

# EFFECT OF DOPANTS ON THE LOCAL ATOMIC STRUCTURE AND SINTERING BEHAVIOR OF BISMUTH SODIUM TITANATE

Dissertation

zur Erlangung der Würde eines Doktors der Naturwissenschaften  
(Dr. rer. nat.) vorgelegt der  
Fakultät für Biologie, Chemie und Geowissenschaften  
der Universität Bayreuth

von

Veronika Schmitt  
aus Regensburg

Würzburg 2013



This doctoral thesis was prepared at the Department of Inorganic Chemistry I at the University of Bayreuth, Faculty for Inorganic Chemistry I, and the Fraunhofer-Institute for Silicate Research in Würzburg from February 2009 to January 2013, and supervised by Professor Dr. Josef Breu.

This is a full reprint of the dissertation submitted to obtain the academic degree of Doctor of Natural Sciences (Dr. rer. nat.) and approved by the Faculty of Biology, Chemistry and Geosciences of the University of Bayreuth.

Actin Dean: Prof. Dr. Rhett Kempe

Date of submission: 01.02.2013

Date of defence (disputation): 06.12.2013

Doctoral Committee:

Prof. Dr. Josef Breu 1<sup>st</sup> reviewer

PD. Dr. Torsten Staab 2<sup>nd</sup> reviewer

Prof. Dr. Jürgen Senker Chairman

Prof. Dr. Hans Keppler





To my  
grandparents



# Abstract

The most commonly used piezoceramic is lead zirconate titanate  $\text{Pb}(\text{Zr}_x\text{Ti}_{1-x})\text{O}_3$  (PZT). It possesses outstanding piezoelectric properties which can be modified for numerous applications by the addition of dopants. However, because of environmental and health concerns regarding lead, lead-free alternatives are demanded by politics.

One of the two most promising lead-free replacement materials is the ferroelectric bismuth sodium titanate  $(\text{Bi}_{0.5}\text{Na}_{0.5})\text{TiO}_3$  (BNT). Like PZT, it crystallizes in the perovskite structure.

Since the dielectric and piezoelectric properties of pure BNT ceramics are insufficient for application, BNT is often modified by the addition of dopants. These influence a great variety of material properties to different degrees, e.g. the sintering behavior, the dielectric and piezoelectric properties and their respective temperature stabilities. Doping of BNT aims to decrease the sintering temperature in order to avoid Bi vaporization, to increase the depolarization temperature and to enhance the piezoelectric coefficient.

The effects of numerous dopants on the resulting performance of BNT were studied extensively in the literature. However, so far little attention has been paid to the way in which dopants interact with the piezomaterial. Nevertheless, it is the understanding of these relationships that would make targeted modifications and improvements of BNT possible.

The primary goal of this study was to investigate and explain the effects of a model dopant—cobalt—on the phase formation, sintering behavior and microstructure of BNT as well as on the resulting dielectric and piezoelectric properties. In this regard, a core issue was to determine the preferred lattice site of Co in BNT.

BNT was synthesized from oxide powders using the classic solid-state route and sintered at temperatures ranging from 1000 °C to 1150 °C. Cobalt was added in concentrations between 0.1 mol % and 2.6 mol % Co prior to the calcination as  $\text{Co}_3\text{O}_4$ .

About one third of the total cobalt amount was incorporated into the BNT lattice on the perovskite B-site, that is, it substituted for Ti. The cobalt in BNT appeared to be in equilibrium with the secondary phase  $\text{Co}_2\text{TiO}_4$ , which invariably formed at cobalt concentrations greater than 0.1 mol % Co. For charge balancing reasons, oxygen vacancies were created in the lattice of cobalt-doped BNT. These markedly enhanced the diffusivity. As a result, the sintering temperature of doped BNT decreased with increasing cobalt concentrations, and high final densities were achieved. However, in highly doped BNT

sample swelling occurred at elevated temperatures of the sintering cycle. This phenomenon was attributed to evaporating oxygen caused by the valence transition of  $\text{Co}^{3+}$  to  $\text{Co}^{2+}$ .

Up to  $950^\circ\text{C}$ , BNT was found to densify via solid state sintering mechanisms. Above this temperature, a small amount of liquid phase was present, which probably formed from decomposing BNT because of a slight Ti-deficiency due to doping. Increased Bi vaporization from the melt above  $1000^\circ\text{C}$  appeared to have stabilized sodium cobalt titanate, an additional secondary phase.

The rotation of the iso-lines in the kinetic field diagram of doped BNT was interpreted such that the activation energy for grain growth was higher than the activation energy for densification. Possible reasons are the solute-drag effect and the pinning of domain walls by secondary phase particles.

Both the depolarization temperature and the piezoelectric coefficient  $d_{33}$  decreased with increasing cobalt concentrations. The dielectric properties deteriorated as well. This was attributed to the high electrical conductivity of the doped samples, which prevented full poling.

# Zusammenfassung

Die am häufigsten eingesetzte Piezokeramik besteht aus Bleizirkontitanat  $\text{Pb}(\text{Zr}_x\text{Ti}_{1-x})\text{O}_3$  (PZT). PZT besitzt herausragende piezoelektrische Eigenschaften, die sich durch die Zugabe von Dotierungen für zahlreiche Anwendungen anpassen lassen. Allerdings bestehen seitens der Politik wegen des hohen Bleigehalts Bedenken hinsichtlich der Umwelt- und Gesundheitsverträglichkeit, weshalb die Erforschung bleifreier Alternativen erforderlich ist.

Eines der am vielversprechendsten Ersatzmaterialien ist das ferroelektrische Bismutnatriumtitanat  $(\text{Bi}_{0.5}\text{Na}_{0.5})\text{TiO}_3$  (BNT). Ebenso wie PZT kristallisiert es in der Perowskitstruktur. Da die dielektrischen und piezoelektrischen Eigenschaften der reinen BNT-Keramik unzureichend für die praktische Anwendung sind, wird es zur Optimierung mit Dotierungen versehen.

Dotierungen haben Einfluss auf eine Vielzahl von Materialparametern, zum Beispiel auf das Sinterverhalten, die dielektrischen und piezoelektrischen Eigenschaften sowie auf deren Temperaturstabilität. BNT wird meist mit dem Ziel dotiert, die benötigte Sintertemperatur zu senken, um das Abdampfen von Bismut zu vermeiden. Außerdem strebt man eine höhere Depolarisierungstemperatur sowie einen gesteigerten piezoelektrischen Koeffizienten  $d_{33}$  an.

In der Literatur wurden die Einflüsse zahlreicher Dotierungen auf die resultierenden Eigenschaften von BNT eingehend untersucht. Wenig Beachtung geschenkt wurde hingegen der Art und Weise, auf welche die Dotierung letztlich mit dem Piezomaterial interagiert. Letztendlich ist es allerdings das Verständnis genau dieser Zusammenhänge, das eine gezielte Modifikation und Verbesserung von BNT-Keramiken ermöglichen könnte.

Ziel der vorliegenden Arbeit war es, die Effekte einer Modelldotierung – Cobalt – auf die Phasenbildung, das Sinterverhalten, das Gefüge und die sich ergebenden dielektrischen sowie piezoelektrischen Eigenschaften zu untersuchen und zu verstehen. In diesem Zusammenhang war auch die Bestimmung der lokalen atomaren Umgebung von Cobalt in BNT, also dessen bevorzugter Gitterplatz, erforderlich.

BNT wurde zunächst über die Mixed-Oxides-Route in einer Festkörperreaktion aus Oxidpulvern hergestellt und anschließend bei Temperaturen zwischen 1000 °C und 1150 °C gesintert. Cobalt wurde in Form von  $\text{Co}_3\text{O}_4$  in Konzentrationen zwischen 0.1 mol % und 2.6 mol % Co vor der Kalzinierung zugegeben.

Etwa ein Drittel der insgesamt zugesetzten Cobalt-Menge wurde in das BNT-Gitter auf dem B-Platz der Perowskit-Struktur, d.h. anstelle von Titan, eingebaut. Dabei besteht

vermutlich ein Gleichgewicht zwischen in BNT eingebautem Cobalt und der Nebenphase  $\text{Co}_2\text{TiO}_4$ , die sich stets bildete, wenn die Gesamtkonzentration 0.1 mol % Co überstieg. Wegen des durch die Ti-Substitution nötigen Ladungsausgleichs wurden im Gitter des dotierten BNTs Sauerstoffleerstellen erzeugt, welche den effektiven Diffusionskoeffizienten stark erhöhten. Dies zeigte sich besonders deutlich dadurch, dass die Sintertemperatur mit steigender Cobalt-Konzentration sank und hohe Enddichten der gesinterten Körper erreicht wurden. Allerdings begannen stark dotierte Sinterkörper bei hohen Sintertemperaturen zu schwellen. Vermutlich war der bei der Reduktion von  $\text{Co}^{3+}$  zu  $\text{Co}^{2+}$  zusätzlich freigesetzte Sauerstoff hierfür verantwortlich.

Bis zu einer Sintertemperatur von 950 °C handelte es sich bei dotiertem BNT um reines Festphasensintern. Oberhalb dieser Temperatur entstand im Gegensatz zum undotierten Material in geringem Umfang eine Schmelzphase, die wahrscheinlich von der Zersetzung des BNT mit leichtem Ti-Unterschuss herrührte. Das vermehrte Abdampfen von Bismut oberhalb von 1000 °C stabilisierte daraufhin wahrscheinlich Natriumcobalttitanat, eine weitere, Bismut-freie Nebenphase.

Das Drehen der Iso-Linien im Kinetic Field-Diagramm von dotiertem BNT wurde dahingehend interpretiert, dass die Aktivierungsenergie für Kornwachstum größer war als die Aktivierungsenergie für Verdichtungsprozesse. Mögliche Ursachen hierfür sind der sogenannte ‘solute-drag’-Mechanismus und ein ‘Pinning’-Effekt der Sekundärphasenpartikel.

Sowohl die Depolarisierungstemperatur als auch der piezoelektrische Koeffizient  $d_{33}$  sanken mit steigender Cobalt-Konzentration. Ebenso verschlechterten sich die dielektrischen Eigenschaften. Dies wurde darauf zurückgeführt, dass aufgrund der hohen elektrischen Leitfähigkeit eine vollständige Polarisierung der Keramiken nicht möglich war.

# Contents

<b>Abstract</b>	<b>vii</b>
<b>Zusammenfassung</b>	<b>ix</b>
<b>1 Introduction and Motivation</b>	<b>1</b>
<b>2 Literature Review</b>	<b>3</b>
2.1 Piezo- and Ferroelectricity . . . . .	3
2.1.1 Piezoelectricity . . . . .	3
2.1.2 Ferroelectricity . . . . .	4
2.2 Ferroelectrics: PZT and Lead-Free Systems . . . . .	6
2.2.1 Lead Zirconate Titanate . . . . .	6
2.2.2 The Lead Issue . . . . .	7
2.2.3 Lead-Free Ferroelectrics . . . . .	8
2.2.4 Bismuth Sodium Titanate . . . . .	8
2.2.5 Doping of Ferroelectrics . . . . .	10
2.2.6 X-ray Absorption Studies of Piezoelectric Materials . . . . .	12
2.3 Sintering . . . . .	13
2.3.1 Sintering Stages . . . . .	13
2.3.2 Sintering of Lead-Free Ferroelectrics . . . . .	13
<b>3 Experimental</b>	<b>15</b>
3.1 Characterization Methods . . . . .	15
3.1.1 Particle Size Measurement . . . . .	15
3.1.2 Powder X-ray Diffraction . . . . .	15
3.1.3 Differential Thermal Analysis . . . . .	16
3.1.4 Density Measurement . . . . .	17
3.1.5 Scanning Electron Microscopy . . . . .	17
3.1.6 Electron Probe Micro Analysis . . . . .	18
3.1.7 X-ray Absorption Fine Structure . . . . .	19
3.1.8 Transmission Electron Microscopy . . . . .	23
3.1.9 Thermo-Optical Dilatometry . . . . .	24
3.1.10 Dielectric and Piezoelectric Properties . . . . .	26

3.2	Synthesis of BNT . . . . .	28
3.2.1	Synthesis Route . . . . .	28
3.2.2	Choice of the Dopant Oxide . . . . .	28
3.2.3	Raw Material Characterization . . . . .	29
3.2.4	Calcination Parameters . . . . .	30
<b>4</b>	<b>Data Evaluation</b>	<b>33</b>
4.1	Simulation of XANES Spectra . . . . .	33
4.2	Thermo-Optical Data Evaluation . . . . .	33
4.2.1	Thermal Expansion Correction . . . . .	33
4.2.2	Kinetic Field Analysis . . . . .	34
4.3	Determination of Depolarization Temperature . . . . .	34
<b>5</b>	<b>Local Atomic Environment of Co</b>	<b>37</b>
5.1	Phase Formation in Cobalt-Doped BNT . . . . .	37
5.2	Incorporation of Co in BNT . . . . .	41
5.3	Lattice Site Preference . . . . .	45
5.4	Discussion . . . . .	47
5.4.1	Secondary Phases . . . . .	47
5.4.2	Local Atomic Environment . . . . .	48
5.4.3	Valence State . . . . .	49
5.4.4	Quantitative Considerations . . . . .	50
<b>6</b>	<b>Sintering of Cobalt-Doped BNT</b>	<b>53</b>
6.1	Initial Sintering Stage . . . . .	53
6.2	Intermediate Sintering Stage . . . . .	53
6.3	Final Sintering Stage . . . . .	56
6.4	Kinetic Field . . . . .	58
6.5	Discussion . . . . .	60
6.5.1	Densification Behavior . . . . .	60
6.5.2	Swelling of Doped BNT . . . . .	61
6.5.3	Liquid Phase Sintering . . . . .	62
6.5.4	Phase Development During Sintering . . . . .	63
6.5.5	Sintering Kinetics . . . . .	64
6.5.6	Sintering Mechanisms . . . . .	65
<b>7</b>	<b>Piezoelectric and Dielectric Characterization</b>	<b>67</b>
7.1	Dielectric Permittivity and Loss Tangent . . . . .	67
7.2	Electrical Conductivity . . . . .	69
7.3	Depolarization Temperature . . . . .	70
7.4	Piezoelectric Coefficient . . . . .	70
7.5	Discussion . . . . .	71



<b>8 Conclusion</b>	<b>73</b>
<b>References</b>	<b>75</b>
<b>A Appendix</b>	<b>85</b>
A.1 Table of Raw Materials . . . . .	86
A.2 Crystallographic Data for XANES Calculations . . . . .	87
A.3 STEM-EDX Line Scans . . . . .	88
A.4 Dielectric Characterization of BNT . . . . .	91
<b>Curriculum Vitae</b>	<b>93</b>
<b>Acknowledgments</b>	<b>95</b>
<b>Declaration of Authorship</b>	<b>97</b>



# List of Figures

2.1	Perovskite structure using the example of $\text{PbTiO}_3$ . . . . .	5
2.2	Ferroelectric domains in a ceramic material . . . . .	6
2.3	Schematic P-E hysteresis loop of a ferroelectric . . . . .	6
2.4	Phase diagram of lead zirconate titanate . . . . .	7
2.5	Perovskite structure of BNT . . . . .	9
2.6	Compositions of cobalt-doped $(1-x)\text{BNT}-x\text{BT}$ in the literature . . . . .	12
2.7	Sintering stages in a BNT shrinkage curve . . . . .	14
3.1	Bragg's law . . . . .	16
3.2	Schematic of cross-section polishing . . . . .	18
3.3	Relaxation mechanisms in an atom with a core hole in the K-shell . . . . .	19
3.4	Absorption coefficient of metallic Cobalt at the K-edge . . . . .	20
3.5	Scattering of photoelectron-waves at the next neighbor atoms . . . . .	21
3.6	XANES: Schematic representation of the experimental setup . . . . .	22
3.7	Schematics of the TOM furnace . . . . .	25
3.8	Schematics of the Berlincourt-type setup used to measure $d_{33}$ . . . . .	27
3.9	Synthesis steps for BNT . . . . .	29
3.10	SEM images of the starting oxides . . . . .	31
3.11	Powder XRD of calcined BNT with 2.6 mol % Co . . . . .	31
4.1	Construction of the kinetic field diagram . . . . .	35
5.1	Powder X-ray diffractograms of sintered BNT . . . . .	38
5.2	SEM backscattering images of cobalt-doped and sintered BNT samples . . . . .	40
5.3	Quenching effect on BNT doped with 2.6 mol % Co . . . . .	41
5.4	Electron probe micro analysis measurement procedure . . . . .	42
5.5	Quantitative electron probe micro analysis of cobalt-doped BNT . . . . .	42
5.6	Effect of sintering temperature on the cobalt concentration . . . . .	43
5.7	HR-TEM image of BNT doped with 2.6 mol % Co . . . . .	44
5.8	STEM image of BNT doped with 2.6 mol % Co . . . . .	44
5.9	STEM image of BNT powder doped with 2.6 mol % Co after calcination . . . . .	44
5.10	Influence of temperature and dopant level on XANES spectra of Co in BNT . . . . .	45
5.11	Experimental XANES spectra compared to ab-initio calculations . . . . .	46

5.12	Superposition of calculated XANES spectra . . . . .	47
5.13	Cobalt concentration in BNT lattice versus total cobalt concentration . . .	50
6.1	Sinter shrinkage of cobalt-doped BNT . . . . .	54
6.2	$T_{\text{Onset}}$ and $T_{50}$ of cobalt-doped BNT . . . . .	54
6.3	Sintering uniaxial with load . . . . .	55
6.4	Setup for melting experiments . . . . .	56
6.5	Final densities of pure and doped BNT ceramics . . . . .	57
6.6	Sample expansion during sintering . . . . .	57
6.7	Shrinkage curves at different constant heating rates . . . . .	58
6.8	Kinetic field of pure and cobalt-doped BNT . . . . .	59
6.9	Apparent activation energies . . . . .	60
6.10	Proposed reaction sequence in cobalt-doped BNT . . . . .	64
7.1	$\varepsilon_r$ and $\tan \delta$ of BNT as a function of temperature . . . . .	68
7.2	Calculated AC conductivity of poled BNT samples . . . . .	69
7.3	Piezoelectric coefficient $d_{33}$ of doped BNT . . . . .	71
A.1	STEM-EDX line scan: grain boundary 1 . . . . .	88
A.2	STEM-EDX line scan: grain boundary 2 . . . . .	89
A.3	STEM-EDX line scan: grain boundary 3 . . . . .	90
A.4	$\varepsilon_r$ and $\tan \delta$ of doped BNT as a function of temperature . . . . .	91

# List of Tables

2.1	Typical properties of ferroelectric ceramics . . . . .	10
3.1	Parameters for XAFS data collection . . . . .	23
3.2	Starting powders for BNT synthesis . . . . .	30
5.1	Secondary phases in sintered BNT ceramics doped with cobalt . . . . .	39
5.2	Ionic radii and tolerance factors for selected B-site cations . . . . .	49
7.1	AC conductivities of BNT and BNT doped with 2.6 mol % Co . . . . .	70
7.2	Depolarization temperatures for pure and doped BNT . . . . .	70
A.1	Detailed list of starting powders for BNT synthesis . . . . .	86
A.2	Crystallographic data used for XANES calculations . . . . .	87



# 1 Introduction and Motivation

Up to today, the most commonly used piezoceramic is lead zirconate titanate (PZT)  $\text{Pb}(\text{Zr}_x\text{Ti}_{1-x})\text{O}_3$  [Jaf71]. It shows outstanding piezoelectric properties, which can be tailored by the addition of dopants to fulfill the requirements of numerous applications. These include sensors, actuators or ultrasonic transducers for industrial, commercial, scientific or medical devices. However, PZT consists of more than 60 wt % lead, which complicates recycling and waste disposal. Moreover, during the fabrication process, hazardous lead oxide is set free.

In the wake of the augmenting environmental awareness, the legislations regarding the use of lead have recently been hardened in countries all over the world [Röd09]. In 2006, for instance, the European Union adopted two directives, WEEE<sup>1</sup> and RoHS<sup>2</sup>, which restrict the use of hazardous substances, amongst others lead, in electrical and electronic equipment used in households and industry. Exceptions are made only for applications in which the replacement by lead-free substances is not yet feasible.

It was due to such legislations that the search for lead-free alternatives to PZT was revived about ten years ago. So far, the outstanding and versatile properties of PZT are unmatched. It appears possible, though, to adapt replacement materials so that they can be used for specific, albeit rather narrow fields of application.

Currently, the most promising lead-free materials are based on two perovskite systems: Potassium sodium niobate  $(\text{K}_{0.5}\text{Na}_{0.5})\text{NbO}_3$  (KNN), and bismuth sodium titanate  $(\text{Bi}_{0.5}\text{Na}_{0.5})\text{TiO}_3$  (BNT). The piezoelectric properties of pure KNN and BNT ceramics, however, are insufficient for application. The main issues root in the poor densification behavior, which necessitates high sintering temperatures of more than 1100 °C [Du06, Hir09]. The subsequent evaporation of alkali oxides or bismuth oxide has a deteriorating effect on the piezoelectric performance.

The attempts to overcome these obstacles focus on the one hand on binary or ternary complex solid-solution systems of BNT or KNN with other perovskite structures. On the other hand, dopants in the range of a few mol % can be used to enhance the performance of pure BNT and KNN or their respective solid-solution systems.

Dopants influence a great variety of material properties to different degrees. For exam-

---

<sup>1</sup>Waste Electrical and Electronic Equipment [Eur03b]

<sup>2</sup>Restriction of the Use of Certain Hazardous Substances in Electrical and Electronic Equipment [Eur03a]

ple, they can drastically alter the sintering behavior [Hua09] and the resulting microstructure of a ceramic. They also affect the dielectric and piezoelectric properties as well as their respective temperature stability.

The role of dopants during the sintering process and their effects on a ceramic's piezoelectric performance has so far received little attention from a microscopic point of view. Nonetheless, understanding the way dopants interact with the piezomaterial is crucial to explain their effects and to open up the possibility to improve these properties selectively.

The goal of this study is to investigate and understand the effects of a model dopant on the local atomic structure of BNT (that is, the preferred lattice site in which the dopant is incorporated), on its sintering behavior, microstructure, and the resulting dielectric and piezoelectric properties. Cobalt, which acts as a so called 'hard' dopant in PZT, was chosen for this purpose. Studies in the literature reported conflicting findings on how the changes in the microstructure and piezoelectric properties of cobalt-doped BNT-BaTiO<sub>3</sub> (BNT-BT) are related [Chu02, Li04, Xu05, Zha07, Xu08b]. To avoid additional effects from the solid-solution with barium titanate, the current work is constrained to the study of pure BNT doped with cobalt.

A broad set of analytical techniques is employed to cover the diverse aspects of this topic. X-ray diffraction and scanning electron microscopy are used for phase analysis. The incorporation of cobalt into BNT is studied by means of electron probe micro analysis and transmission electron microscopy. To determine the local atomic environment of the dopant, X-ray absorption spectra are recorded and compared to theoretical calculations. The sintering behavior is studied by thermo-optical dilatometry and the sintering kinetics are analyzed by means of the kinetic field method. Finally, the dielectric and piezoelectric characteristics of the doped ceramic are studied.

The following work is outlined as follows: First, the literature overview covers the basics of piezoelectricity, ferroelectric ceramics and sintering. The experimental section provides details on the measuring techniques and the synthesis route of BNT. In Chapter 5, the phase formation and the local atomic structure of Co is covered. Chapter 6 deals with the sintering behavior, and Chapter 7 presents the dielectric and piezoelectric characterization. Finally, Chapter 8 summarizes and concludes the findings of this study.



## 2 Literature Review

### 2.1 Piezo- and Ferroelectricity

Piezoelectricity is the ability of a material to translate mechanical stress into electrical charge and vice versa. It was first discovered by Jacques and Pierre Curie in 1880 in Rochelle salt. The first piezoelectric ceramic, consisting of ferroelectric  $\text{BaTiO}_3$ , was synthesized in the 1940s [Thu77]. Today's most popular material for ferroelectric applications is lead zirconate titanate  $\text{Pb}(\text{Zr}_x\text{Ti}_{1-x})\text{O}_3$  (PZT), which was discovered about ten years later [Hae99]. Since then, piezoelectric ceramics and ferroelectric materials in general have found a vast range of industrial and scientific applications. Among them are piezoelectric fuel injection systems, motors, inkjet printer heads, micro-positioning systems, piezoelectric transducers for medical purposes, electroacoustic transformers and sensors.

#### 2.1.1 Piezoelectricity

According to the definition by Cady [Cad46], piezoelectricity is the “[...] electric polarization produced by mechanical strain in crystals belonging to certain classes, the polarization being proportional to the strain and changing sign with it.” This definition basically contains the description of the direct piezoelectric effect: When mechanical stress is applied to a piezoelectric material, a charge is generated. The converse effect is called indirect piezoelectric effect. When the material is subjected to an electric field, a strain is induced. The following equations state the relationship between the mechanical and electrical variables for both effects:

$$D_i = d_{ij}T_j \quad (2.1)$$

$$S_i = d_{ij}E_j \quad (2.2)$$

Here,  $T$  is the mechanical stress,  $S$  is the field-induced strain,  $E$  is the electric field, and  $D$  is the dielectric displacement.  $D$  is related to the polarization  $P$  by  $D = \varepsilon_0 E + P$ , with  $\varepsilon_0 = 8.854 \times 10^{-12} \text{ F m}^{-1}$  (permittivity of vacuum). The proportionality factor  $d_{ij}$  is called piezoelectric constant. The indices  $i$  and  $j$  refer to the direction in which  $T$ ,  $S$ ,  $E$  and  $D$  are applied or generated. 3 indicates the polarization direction, 1 and 2 are directions perpendicular to 3 and each other, and 4, 5 and 6 indicate shear. A detailed explanation and the full set of equations of state can be found e.g. in the textbooks by Jaffe [Jaf71] and Xu [Xu91].

The most often reported piezoelectric constant,  $d_{33}$ , relates the mechanical stress and electrical displacement (or mechanical strain and electric field strength) in the direction of polarization. It is an important figure of merit for the piezoelectric effect and especially important for sensors. Another frequently reported quantity is the piezoelectric coupling factor  $k$ , which describes how efficiently one form of energy is converted into another. It is defined as

$$k^2 = \frac{\text{electric energy converted to mechanical energy}}{\text{input electric energy}} \quad (2.3)$$

or

$$k^2 = \frac{\text{mechanical energy converted to electric energy}}{\text{input mechanical energy}} \quad (2.4)$$

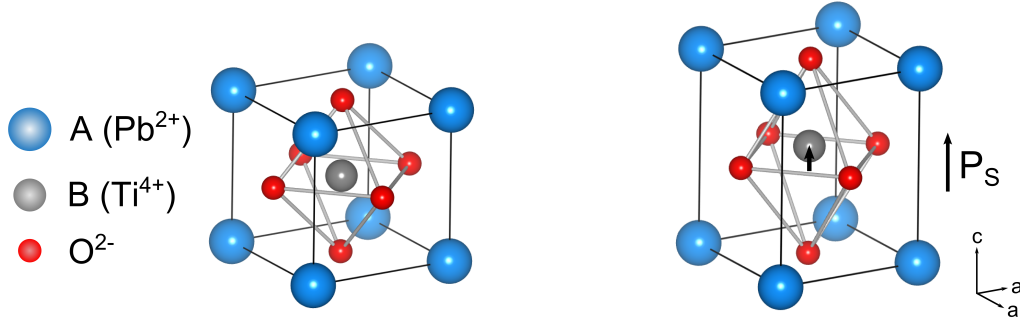
Thus the  $k$ -factor is a measure of the overall strength of the electromechanical effect. It is always less than unity, because the conversion of energy is always incomplete [Jaf71].

### 2.1.2 Ferroelectricity

In order to obtain a piezoelectric ceramic, the used material must additionally be ferroelectric. Ferroelectric materials are a subgroup of piezoelectric materials.

All crystal systems lacking a center of symmetry  $\bar{1}$  exhibit piezoelectricity (except for the point group 432 due to other geometrical reasons) [Jaf71]. Ten of those 20 point groups allow for the existence of permanent electric dipoles. The magnitude of their polarity changes with temperature. Hence, these materials are termed *pyroelectric*. If the direction of the permanent dipole can be switched by the application of an electric field, the material is called ferroelectric.

Most ferroelectric ceramics consist of materials that crystallize in the perovskite structure [Dam01], such as PZT or BaTiO<sub>3</sub>. The general formula is ABO<sub>3</sub>. Figure 2.1a shows the structure of a perovskite in the cubic modification. The big A-ions are located on the corners of the unit cell ('A-site'). The center is occupied by the smaller B-cation ('B-site'), which is surrounded by 6 oxygens forming octahedra that are corner-linked with each other. Ferroelectric perovskites usually are of the type A<sup>2+</sup>B<sup>4+</sup>O<sub>3</sub> or A<sup>1+</sup>B<sup>5+</sup>O<sub>3</sub> [Xu91]. In the cubic modification, this structure is nonferroelectric or paraelectric. When it is cooled below its Curie temperature  $T_C$ , it undergoes a phase transition to an antiferroelectric or ferroelectric modification (tetragonal, rhombohedral, orthorhombic or monoclinic) as shown in Figure 2.1b. The structure now possesses permanent electric dipoles that occur because the cation sublattice is shifted with respect to the oxygen sublattice. As a result, a net dipole moment is generated. The value of the dipole moment per unit volume is called spontaneous polarization  $P_S$ . Even in single crystals, the dipole orientation is not completely uniform [Dam98]. Instead, regions with dipoles oriented in the same direction, called domains, exist. The boundaries to regions with a different dipole orientation are called domain walls. In polycrystalline ceramics, the crystals as well as the domains are randomly oriented, and thus the moments of spontaneous polarization cancel each other out (see Figure 2.2a). To obtain a piezoelectric ceramic, the dipole moments must be aligned in a single direction. This can be achieved by subjecting the material to a strong



(a) Cubic perovskite  $\text{ABO}_3$ : the oxygen octahedron is occupied by the B cation, the corners of the unit cell are occupied by 12-fold coordinated A-ions.

(b) Perovskite with tetragonal distortion: the B-site ion is displaced from the center and gives rise to a dipole moment  $\mathbf{P}_s$ .

**Figure 2.1:** Perovskite structure using the example of  $\text{PbTiO}_3$ <sup>1</sup>; the cubic modification is nonferroelectric, the tetragonal modification has a dipole moment and shows ferroelectricity.

electric field (see Figure 2.2b). The polarization in the ceramic changes according to the hysteresis loop shown in Figure 2.3. When the electric field  $E$  is applied for the first time (1), the dipoles begin to change their orientation until a maximum polarization is reached (2). The dipoles are now oriented along the field in the best possible way. Upon reduction of the field to zero, most of the dipoles retain their orientation. The resulting polarization is called the remanent polarization  $P_r$ . When the direction of the external electric field is switched and the field increases until maximum polarization is reached (3), the dipoles slowly change their orientation. The field strength at which the polarization becomes zero is called the coercive field strength  $E_c$ .

In addition to the parameters introduced above, many others can be measured to characterize the behavior of a ferroelectric ceramic. Important quantities are the relative dielectric permittivity  $\epsilon_r$  (more precisely,  $\epsilon_{33}^T/\epsilon_0$ , where  $T$  indicates constant stress) and the dielectric loss or loss tangent  $\tan \delta$ .  $\tan \delta$  is a measure of the proportion of the charge transferred in conduction to that stored in polarization. High losses degrade the performance of the dielectric, especially in capacitor applications.

High dielectric constants are desirable for example for actuators, together with a high mechanical quality factor  $Q_m$  [Pan09]. Since actuators are designed for maximum strain at minimum coaxial electric field [Röd09], the so called large signal  $d_{33}$  may also be of interest. In contrast to the *small signal*  $d_{33}$  defined in 2.1.1, the *large signal*  $d_{33}$  represents the maximum obtainable strain at maximum electric field in the poling direction  $S_{3,\max}/E_{3,\max}$ . Sometimes,  $s_{ij}^E$ , the material compliance (inverse of modulus of elasticity) at constant electric field is also reported.

<sup>1</sup>Crystal structures were drawn using VESTA 3 [Mom11]

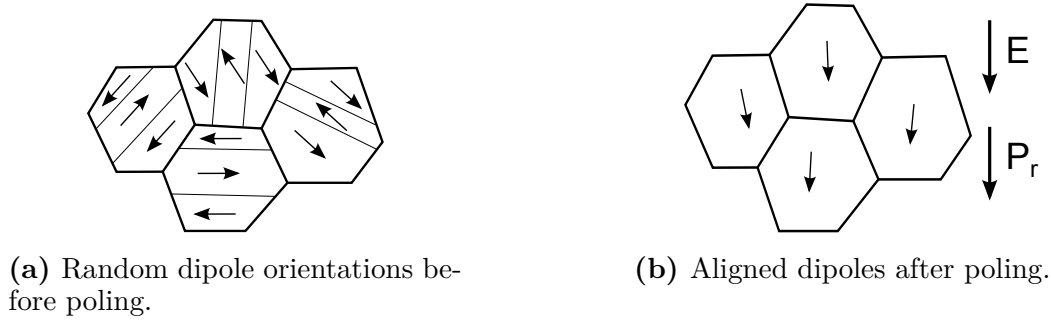


**Figure 2.2:** Ferroelectric domains in a ceramic material. a) Before poling: Each grain shows domains with dipoles (arrows) oriented  $180^\circ$  with respect to each other; b) Poled ceramic: the dipoles are aligned in the direction of the electric field, a net remanent polarization results; the ceramic is slightly elongated in the direction of the polarization.

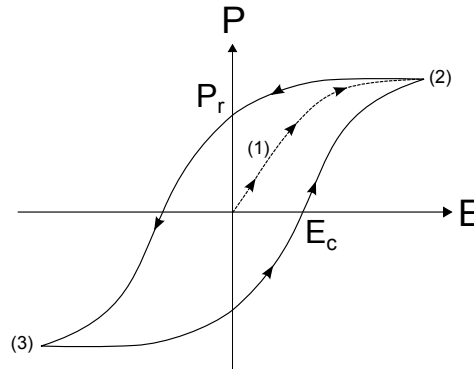


**Figure 2.3:** Schematic P-E hysteresis loop of a ferroelectric. (1) represents the initial polarization curve,  $E_C$  is the coercive field strength, and  $P_r$  denotes the remanent polarization.

## 2.2 Ferroelectrics: PZT and Lead-Free Systems

### 2.2.1 Lead Zirconate Titanate

The most commonly used material for piezoelectric ceramics is the solid solution lead zirconate titanate  $\text{Pb}(\text{Zr}_x\text{Ti}_{1-x})\text{O}_3$  (PZT). Its outstanding ferroelectric properties were discovered in 1954 by Jaffe [Jaf54]. PZT belongs to the family of perovskites. The octahedral B-site is shared by the ions  $\text{Ti}^{4+}$  and  $\text{Zr}^{4+}$ , while  $\text{Pb}^{2+}$  occupies the 12-fold coordinated A-site (cf. Figure 2.1). The best piezoelectric properties are obtained at the boundary between the rhombohedral  $\text{PbZrO}_3$  and the tetragonal  $\text{PbTiO}_3$ , where  $x(\text{Zr})=0.53$ . This boundary is called morphotropic phase boundary (MPB) and it is almost temperature independent. It is shown in Figure 2.4. The superior properties at this composition mainly stem from the fact that the electrical dipoles can be aligned along as many as 14 different orientations, which leads to a higher degree of overall dipole alignment than in other

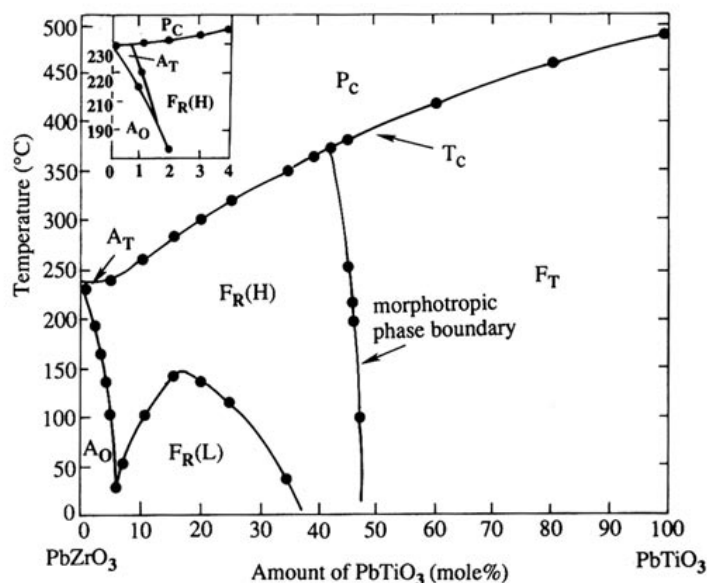


**Figure 2.4:** Phase diagram of lead zirconate titanate (PZT) after Jaffe et al. [Jaf71].

compositions [Swa90]. The remanent polarization of PZT at the MPB-composition is  $35 \mu\text{C cm}^{-2}$ . Poling is easily achieved at a low coercive field of  $1 \text{ kV mm}^{-1}$  to  $2 \text{ kV mm}^{-1}$ . The Curie temperature  $T_C$  is above  $350^\circ\text{C}$  and thus allows for comparably high operating temperatures. The PZT properties can readily be modified by the addition of dopants (see Chapter 2.2.5) to make the material suitable for a great variety of applications.

## 2.2.2 The Lead Issue

The combination of all the above mentioned properties explain why PZT has become so popular. However, there are some severe drawbacks which make it necessary to find alternate ferroelectric systems for piezoelectric applications.

PZT contains more than 60 wt % Pb. Lead and its derivatives are toxic to humans and other organisms, especially if inhaled. During the fabrication of PZT, lead oxide evaporates and is set free. Lead-contaminated dust is generated when PZT parts are machined. Another issue arises concerning the waste disposal and recycling of electrical and electronic devices.

The growing environmental awareness has lead to several new directives being established. For example, as of 1 July 2006, the European Union adopted the ‘directive on the restriction of the use of certain hazardous substances in electrical and electronic equipment’, RoHS [Eur03a]. This directive restricts the use of lead and other hazardous elements in the manufacture of most electronic and electrical equipment. Exemptions are made for medical devices, monitoring and control instruments only, but the allowed lead content is limited. For cases in which it is technically or scientifically impracticable to use lead-free replacements, such as for electronic ceramics, the use of lead is not yet prohibited, but will

probably be forbidden as soon as alternative materials are available. Similar regulations are being promoted in countries all over the world [Röd09].

A lot of scientific activity has since been triggered to explore alternative non-hazardous materials for the use in piezoelectric devices. There are many excellent reviews on the current status of the development of lead-free materials [Röd09, Dam10, Aks10b, Pan09, Shr07]. Up to this day, the piezoelectric properties of all suggested material systems are still inferior to those of PZT. Few patents for the actual application of lead-free piezoelectrics have so far been filed [Chi06, Tan01]. It seems likely that, for specific applications, specially tailored replacements can be found. However, there appears to be no ‘all-round’ material that is as versatile as lead zirconate titanate [Röd09], since its superior piezoelectric properties are based on the chemical nature of the lead ion [Coh92].

### 2.2.3 Lead-Free Ferroelectrics

Apart from a few material families for specialized applications, such as potassium tungsten bronze structures for sensors [Jam68] or bismuth layered structure ferroelectrics for high temperature applications [Ike74], perovskite structures still appear to be the most promising class of ferroelectrics. Two systems, both with perovskite structure, have received major attention in research: potassium sodium niobate ( $\text{K}_{0.5}\text{Na}_{0.5}\text{NbO}_3$  (KNN) and bismuth sodium titanate ( $\text{Bi}_{0.5}\text{Na}_{0.5}\text{TiO}_3$  (BNT). The first system, KNN, is described in brief below; for further details, the reviews on lead-free materials offer a good insight. BNT, being the topic of this thesis, is presented in greater detail in the following section.

KNN is a solid solution of ferroelectric  $\text{KNbO}_3$  and antiferroelectric  $\text{NaNbO}_3$  (both orthorhombic). The best piezoelectric properties are obtained at the morphotropic phase boundary [Mae04], similar to PZT. KNN can yield a high longitudinal piezoelectric coefficient ( $148 \text{ pC N}^{-1}$  [Li06]), a good electromechanical coupling coefficient and has a high  $T_C$  of up to  $420^\circ\text{C}$  [Pan09]. However, processing of the raw materials as well as sintering is difficult [Hol05].

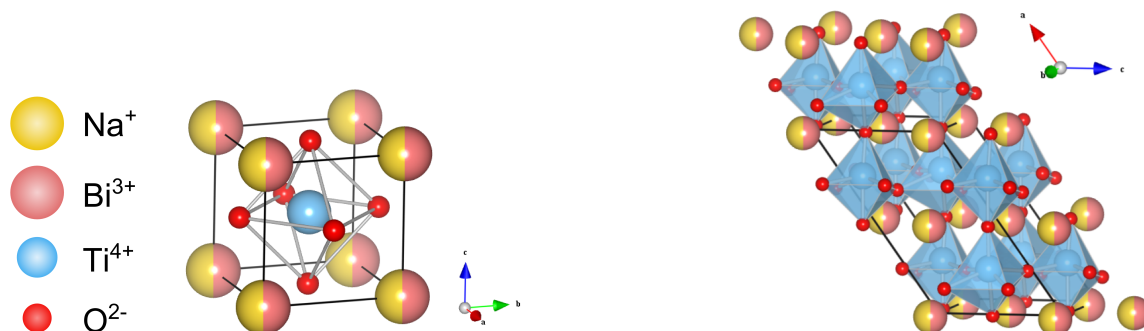
### 2.2.4 Bismuth Sodium Titanate

BNT was discovered in the 1960s by Smolenskii et al. [Smo61], but, due to its inferior piezoelectric properties compared to PZT, did not receive much attention until lately. The following sections give an overview over the current state of knowledge of its crystal structure, phase transitions and piezoelectric properties.

#### Crystal Structure

BNT crystallizes in the perovskite structure (Figure 2.5a), similar to PZT and KNN (see also Chapter 2.1.2). The octahedral site is occupied by the  $\text{Ti}^{4+}$  ion. The A-site is shared by  $\text{Na}^{1+}$  and  $\text{Bi}^{3+}$  in the ratio 1:1. The distribution of the two A-site cations is still subject to investigation [Grö11]. One consequence of the shared A-site is the relaxor behavior of BNT [Röd09]. The term *relaxor* refers to a class of disorder crystals with peculiar

structural features and properties [Bok06]. It is caused by a disorder of ions sharing the same crystallographic site. Relaxor behavior manifests e.g. in broad humps instead of narrow peaks of the dielectric permittivity  $\epsilon$  as a function of temperature at the material's Curie temperature [Dan11].



(a) Cubic BNT: the center of the oxygen octahedron is occupied by the  $\text{Ti}^{4+}$  cation, the corners of the unit cell are occupied by  $\text{Na}^{1+}$  and  $\text{Bi}^{3+}$  in the ratio 1:1.

(b) Room temperature structure of BNT with monoclinic distortion.

**Figure 2.5:** Perovskite structure of BNT<sup>2</sup>: a) above the Curie temperature, b) at room temperature.

The phase transitions of BNT are still being discussed controversially. Basically, the material undergoes two phase transitions upon cooling : from cubic to tetragonal at 540 °C, and from tetragonal to its room temperature modification between 325 °C and 200 °C [Suc95, Jon02]. The structure in the region of the second phase transition is being discussed as being either antiferroelectric [Sak74] or as a coexistence region of rhombohedral and tetragonal phases with polar nano regions [Suc88]. At room temperature, a monoclinic structure (space group  $Cc$ ) has also been proposed [Aks11]. It is, however, usually sufficient to use the rhombohedral model (space group  $R3c$ ) determined by Jones and Thomas [Jon02] for the average room temperature structure [Kee12], which is shown in Figure 2.5b.

## Piezoelectric Properties

The piezoelectric properties of BNT are summarized in Table 2.1. BNT has a Curie temperature of 325 °C. Due to the transition region between rhombohedral and tetragonal phase, however, BNT loses its polarization at 187 °C [Hir09]. This temperature is hence called depolarization temperature. BNT possesses a large remanent polarization of 38  $\mu\text{C cm}^{-2}$ , comparable to that of PZT (35  $\mu\text{C cm}^{-2}$ ). Full poling may be difficult to achieve, mainly because of the high coercive field of 7.3 kV mm<sup>-1</sup>.

<sup>2</sup>Crystal structures were drawn using VESTA 3 [Mom11]

**Table 2.1:** Typical properties of ferroelectric ceramics. Usually, a high Curie temperature  $T_c$ , a high coupling coefficient  $d_{33}$ , a high mechanical quality  $Q_m$  and a low dissipation factor  $\tan \delta$  are desired. The relative dielectric permittivity  $\varepsilon_r$  should either be high or low, depending on the specific application.

Material	$T_c$ [°C]	$\varepsilon_r$	$\tan \delta$	$d_{33}$ [pC N <sup>-1</sup> ]	$Q_m$	Reference
Pb(Zr <sub>0.48</sub> Ti <sub>0.52</sub> )O <sub>3</sub>	386	399	0.004	223	500	[Jaf71]
DoD I PZT4 <sup>(a)</sup>	328	1300	0.004	290	>500	[Shr07]
DoDII PZT5A <sup>(b)</sup>	365	1700	0.02	375	75	[Shr07]
KNN	395	559	0.026	148	215 <sup>(c)</sup>	[Li06]
Bi <sub>0.5</sub> Na <sub>0.5</sub> TiO <sub>3</sub>	325	343	0.045	73	368	[Hir09]
BNT-6BT	105	826	0.025	155	-	[Xu08a]
BNT-7BT + 2.3 % Co	>120	600	0.008	137	297	[Xu08b]

<sup>(a)</sup> ‘hard’ doped PZT    <sup>(b)</sup> ‘soft’ doped PZT    <sup>(c)</sup> [Lin08]

From Table 2.1 it is evident that the properties of pure BNT are inferior to PZT and currently not sufficient for practical applications. Furthermore, the pure material is difficult to synthesize. Dense BNT ceramics require a sintering temperature of at least 1100 °C [Hir09]. At this temperature, significant bismuth evaporation was observed [Nag06]. The resulting bismuth and oxygen vacancies are believed to be the reason for the relatively high electrical conductivity of BNT ceramics [Hir09]. This adds to the poling difficulties and thus has a negative effect on the final piezoelectric properties.

## 2.2.5 Doping of Ferroelectrics

### Doping of PZT

Pure PZT itself is also unsuitable for most applications. To tailor its properties to the desired application, it is usually doped with one or more additives. *Doping* implies that ions of a different atomic species are added, either of similar (isovalent doping) or different (aliovalent doping) valence than those present in the doped material. In the case of ferroelectric ceramics, the dopant amount is typically in the range of 0.1 mol % to 2.5 mol %.

Depending on the nature of the dopant species, the properties of PZT can be altered following basically two opposed trends:

1. *‘Soft’ doping.* Ions of higher valence are introduced on either the A- or the B-site, causing Pb<sup>2+</sup> vacancies. As a result, domain wall motions are facilitated [Xu91]. In general, the elastic compliance coefficients  $s_{ij}$ , the dielectric constant  $\varepsilon$ , the planar coupling coefficient  $k_p$  as well as the bulk resistivity  $\sigma$  are increased by soft doping, while the coercive field  $E_c$  and the mechanical quality  $Q_m$  are decreased. Soft dopants



for PZT include  $\text{La}^{3+}$ ,  $\text{Bi}^{3+}$ ,  $\text{Nb}^{5+}$ ,  $\text{W}^{6+}$ .

2. *‘Hard’ doping.* The dopant ions have a lower valence than those they replace and thus are considered acceptors. They can either occupy the A- or B-site of PZT. For charge balancing reasons, oxygen vacancies are generated in the p-type electrical conductor material. This results in space charges which inhibit the domain wall motion. Hard doped PZT has a lower dielectric constant  $\varepsilon$ , lower dielectric loss  $\tan\delta$ , lower the planar coupling coefficient  $k_p$  and lower bulk resistivity  $\sigma$  than pure PZT, whereas the coercive field  $E_c$  and mechanical quality factor  $Q_m$  are enhanced.  $\text{Na}^+$ ,  $\text{Fe}^{2+}$ ,  $\text{Co}^{3+}$ ,  $\text{Mn}^{2+}$ , and  $\text{Ni}^{2+}$  are examples for hard PZT dopants.

## Doping of BNT

Doping of BNT currently aims to decrease the vaporization of bismuth by reducing the sintering temperature and to make full poling possible, but it is also intended to increase the depolarization temperature. A great variety of dopants was screened in the literature, for example Fe [Wat07, Aks12], Mn [Dav11, Xu06], Li [Lu06], La [Her97], Sr [GP04], and Ta [Koe07]. A comprehensive compilation can be found in the excellent review paper by Roedel et al. [Röd09].

In general, large dopant ions that are incorporated on the A-site of BNT lead to a softening of the piezoelectric properties, while B-site dopants seem to be associated with a hardening effect. When comparing the effect of a dopant on PZT and BNT, it is important to remember that PZT has its shared ion position on the B-site, whereas in BNT the A-site is affected. For this reason, doping the A-site of BNT is considered more effective than B-site doping [Xia08], which is favored in PZT.

Another effective way to improve the sinterability and the piezoelectric properties of BNT was introduced by Takenaka et al. [Tak91]. He first reported the superior properties of the solid solution of BNT with  $\text{BaTiO}_3$  (BT), which can be attributed to the existence of a morphotropic phase boundary. However, the MPB is curved, which means that the associated properties are very temperature sensitive. Furthermore, while  $d_{33}$  was strongly enhanced, the depolarization temperature was lowered to about 100 °C [Che08a]. Other binary and ternary solid solution systems with an MPB have since been investigated, for example BNT-BKT ( $\text{BNT-Bi}_{0.5}\text{K}_{0.5}\text{TiO}_3$ ) [Sas99], BNT-BT-KNN [Zha08a, Zha08b], or BNT-BKT-BT [Nag03].

## Doping with Co

This work is the first study on pure BNT doped with Co. In the literature, there are some related studies which deal with the effect of cobalt-doping on  $(1-x)\text{BNT}-x\text{BT}$  [Chu02, Li04, Xu05, Zha07, Xu08b] at the MPB. Here,  $x$  refers to the amount of  $\text{BaTiO}_3$  added, which is usually between 6 mol % and 8 mol % (the exact composition of the MPB is controversial). Figure 2.6 compares the compositions studied in this work to those of the previous ones.

The most systematic of the mentioned studies was carried out by Xu et al. in 2008 [Xu08b]. His group added varying amounts of Co to BNT-BT synthesized via a sol-

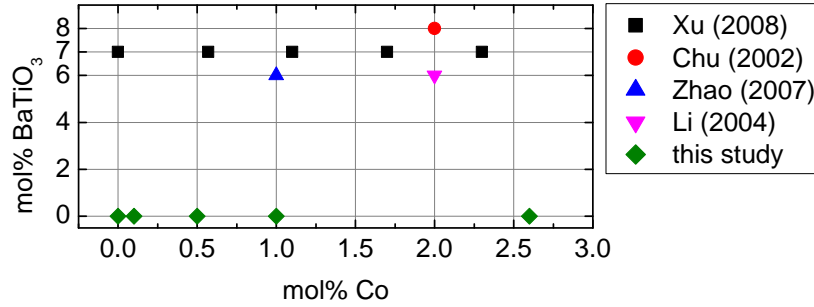


**Figure 2.6:** Compositions of cobalt-doped (1-x)BNT-xBT in the literature, compared to this work.

gel-method. They found that the resulting piezoelectric properties generally followed a ‘hard’ doping effect, that is,  $T_C$  was increased, whereas  $d_{33}$  declined with increasing dopant amount. However, the effect on  $d_{33}$  is not entirely clear, since the group of Li et al. [Li04] reported the opposite effect. They explained this by the strongly enhanced grain growth, that supported the development of large ferroelectric domains. These make higher  $d_{33}$  coefficients possible. However, Xu found no such effect in his study.

According to Xu,  $\text{Co}^{2+}$  can substitute for  $\text{Ti}^{4+}$  because of radius matching. For charge balancing, oxygen vacancies would have to form, which harden the material by a clamping effect. In all studies, cobalt was claimed to replace  $\text{Ti}^{4+}$ , either in its di- or trivalent state, the only basis for the assumption being the similar size of the ionic radii. This problem was addressed in the current study by the means of X-ray absorption experiments.

## 2.2.6 X-ray Absorption Studies of Piezoelectric Materials

X-ray absorption spectra (XAS) give insight into the local atomic environment of one selected atomic species at a time. It can be used to determine the number, distance, coordination geometry and nature of the surrounding atoms. For piezoelectric materials, XAS experiments were mainly performed to analyze the local site symmetry and bond lengths of the main elements. For example, there are studies on the local atomic environment of Ti and Zr in PZT [Cao04, Ved98] or Bi, K and Ti in BNT and KNN [Lem07, Shu05].

Although the sensitivity of XAS is high enough to probe minor elements, it was rarely used for the examination of dopant sites in perovskites. In 2000, Davies and his group demonstrated the feasibility of XAS for the determination of dopant sites in a perovskite doped with low concentrations of Nd and Yb [Dav00]. Several years later, two studies investigated the dopant site selectivity of Mn in PZT [Lim07, Che08b].

An alternative method, electron paramagnetic resonance (EPR), was recently adapted for the characterization of dopant sites and dipole formation in lead-free ferroelectrics [Eic11]. It was successfully applied to lead-free BNT and BNT-BT-BKT doped with Fe and Cu [Aks10a, Jo11]. While this method offers a very high sensitivity, it is inherently limited to dopants with unpaired electrons.

## 2.3 Sintering

The heat treatment process in which a compacted powder (green body) is turned into a ceramic material is referred to as *sintering*. The powder particles are joined together and the porosity is removed, thereby leading to consolidation and shrinkage of the material.

The driving force for sintering is the minimization of surface free energy of the green body. This can be accomplished by densification and coarsening via atomic diffusion and evaporation and condensation, either in the solid material ('solid state sintering') or assisted by a liquid phase ('liquid-phase sintering'). The diffusion may occur on the particle surface, along grain boundaries or through the crystal lattice. The sintering rate is controlled by the slowest diffusing species, which limits the matter transport. Crystal defects such as vacancies, but also liquid films wetting the grain boundaries that lower the activation energy for diffusion can accelerate the sintering process.

### 2.3.1 Sintering Stages

The solid state sintering process can be divided into three major stages (Figure 2.7). In the initial stage, inter-particle neck-growth reduces the large differences in surface curvatures and leads to a beginning densification. At approx. 3 % to 5 % linear shrinkage, when the pores have reached their equilibrium shape, the intermediate sintering stage with rapid densification sets in. At the beginning, the pores are connected by an open 'spaghetti-like' pore system. Their size is gradually reduced by matter transport until isolated pores are pinched off, which occurs roughly at 90 % of the theoretical density. In the following final stage, the pores continue to shrink. The free energy is further reduced by coarsening of both grains and pores.

As mentioned above, liquid-phase sintering leads to enhanced densification. The liquid film reduces friction between the particles, allowing for enhanced particle rearrangement under the induced capillary stress gradients. This process occurs in the first sintering stage. In the intermediate stage, the densification benefits from the enhanced matter transport through the liquid (e.g. by solution and precipitation). The residual porosity is reduced in the final sintering step. The liquid usually consists of a molten sintering aid or involves components from the bulk material due to eutectic melting. It typically amounts to less than a few vol %. Good wetting of the solid, that is, a low dihedral angle, is essential. Liquid-phase sintering is employed to enhance the densification rate and lower the sintering temperatures or to accelerate grain growth.

Detailed discussions of solid state sintering can be found in textbooks, e.g. [Ger96, Rah03], for liquid-sintering cf. [Ger85].

### 2.3.2 Sintering of Lead-Free Ferroelectrics

As mentioned before, sintering both KNN [Du06] and BNT [Hir09] to useful densities requires temperatures above 1100 °C. Besides the undesirable issue of high energy consumption, the high temperatures lead to the vaporization of alkali oxides [Ski07] and bismuth

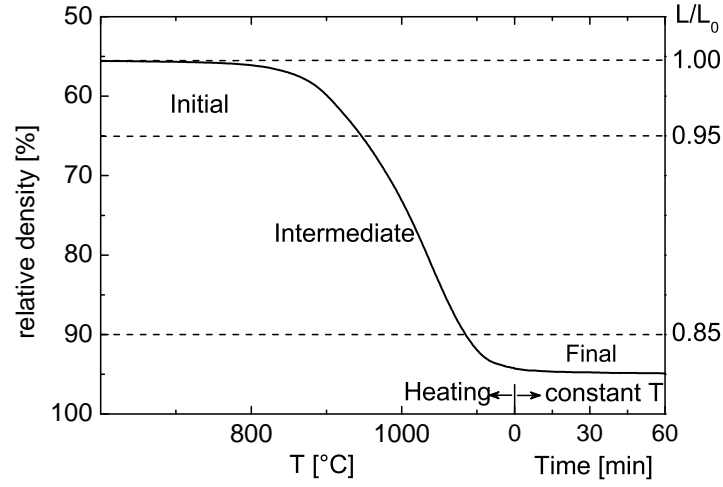


**Figure 2.7:** Sintering stages in a BNT shrinkage curve with constant heating rate and subsequent isothermal sintering.  $L/L_0$  = relative sample width,  $L_0$  = initial sample width,  $L$  = sample width at the respective temperature.

oxide [Hir09]. The resulting nonstoichiometry causes the dielectric and piezoelectric properties to degrade. This effect can be reduced by adding the volatile components in excess before sintering [Ack10, Wan05]. Another approach is to saturate the sintering atmosphere [Wan08] with the respective component.

A further common method to enhance densification involves sintering aids, such as CuO, which induce liquid-phase sintering and reduce the required sintering temperature. However, if too much CuO is added, abnormal grain growth promoted by the liquid phase can occur [Wan12, Jo11] and the piezoelectric properties degrade [Che07, Cho11]. In the case of BNT, a dramatic decrease of the sintering temperature was achieved by the addition of 0.075 mol %  $\text{Fe}_2\text{O}_3$  as sintering aid [Wat07]. The side-effects, however, were a high electrical conductivity and a decreased piezoelectric coefficient [Aks12].

Other methods such as hot-pressing, reactive templated grain growth or chemical vapor deposition were also explored (for a summary, cf. [Röd09]). However, the improvement in properties was fairly low and did not outweigh the high production cost of these methods.

## 3 Experimental

The first part of the following chapter gives details about the methods used to characterize the final ceramic specimens as well as samples in intermediate processing stages, beginning with the raw materials. In the second part, the synthesis route itself and the choice of the respective parameters for each step are explained in detail.

### 3.1 Characterization Methods

#### 3.1.1 Particle Size Measurement

The particle size of the raw materials and of the green powders strongly affects the calcination and sintering properties and should thus be controlled. The laser diffraction technique is a quick way for determining particle sizes down to 0.1  $\mu\text{m}$ , while requiring only small amounts of sample powder.

The scattering of light of a focused laser beam directed through a particle suspension depends on the refractive index gradient of the sample and the solvent, the particle size and the volume of particles of equal size. Using Mie theory [Mie08], a particle size distribution can be determined from the scattering pattern.

The particle size analyses were carried out on a Mastersizer S (Malvern, Worcestershire, UK). The powder samples were suspended in isopropanol and further dispersed using ultrasound to break soft agglomerates. Due to the strong dependence of the scattering power on the volume of the scattering particles, laser diffraction instruments usually report the volume of particles in each size class. Thus, the  $D_{v,50}$  represents the median particle size of the *volume* based particle size distribution.

#### 3.1.2 Powder X-ray Diffraction

Powder X-ray diffraction (XRD) is a powerful tool for phase identification in crystalline solids. A monochromatic X-ray beam is reflected by a crystal only at specific angles depending on its symmetry and lattice parameters. For powder diffraction, the reflecting conditions are described by Bragg's law

$$n\lambda = 2d_{hkl}\sin\theta \quad (3.1)$$

where  $\lambda$  is the wavelength of the X-rays,  $n$  is an integer,  $d_{hkl}$  is the spacing of the  $(hkl)$ -lattice planes, and  $\theta$  is the angle between the incident radiation and the lattice planes. The difference in travel path lengths experienced by X-rays that are reflected at a set of lattice planes must be equal to an integer multiple of  $\lambda$  to obtain constructive interference (see also Figure 3.1). In any other case destructive interference will lead to an extinction of the X-ray beam.

In a powder diffractogram, which usually shows the diffracted intensity  $I$  over the diffraction angle  $2\theta$ , the angles at which the beam is reflected are the so called peak positions. They depend solely on the specific dimensions and symmetry of the crystal lattice, while the intensity of a reflection contains information about the chemistry of the crystal. The resulting diffraction patterns are unique and can therefore be used as ‘fingerprints’ to identify crystal phases in powder samples.

XRD measurements can be done fairly quickly, the sample preparation is easy and requires only very little powder material. This makes the technique suitable to analyze the phase composition of BNT samples after calcination or sintering.

In this work, the XRD patterns were recorded using a D5005 (Siemens, Munich, Germany) with a copper anode ( $K\alpha$  radiation). It is equipped with a  $K\beta$ -filter and a system of several divergence slits. In addition, a Goebel mirror was used to produce a highly parallel X-ray beam. Sintered samples were crushed and ground with an agate mortar and pestle and then mixed with ethanol to produce a homogeneous slurry. The slurry was applied to a flat sapphire disc. Upon drying, a thin, flat powder layer formed, which is sufficient to obtain good X-ray diffractograms. Powder samples were also ground manually prior to the slurry preparation to ensure a sufficiently small grain size even in calcined samples.

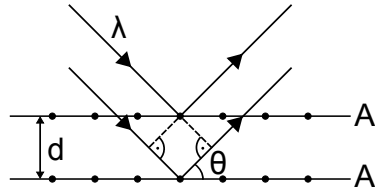


**Figure 3.1:** Bragg’s law reflection. The incident X-rays having a wavelength  $\lambda$  are reflected at a set of crystal planes (A, A’) with distance  $d$  at the incident angle  $\theta$ . The difference in travel paths is equal to an integer multiple of  $\lambda$ , which leads to constructive interference.

### 3.1.3 Differential Thermal Analysis

During the calcination and sintering processes ceramics can undergo for example phase transitions, decomposition and oxidation reactions or chemical reactions between various phases. These (exo- or endothermic) events can be detected using differential thermal analysis (DTA) combined with thermogravimetry (TG) and a mass spectrometry (MS). In DTA, the temperature difference between the sample and a thermally inert material is

measured during heat treatment. The weight change of the sample is recorded simultaneously. In addition, volatile reaction products can be identified with a mass spectrometer attached to the DTA instrument.

The DTA measurements were carried out using a Netzsch STA 449 C Jupiter system (Netzsch, Selb, Germany) combined with a Netzsch QMS 403 C Aeolos Quadrupole Mass Spectrometer. The sample holders were made of  $\text{Al}_2\text{O}_3$ . For measurements involving MS, Ar gas was chosen as inert atmosphere. Other experiments were conducted in synthetic air to reproduce the conditions during calcination and sintering.

### 3.1.4 Density Measurement

The density of the sintered samples was determined by the Archimedes method (according to EN 993-1). When a body is immersed in a liquid, it is buoyed up by a force equal to the weight of the fluid it actually displaces. Thus, by weighing the sample in air and in a liquid medium, its mass and volume can be obtained.

For this study, distilled water was used as liquid. In samples with low density, open pores were considered by additionally weighing the water-infiltrated sample.

### 3.1.5 Scanning Electron Microscopy

The microstructure of fine powders and ceramics can be scrutinized using scanning electron microscopy (SEM). The sample surface is scanned by a focused electron beam in a raster scan pattern. Images are obtained from secondary electrons which are generated during the inelastic interaction of the primary electrons and the sample, as well as from elastically backscattered electrons.

The contrast from secondary electrons (SE) is primarily due to differences in the topography, depending on the surface orientation relative to the SE detector. The backscattering contrast reveals differences in the effective atomic number  $Z$ , since heavier elements reflect electrons more strongly than lighter elements.

Through inelastic interaction of electrons with the sample, characteristic X-ray radiation is generated. It can be analyzed using energy-dispersive (EDX) spectrometers and thus allows for a qualitative as well as quantitative chemical analysis of the sample. This can be exploited to identify secondary phases.

SEM images were taken using a Supra 25 (Carl Zeiss AG). Powder samples were applied to an adhesive conducting carbon pad on an aluminum sample holder. Sintered samples were cut into discs and polished with deionized water and diamond paste. In some cases samples were prepared via cross-section polishing (see Chapter 3.1.5) instead to avoid depletion of possibly solvable ions from the sample during the polishing process or to avoid damage to the green sample microstructure. When necessary, the samples were sputtered with a thin layer of gold.

EDX measurements were carried out using an EDAX Ultra 55 (EDAX Inc., Mahwah, NJ, U.S.A.) detector with Si-crystal and an active area of  $10\text{ mm}^2$ . The detection limit is approx. 0.1 wt % to 1.0 wt %. Standardless quantitative analyses of element concentrations

were done with the software WINEDS (v3.10, Thomson Scientific Instruments) applying ZAF corrections.

### Cross-Section Polishing

Cross-section polishing (CSP) is a sample preparation method for scanning electron microscopy.

A beam of Ar ions is focused on the sample surface which is partly covered by a shielding plate (Figure 3.2). The non-covered surface is ablated and forms a flat cross-section. Unlike common polishing with diamond paste this technique allows for artifact-free sample preparation. In addition, samples of compacted powders like green samples can also be prepared. In porous ceramics, however, the so-called curtaining-effect can cause a slightly uneven sample surface.

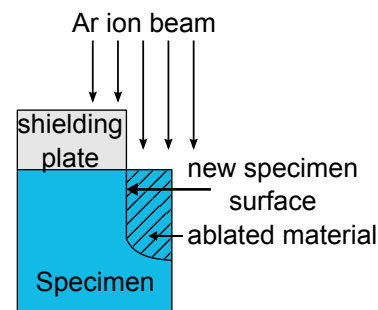


**Figure 3.2:** Schematic of cross-section polishing

### 3.1.6 Electron Probe Micro Analysis

When a quantitative analysis of elements on very small sample areas (e.g. secondary phases in a ceramic) is required, wavelength dispersive X-ray spectroscopy (WDX) is superior to EDX. Its detection limit is an order of magnitude lower than that of EDX since it has a better signal to noise ratio, making it suitable to detect e.g. cobalt in BNT in low concentrations. The main drawback of the method is that only one element per detection unit can be analyzed at a time.

Electron probe micro analysis (EPMA) allows for the simultaneous measurement of up to five elements. In principle, an electron microprobe is similar to a scanning electron microscope. A flat sample surface is hit by a focused electron beam, and the emitted characteristic X-ray radiation is detected on several independent wavelength dispersive spectrometers. These are equipped with single crystals which filter the desired wavelength from the incident radiation exploiting Bragg's law (cf. eq 3.1). The electron microprobe also collects backscattering images (cf. Chapter 3.1.5), thus allowing for the exact placement of the electron beam on the desired sample area.

In this work, the electron microprobe analysis was carried out using a JEOL JXA-8200 (Tokyo, Japan) with five wavelength dispersive X-ray (WDX) spectrometers at the BGI (Bayerisches Geoinstitut), Bayreuth. The Bi  $M\alpha$  and Ti  $K\alpha$  spectral lines were analyzed with a pentaerythritol (PET) crystal, Na  $K\alpha$  with a thallium acid phthalate (TAP) crystal, and Co  $K\alpha$  with a lithium fluorite (LIF) crystal. The measurements were performed at 15 kV and with a 15 nA beam current. For each point, the background was measured for 10 s on either side of the peak, while the counting time on the peak itself was 20 s. When a lower detection limit was desired, these times were doubled. Bismuth and cobalt metal, albite and titanium dioxide were used for calibration. The  $\phi(\rho z)$ -method [Arm88] was applied to quantify the elements.



The diameter of the electron beam was approx.  $1\text{ }\mu\text{m}$ . The information depth, which depends on the acceleration voltage and the effective atomic number  $Z$  of the sample, was less than  $1\text{ }\mu\text{m}$ . It was calculated using Monte Carlo simulations (Electron Flight Simulator v3.1, SPI Supplies, USA).

### 3.1.7 X-ray Absorption Fine Structure

X-ray absorption fine structure (XAFS) spectroscopy is an element specific technique that probes the absorption edge of the desired element to gain structural information about its atomic environment. The method can thus be used to identify the lattice site of an atomic species, e.g. a dopant, in a known matrix.

#### X-ray Absorption in Matter

When matter is hit by X-ray photons, one of three possible interaction mechanisms occurring is the photoelectric effect. When the energy of the photon is equal to or greater than the binding energy of a core electron, the photon can be absorbed completely. The absorbing core electron is excited to a higher, unoccupied electron orbital or even ejected into the continuum with a kinetic energy equal to the excess energy of the photon as compared to the binding energy. The resulting core hole (empty electron orbital) in the atom is subsequently filled by an electron from a higher-energy shell, for example the L- or M-shell. This relaxation process is accompanied by a release of energy in the form of characteristic X-ray radiation or Auger electrons, as shown in Figure 3.3).

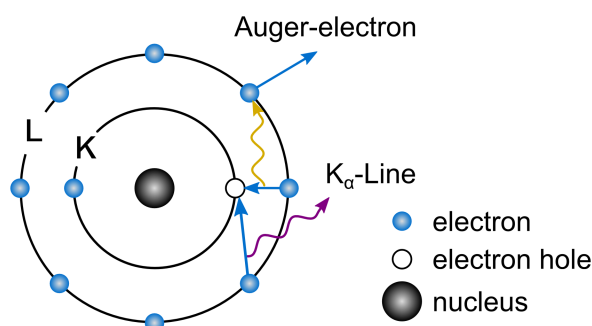


**Figure 3.3:** Relaxation mechanisms in an atom with a core hole in the K-shell: electrons from higher orbitals (here: L-shell) fill the vacancy in the K-shell; the excess energy can either be released in the form of characteristic X-ray radiation, or be transferred to another electron (Auger-electron), which is then emitted from the atom.

The absorption coefficient  $\mu$  describes the probability that a photon is absorbed by matter. It is a function of the incident photon energy and generally decreases with increasing energy. However, when the photon energy reaches the energy required to excite a core electron to an unoccupied electron orbital, the absorption probability increases sharply. This step-like increase is called *absorption edge*. The term *K-edge* refers to core holes generated in the K-shell, an *L-edge* to a hole in the L-shell, and so on.

### X-ray Absorption Spectra

In solids or liquids,  $\mu$  does not decrease monotonically above the absorption edge energy, but oscillates up and down (Figure 3.4). These ‘wiggles’ represent the X-ray absorption fine structure (XAFS). They contain structural information about distance, type and number of the next neighbor atoms around the scatterer.

When the outgoing photo-electron wave is scattered back from the neighboring atoms, it interferes with itself. As the energy of the X-ray photon increases, its wavelength decreases, while the position of the scattering atoms remains constant. As a consequence, the interference periodically changes from constructive to destructive and vice versa. Accordingly, the probability for X-ray absorption, that is,  $\mu$ , increases or decreases, respectively, where the periodicity depends on the distance of the scattering atoms. In addition, the height of the fine structure of  $\mu$  is determined by the number and types of the coordinating atoms.

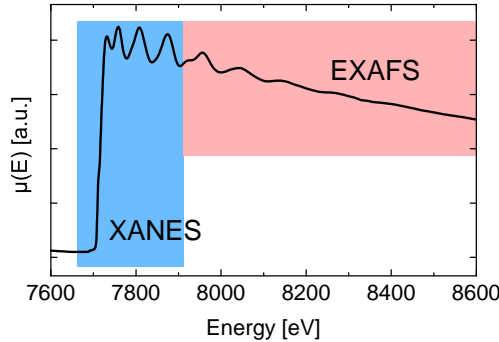


**Figure 3.4:** Absorption coefficient of metallic Cobalt at the K-edge. The absorption coefficient rises sharply at the edge energy (7709 eV), then decreases monotonically with superimposed ‘wiggles’, which reflect the arrangement and atomic species of the next neighbor atoms of the absorber. The blue region is called XANES region (near-edge spectrum), the red one EXAFS (extended XAFS spectrum).

To model the extended X-ray absorption fine structure (EXAFS, 200 eV to 1000 eV above the edge) signal, the so-called EXAFS equation (cf. [Kon88]) is used. Based on a preliminary model of the local atomic environment of the scatterer, the scattering properties of the next atomic neighbors can be calculated (for example using the program FEFF [Reh09]). These parameters are inserted into the EXAFS equation, via which the distance, number and mean-square disorder of the next neighbor atoms can then be determined. Detailed explanations can be found e.g. in [Kon88] or [Kel08].

The X-ray absorption near-edge structure (XANES) from  $-50$  eV to  $200$  eV relative to the absorption edge energy contains information about the valence state and coordination geometry of an element. The shape of this region reflects the density of states available for excited photoelectrons. Often a so-called *white line* is observed, as well as peaks below the actual edge-energy (‘pre-edge peaks’).

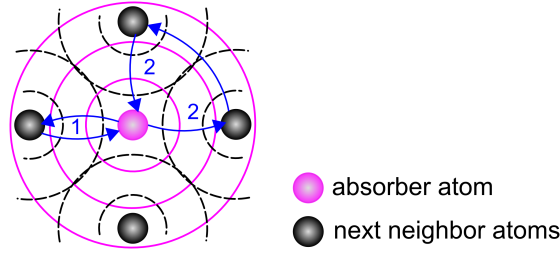


**Figure 3.5:** Scattering of photoelectron-waves at the next neighbor atoms. While it is sufficient to consider single scattering (path 1) for EXAFS, multiple scattering events at several neighbor atoms (path 2) become important in the XANES region.

The kinetic energy of the photoelectrons in the XANES region is rather small. Consequently, multiple scattering effects (Figure 3.5), which can be neglected for EXAFS, become dominant. Various other factors, for example multi body effects, have to be taken into account (see e.g. [Reh00]) as well. As a result, there is no simple analytic description for the XANES signal. However, XANES features are characteristic for a specific material, and the spectra can be used as ‘fingerprints’ for a qualitative analysis. They are first normalized and can then be compared to measured or calculated reference spectra of standard materials. For a quantitative analysis, the reference spectra are linearly combined and fitted to the measured data.

### Measurement Techniques

The absorption coefficient  $\mu$  can be measured in two different ways:

1. The intensity of the X-ray beam is measured directly before and after transmission through the sample using ionization chambers. This is the most common technique. The corresponding experimental setup is called transmission mode. The measured intensity  $I$  at the energy  $E$  can be expressed as

$$I = I_0 e^{-\mu(E)t} \quad (3.2)$$

$$\mu(E)t = -\ln(I/I_0) \quad (3.3)$$

where  $I_0$  is the intensity of the primary beam and  $t$  the sample thickness. This method can be used for element concentrations above  $\approx 10$  wt % and where the sample can be prepared sufficiently thin to obtain a good count rate after transmission.

2. For lower element concentrations or samples which cannot be prepared thin enough, a fluorescence setup can be used. Instead of  $I$ , the fluorescence radiation intensity  $I_f$  produced in the sample is measured. It is proportional to the absorption in the sample:

$$\mu(E) \propto I_f/I_0 \quad (3.4)$$

Here, several corrections e.g. for self-absorption need to be applied during data evaluation.

In this study, the local atomic environment of cobalt was analyzed in fluorescence mode because of the following reasons: For most samples, the concentration of Co in the bulk material was less or equal than 1 wt %  $\text{Co}_3\text{O}_4$ , corresponding to 0.92 wt % Co.  $\text{Bi}_{0.5}\text{Na}_{0.5}\text{TiO}_3$  has a high X-ray absorption coefficient due its high bismuth content. For transmission, a sample would thus have to be highly diluted, leading to even lower concentrations of cobalt atoms, which in turn diminishes the XAFS signal. In addition, the fluorescence setup allows for the use of as-sintered ceramic bulk material, whereas transmission mode would involve crushing and milling the sample material.

### Experimental Setup and Parameters

XAFS experiments are performed at synchrotron facilities, since they can provide the tunable X-ray beam required to probe the absorption edge with sufficiently high intensity. The basic layout of a XAFS experiment in fluorescence mode is shown in Figure 3.6. The white X-ray beam is guided through monochromator crystals which allow to pick the desired wavelength. After collimation, the primary intensity  $I_0$  is measured in an ionization chamber. The fluorescence radiation is detected using scintillation detectors.

In this study, XAFS experiments at the Co K-edge (7709 eV) were carried out at the beamline 7TMPW-MAGS of the BESSY II storage ring (Berlin, Germany). The beamline covers an energy range from 3.5 keV to 30 keV and provides a photon flux of  $2.5 \times 10^{12}$  photons/s/100 mA at 10 keV. The X-ray energy is selected using a Si(111) double crystal monochromator. The energy resolution is approx. 2 eV. A primary ionization chamber and a NaI scintillation detector were used to record  $I_0$  and  $I_f$ . The flat sample surface was orientated at  $45^\circ$  with respect to the beam and the detector.

For non-sintered samples, cylindrical pressed powder pellets with a flat surface were used. Sintered ceramic samples were cut into disks using a diamond saw and then polished manually to obtain a smooth, flat surface.

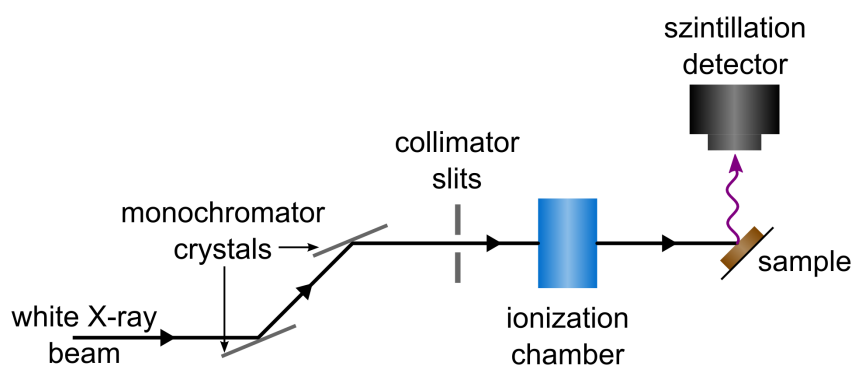


**Figure 3.6:** XANES: Schematic representation of the experimental setup at the MagS beamline at BESSY (Berlin, Germany). The data was collected in fluorescence mode.

XAFS spectra were recorded from 7550 eV to 8300 eV, but only the near-edge region from 7700 eV to 7820 eV could be used due to the low signal to noise ratio. For each sample, three consecutive scans with a counting time of 2 s per step  $\Delta E$  were recorded and the data summed up to improve the signal. The detailed measuring parameters are shown in Table 3.1.

A highly pure cobalt metal foil (99.99 %, Good-fellow) was employed for energy calibration. The recorded spectra were normalized using ATHENA (v0.8.0.61) from the IFEFFIT package [Rav05]. Detector and sample effects as well as effects of self-absorption were removed.  $\mu(E)$  was scaled so that it represents the absorption of a single X-ray and oscillates around 1, making it possible to compare the spectra to ab-initio calculated spectra (cf. Chapter 4.1) or spectra recorded at other light sources.

**Table 3.1:** Parameters for XAFS data collection:

Region	Range [eV]	$\Delta E$
Pre-edge	7550 - 7680	2
Edge, Post-edge	7680 - 8380	0.5

### 3.1.8 Transmission Electron Microscopy

#### Principles of Transmission Electron Microscopy

A transmission electron microscope (TEM) is a versatile tool to investigate materials on the nano-scale, even down to atomic features. Modern TEMs offer resolutions of  $<1 \text{ \AA}$ . The TEM can be used to examine for example the microstructure of a sample, to identify crystal defects or inclusions, or to help distinguish between amorphous and crystalline phases. Qualitative as well as quantitative element analyses with low detection limits and very high spacial resolutions are also possible.

In a transmission electron microscope, a thin sample is penetrated by a high-energy electron beam. Image contrast arises due to the scattering of electrons in the sample:

- Incoherent elastic scattering gives rise to mass thickness contrast. Since the cross section for elastic scattering increases with increasing  $Z$  (effective atomic number), electrons are scattered more strongly. Thicker sample areas also scatter more strongly, because electrons have a longer traveling path through the sample and thus can be scattered more often. Scattering reduces the intensity of the directly transmitted primary beam.
- In crystalline materials, coherent elastically scattered electrons interfere to yield Bragg diffraction patterns, similar to those observed in X-ray diffraction. The symmetry of the crystal as well as its orientation can thus be identified.
- High resolution TEM (HRTEM), a technique to image the crystallographic structure of a material on the atomic level, exploits the phase differences of electron waves scattered through a thin sample. The interference pattern of these diffracted waves is related to the atomic structure of the material. The interpretation is, however, difficult, since the final TEM image depends on many factors.

The above cases represent only a few methods to gain information about a sample using TEM. For an in-depth treatment of the topic, see e.g. the textbook by Williams and Carter [Wil09].

A TEM can also be operated in scanning mode (STEM), like SEM, that is, the image is generated by scanning a certain sample area and collecting the image information electronically.

EDX analyses are often carried out in STEM mode. The excellent spacial resolution is limited mainly by the beam diameter, surpassing that of EPMA by about two orders of magnitude. Compared to EPMA or SEM there is less electron scattering because of the thin sample and the high energy of the electrons (i.e., increased mean free paths). However, scattered electrons and X-ray radiation from other parts in the TEM or the sample may generate undesired EDX background signals.

In summary, TEM allows to investigate materials on a nano-scale. Using various imaging and detection techniques, a lot of diverse information can be gained about the same, very small sample area. The main drawbacks of TEM (besides the high instrument price) are a the laborious sample preparation, possible radiation damage to sensitive materials and in some cases a difficult image interpretation. In addition, only a small sample area can be investigated at a time.

## Instrumentation and Experimental Parameters

TEM studies were carried out using a JEM2011 by Jeol (Tokyo, Japan) operating at an acceleration voltage of 200 keV. The electron source consisted of a LaB<sub>6</sub> crystal (thermionic source). A STEM generator and a EDX detector (EDAX, USA), were attached to the system. A specimen from the sintered bulk sample was prepared as follows: a thin slice ( $\sim 20\ \mu\text{m}$ ) was cut from the middle of a cylindrical sample using a high precision cutting instrument and glued to a copper grid. Low angle ion milling was used for final thinning. The powder sample was mixed with epoxy, formed to a cylinder and then treated similar to the sintered material.

### 3.1.9 Thermo-Optical Dilatometry

During the heat treatment of materials, dimensional changes occur, e.g. due to thermal expansion, sintering or binder burnout. These changes can be observed using in situ dilatometry. In conventional push-rod dilatometers, the sample is in mechanical contact with a rod that transmits the dimensional changes during heating. As a consequence, the sample is continuously exposed to a small force. This can lead to an undesired additional artificial deformation of soft materials or of samples undergoing liquid-phase sintering. Although a special vertical geometry can avoid these effects, the physical contact is still required. Thermo-optical dilatometry, however, is a non contact method. Thus, any influence on the sintering behavior which may be caused by a push-rod can be avoided. Figure 3.7 shows the schematics of TOM, a thermo-optical measuring device developed at Fraunhofer ISC (Wuerzburg, Germany), which was used in this work [Rae01, Rae09a].

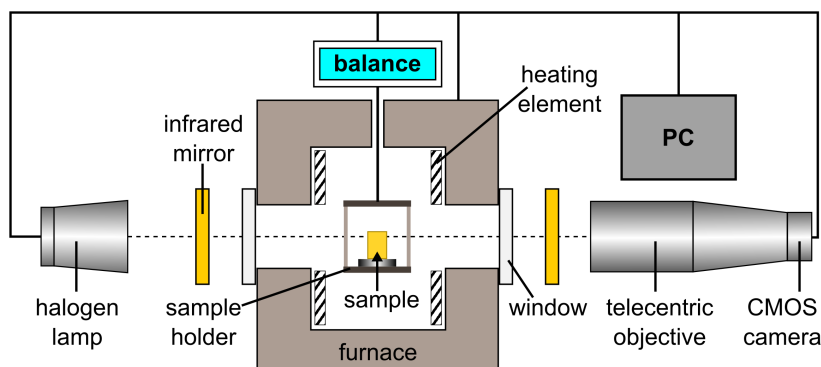


**Figure 3.7:** Schematics of the TOM furnace. The sample is suspended from a balance into the furnace chamber, which possesses two windows on an optical axis. The shadow cast by the illuminated sample is collected by a telecentric objective and camera.

It consists of a high temperature furnace equipped with two transparent quartz windows which lie on the optical axis of a CMOS camera with telecentric optics. The sample shadow is projected onto the camera using a halogen lamp at the opposite side of the furnace (at higher temperatures, the thermal emissions of the sample are sufficient to obtain an image). A software algorithm tracks the contour of the sample during heat treatment and calculates the relative dimensional changes. The TOM instrument achieves a high resolution of  $1\ \mu\text{m}$  and has an excellent reproducibility, especially at convex surfaces.

The furnace features a balance for the in situ measurement of weight changes. An alumina cage, which is suspended from a balance on top of the furnace, is then used as sample holder. The balance signal is recorded by the TOM software simultaneously with the shrinkage data.

The in situ technique makes TOM suitable for a variety of experiments. For instance, load sintering experiments can reveal the presence of a liquid phase during sintering. For these measurements, a small weight is applied to the top of the sample using an alumina plate. Special punches with V-shaped extensions placed below and on top of the green body ensure an exact determination of the sample height, even if slight tilting of the setup occurs during the measurement [Bab07].

The melting point of a compound or powder mixture can also be determined visually in TOM. The wetting behavior of the resulting melt on any desired substrate can then be characterized by measuring the dihedral angle. The knowledge of these properties is especially useful for liquid-phase sintering processes.

The TOM furnace operates in air with a gas flow of  $10\ \text{l min}^{-1}$ . The  $\text{MoSi}_2$  heating elements can generate a maximum temperature of  $1750\ ^\circ\text{C}$ , which is measured by a thermocouple close to the sample position.

BNT sinters at temperatures below  $1200\ ^\circ\text{C}$ . A type S thermocouple (PT-10 %Rh/Pt) offers the best sensitivity for the relevant temperature span and was thus used for the furnace temperature control. The thermocouple was calibrated to the melting point of Au at  $1064\ ^\circ\text{C}$ . A small piece of Au metal foil was slowly heated in TOM and the melting point

was determined visually. The BNT samples were sintered on a thin, flat  $\text{Al}_2\text{O}_3$  substrate, which was placed on a thicker aluminum plate. This was necessary since at high sintering temperatures (roughly above  $1100^\circ\text{C}$ ) the samples tended to cake to the aluminum sheet.

### 3.1.10 Dielectric and Piezoelectric Properties

Piezoelectric ceramics can be characterized by several dielectric and piezoelectric parameters, such as the relative permittivity  $\varepsilon$ , the loss tangent  $\tan \delta$ , the piezoelectric coupling coefficients  $d_{ij}$  or the Curie temperature (see also Section 2.1). In this study, the effect of cobalt doping on the piezoelectric coefficient  $d_{33}$  and the dielectric properties  $\varepsilon$  and  $\tan \delta$  were measured. Finally, the depolarization temperature  $T_d$  was derived from the dielectric measurement (cf. Chapter 4.3). The measurements were carried out at the EPFL in Lausanne, Switzerland.

#### Sample Preparation and Poling

Ceramic discs with a diameter of 12 mm and a thickness of 1 mm were cut from sintered cylinders with a height of 20 mm and slightly polished to obtain flat, parallel surfaces. Both surfaces were then completely coated with sputtered-on chrome-gold electrodes. Up to 5 samples were poled simultaneously in a silicon oil bath at  $60^\circ\text{C}$ . The DC electric field was slowly increased in steps of 1 kV to a maximum field of 6 kV, held constant there for 3 min and shut down slowly, before cooling down the samples to room temperature. After poling, all samples were allowed to age for at least 24 h before any properties were measured.

Some of the highly doped samples did not survive the poling process, because their electric breakdown strength was insufficient. Other doped samples suffered from high leakage currents, which also limited the applicable poling field. As a consequence, the material might not have been fully poled.

#### Dielectric Measurement

The temperature-dependent dielectric properties, that is, relative permittivity  $\varepsilon$  and loss tangent  $\tan \delta$  were determined from room temperature to  $550^\circ\text{C}$  using an LCR-Bridge (HP4284). The dielectric permittivity can be derived from the capacitance  $C$  by

$$C = \varepsilon_0 \varepsilon A / t \quad (3.5)$$

where  $A$  is the electrode area,  $t$  the thickness of the sample, and  $\varepsilon_0$  the permittivity of vacuum ( $8.8514 \times 10^{-12} \text{ F m}^{-1}$ ). The samples were placed on a platinum sheet on a covered hot stage and connected with a platinum wire at the top electrode. A small force was applied by a spring to ensure good contact to the sample electrodes. A thermocouple placed close to the sample recorded the temperature.



### Piezoelectric Measurements

The longitudinal piezoelectric coefficient  $d_{33}$  can be measured using the direct piezoelectric effect. When a stress  $\sigma_3$  is applied to the material, a corresponding dielectric displacement  $D_3$  occurs:

$$D_3 = d_{33}\sigma_3 \quad (3.6)$$

The quasistatic Berlincourt-Type [Jaf71] press method measures the charge  $Q_s$  created by the applied stress:

$$D_3 = Q_s/A \quad (3.7)$$

where  $A$  is the electroded area of the sample. A reference sample with known piezoelectric  $d_{33}$  is subjected to the same force. The generated charge  $Q$  is measured on both the sample and the reference using parallel sensing capacitors as shown in Figure 3.8. Since

$$Q = VC \quad (3.8)$$

and  $C_S/C_R$  can be set to unity, the longitudinal piezoelectric coefficient can be derived as

$$d_{33S} = d_{33R} * (V_S/V_R) \quad (3.9)$$

The static force was applied by a round surface contact, so that a point contact was produced instead of an area contact. This is done to avoid clamping effects in the sample due to friction [Bar04].

An additional slowly alternating force was applied by an actuator, which was driven by a sinusoidal signal of 200 Hz. The generated voltages were measured using an oscilloscope.

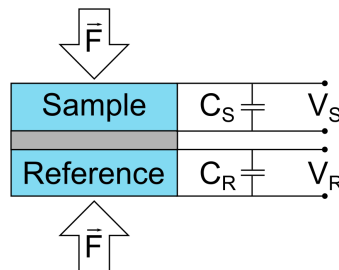


**Figure 3.8:** Schematics of the Berlincourt-type setup used to measure  $d_{33}$

## 3.2 Synthesis of BNT

Bismuth sodium titanate,  $\text{Bi}_{0.5}\text{Na}_{0.5}\text{TiO}_3$  (BNT), can be synthesized from oxide powders using the well established solid state route. The following sections describe the raw materials, the details of the synthesis process, and the chosen parameters for calcination, green body forming and sintering.

### 3.2.1 Synthesis Route

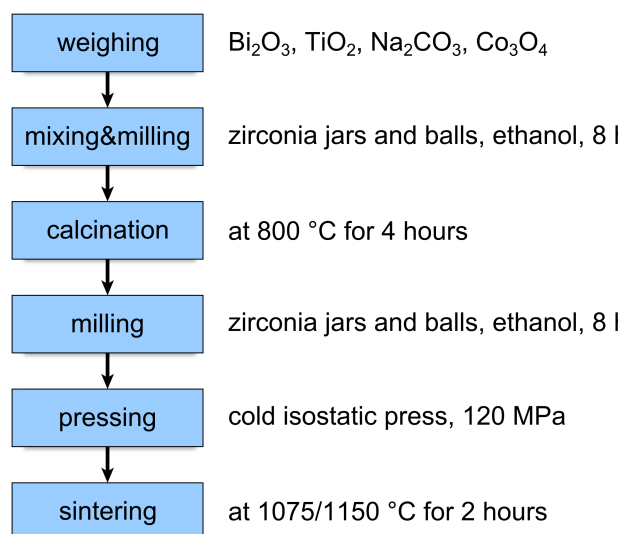
Bismuth sodium titanate was synthesized via a solid state reaction mechanism. The key step is the heat treatment of the oxide powder mixture, which induces a decomposition of the carbonate and a chemical reaction between all components. It is also referred to as *calcination*.

Figure 3.9 shows the individual processing steps of the BNT synthesis from the starting oxides to the finished ceramic specimen.  $\text{Bi}_2\text{O}_3$ ,  $\text{TiO}_2$ ,  $\text{Na}_2\text{CO}_3$ —and, in the case of doped BNT,  $\text{Co}_3\text{O}_4$ —were weighed in stoichiometric amounts and filled into zirconia jars (500 ml). 70 ml of ethanol and 400 g of zirconia milling balls ( $\varnothing$  5 mm) were added. The mixture was homogenized in a planetary ball mill (Pulverisette 5, Fritsch, Idar-Oberstein, Germany) for 8 h at 150 rpm. After removal of the milling balls, the slurry was dried at 55 °C and ground slightly with an agate mortar and pestle. A fixed amount of the powder mixture was filled into an alumina crucible. It was covered with a lid to keep the atmosphere constant for each calcination and to avoid contamination. The calcination was carried out at 800 °C in muffle furnaces. The heating rate was 5 K min<sup>-1</sup>, the dwell time was 4 h.

The calcined powder was slightly crushed with an agate mortar and pestle and then ground for 8 h in the planetary ball mill under the same conditions as for the mixture of raw materials. The mean particle size  $d_{50}$  was 0.92  $\mu\text{m}$ . After subsequent drying at 55 °C and manual grinding, the finished powder was heated to 130 °C for at least 24 h to remove any moisture. It was precompacted manually with a glass rod in a cylindrical shaped silicone mold and compacted in a cold isostatic press (KIP E500, Paul-Otto Weber, Germany) at 120 MPa, yielding a green density of 60 %. The final dimensions of the green bodies were  $\varnothing = 9$  mm with a height of 10 mm and  $\varnothing = 13$  mm with a height of 20 mm. Sintering was either carried out in air in a muffle furnace (NH/11, Nabertherm, Lilienthal, Germany) or in a TOM furnace. The sintering temperatures were 1000 °C, 1075 °C and 1150 °C, respectively. Unless stated otherwise, the heating ramp was 5 K min<sup>-1</sup> and the samples were allowed to cool naturally. The samples were then cut into discs using a precision saw (Accutom 50, Struers, Willich, Germany) with a diamond cutting wheel, and prepared for the individual characterization methods such as XRD, SEM or XANES (see Chapter 3.1).

### 3.2.2 Choice of the Dopant Oxide

For cobalt doping, several cobalt oxides are available. The most stable oxide at ambient conditions is the mixed-valent oxide  $\text{Co}_3\text{O}_4$ . It is reduced to the divalent oxide  $\text{CoO}$  at 900 °C in air [Hol95, Che03]. Although  $\text{CoO}$  is also stable at room temperature, it is



**Figure 3.9:** Synthesis steps for BNT applied in this thesis

oxidized to  $\text{Co}_3\text{O}_4$  when heated above 400 °C. The trivalent oxide  $\text{Co}_2\text{O}_3$  is not available as single phase material.

For this study,  $\text{Co}_3\text{O}_4$  was added to the starting mixture. Initially, the ceramic was also synthesized using  $\text{CoO}$  at the same concentration as  $\text{Co}_3\text{O}_4$  to investigate the influence of the cobalt oxidation state, but no differences were observed. DTA experiments showed that  $\text{Co}^{2+}$  is simply oxidized to  $\text{Co}^{3+}$  below the formation temperature of BNT.

### 3.2.3 Raw Material Characterization

The solid state reaction route requires metal oxide or carbonate powders as starting materials. Some properties of the starting powders, such as purity, grain size, and agglomeration behavior can have a significant influence on the synthesis parameters. In addition, they affect the properties of the final ceramic material directly (especially impurity atoms) as well as indirectly (via the required mixing and heat treatment steps). The raw materials thus need to be well characterized.

Table 3.2 gives an overview over the oxide powders used as starting materials for the BNT synthesis. The purity of all powders was at least 99.7 % or higher. The impurities and original particle sizes are listed in Table A.1 in the appendix. Since not all powders were available with a sufficiently small particle size ( $\sim 1 \mu\text{m}$ ), an additional milling step was necessary.

The size of the  $\text{Bi}_2\text{O}_3$  particles is critical for the calcination process [Aks10c]. Small particles are desired to reduce the diffusion path lengths for the other elements into BNT. The phase formation is accelerated and the dwell time for the calcination can be reduced considerably. For this reason,  $\text{Bi}_2\text{O}_3$  was ground separately in the planetary ball mill for 8 h in ethanol (zirconia jar and balls). Subsequent grain size measurement (laser diffraction)

**Table 3.2:** Starting powders for BNT synthesis:

Powder	Bismuth oxide	Rutile	Sodium carbonate	Cobalt oxide
Chemical formula	$\text{Bi}_2\text{O}_3$	$\text{TiO}_2$	$\text{Na}_2\text{CO}_3$	$\text{Co}_3\text{O}_4$
Purity	99.975 %	99.8 %	99.95 %	99.7 %
Particle size	$d_{50} = 1.0 \mu\text{m}$ $d_{90} = 2.1 \mu\text{m}^{\text{a}}$	$0.9 \mu\text{m}$ to $1.6 \mu\text{m}$	ca. $1 \mu\text{m}^{\text{b}}$	$d_{50} = 1.1 \mu\text{m}$ $d_{90} = 9.7 \mu\text{m}^{\text{c}}$
Supplier	Alfa Aesar <sup>d</sup>	Alfa Aesar <sup>d</sup>	Acros Organics <sup>e</sup>	Alfa Aesar <sup>d</sup>

<sup>a</sup> milled in planetary ball mill

<sup>b</sup> after mixing and milling with the other oxide powders

<sup>c</sup> milled in vibrating disc mill

<sup>d</sup> Alfa Aesar GmbH, Karlsruhe, Germany

<sup>e</sup> Acros Organics, Geel, Belgium

yielded a  $d_{50}$  of  $1.0 \mu\text{m}$  and a  $d_{90}$  of  $2.1 \mu\text{m}$ , close to the size of the  $\text{TiO}_2$  particles.

The dopant particles need to be finely dispersed in the other oxides to ensure a homogeneously doped mixture. Thus, the size of the  $\text{Co}_3\text{O}_4$  particles (initially -325 mesh, that is, particles of up to  $37 \mu\text{m}$  can occur) was reduced as well. The powder was milled with a vibrating disc mill (Pulverisette 9, Fritsch, Germany) in a tungsten carbide grinding set (the powder quantity was too small for the available planetary ball mill).

SEM images of the individual powders after milling are shown in Figure 3.10. The particle size  $d_{50}$  of the milled powder mixture was  $1.1 \mu\text{m}$ , with a second small fraction of larger particles ( $d_{90}$  of  $9.7 \mu\text{m}$ ).

### 3.2.4 Calcination Parameters

In the literature one finds a lot of different calcination procedures for bismuth sodium titanate. Some of these do not lead to single phase BNT powders [Spr04]. Thus, different time-temperature programs were carried out for this study to determine the optimal calcination conditions with respect to the used raw materials (shown in Table 3.2). BNT powder mixtures (pure BNT and BNT doped with 2.6 mol % Co) were heated in a muffle furnace with a heating rate of  $5 \text{ K min}^{-1}$ . The dwell temperature was between  $600^\circ\text{C}$  and  $800^\circ\text{C}$ , with a holding period of 4 h. Figure 3.11 exemplary shows the X-ray diffractograms of the powder with 2.6 mol % Co calcined at different temperatures. While there are still reactants present at  $600^\circ\text{C}$ , no secondary phases were detected after a calcination at  $650^\circ\text{C}$ . This is in accordance with the results of Aksel et al. [Aks10c] for pure BNT. However, DTA experiments showed that  $\text{CO}_2$  kept evaporating from the mixture up to  $700^\circ\text{C}$ . Spreitzer et al. [Spr07] observed that BNT initially forms with a Na deficit, but continues to react

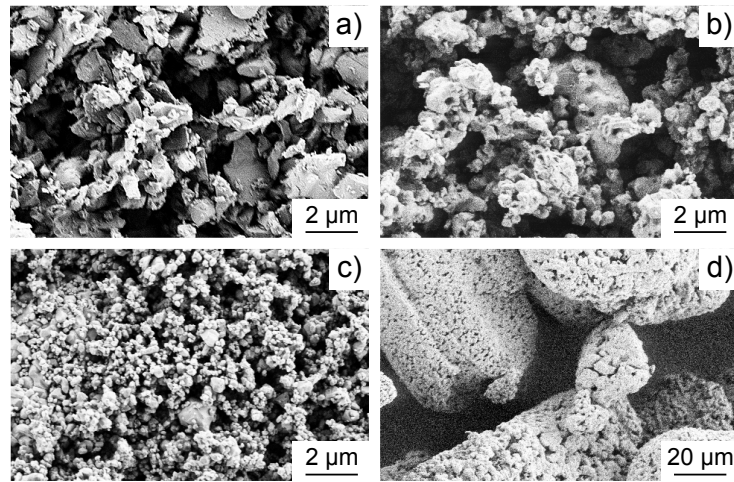


**Figure 3.10:** SEM images of the starting oxides: a)  $\text{Bi}_2\text{O}_3$  (after milling), b)  $\text{TiO}_2$ , c)  $\text{Co}_3\text{O}_4$  (after milling), d)  $\text{Na}_2\text{CO}_3$ .

to stoichiometric BNT after prolonged soaking times or higher temperatures. Considering these results, the calcination parameters for this study have been chosen as  $800^\circ\text{C}$  with a 4 h soaking time to allow for a complete formation of stoichiometric BNT.

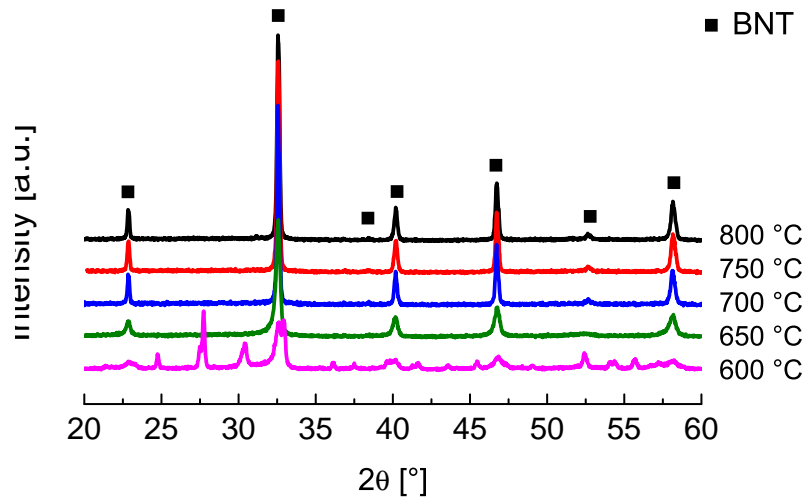


**Figure 3.11:** Powder XRD of BNT with 2.6 mol % Co calcined at different temperatures for 4 h; the formation of BNT without any XRD-detectable secondary phases is finished at  $700^\circ\text{C}$  (measuring time 2 s per  $0.02^\circ$  step).



## 4 Data Evaluation

### 4.1 Simulation of XANES Spectra

Measured XANES spectra can be compared to spectra of known standards (‘fingerprint analysis’, cf. Chapter 3.1.7) to identify the local atomic environment in the sample. However, when no standard spectra are available or it is difficult to synthesize appropriate standard materials, the simulation of XANES spectra based on theoretical ab-initio calculations is a good alternative.

In this work, the FEFF9 code [Reh09] was used to simulate spectra of cobalt on lattice sites in  $\text{Bi}_{0.5}\text{Na}_{0.5}\text{TiO}_3$  and several cobalt oxides which might have formed as secondary phases (see Chapter 5.1).

A cluster of atoms with the absorbing atom at its center is required as input for the calculations. For periodic crystal structures, a list of atoms for a chosen cluster size can be generated using the ATOMS software [Rav01]. The program calculates *xyz*-coordinates based on the space group, lattice dimensions and atomic positions of a crystal structure.

These coordinates are handed to FEFF9, which uses a self-consistent multiple scattering approach to calculate XANES and EXAFS spectra. It employs a full Green’s function for the chosen cluster of atoms. Muffin-tin potentials are used in the iterative calculation of scattering potentials. To account for room temperature conditions, a Debye-Waller factor can be included in the calculations. Details on the crystal structures used in this study can be found in Table A.2.

### 4.2 Thermo-Optical Data Evaluation

#### 4.2.1 Thermal Expansion Correction

The dimensional changes of a green body during sintering occur due to sinter shrinkage as well as due to thermal expansion. The latter contribution is undesired for the analysis of densification behavior and had to be removed from the measured shrinkage. To this end, a pre-sintered BNT sample was heated in TOM (cf. Chapter 3.1.9) at a medium heating rate of  $5 \text{ K min}^{-1}$ . A second order polynomial was fitted to the recorded expansion curve and used to correct the shrinkage data of sintering experiments.

### 4.2.2 Kinetic Field Analysis

The kinetic field diagram was first introduced by Palmour in 1987 [Pal87]. This model-free method is based on large sets of experimental shrinkage data, making it robust and reliable. The kinetic field allows for the calculation of the apparent activation energies for sintering, that is, for grain growth and densification. In addition, the relation between densification and coarsening can be deduced. Furthermore, it can be employed to predict densification rates for arbitrary time-temperature cycles of a specific material, or to calculate the required time-temperature cycle in order to achieve a desired densification rate.

The densification rate for solid state sintering can be described by

$$\frac{1}{3\rho} \frac{d\rho}{dt} = -\frac{d\varepsilon}{dt} = \frac{C_1(\rho)\gamma}{kG^n} \frac{D_0 e^{-E_a/RT}}{T} \quad (4.1)$$

with  $\rho$  = density,  $t$  = time,  $\varepsilon$  = strain,  $C_1$  = constant depending on microstructure,  $\gamma$  = solid-gas interface energy,  $k$  = Boltzmann constant,  $G$  = mean grain diameter,  $n$  = exponent depending on diffusion mechanism,  $D_0$  = diffusion coefficient,  $E_a$  = apparent activation energy (for diffusion and grain growth),  $R$  = gas constant,  $T$  = absolute temperature. For the kinetic field analysis, eq 4.1 is transformed to

$$\ln \left( -T \frac{d\varepsilon}{dt} \right) = \ln \left( \frac{C_1(\rho)\gamma D_0}{k} \right) - n \ln G - \frac{E_a}{RT} \quad (4.2)$$

Assuming the grain size  $G$  changes slowly with time, the activation energy for diffusion can be obtained using an Arrhenius-type plot, the kinetic field diagram, which is shown schematically in Figure 4.1b. The left hand side of eq 4.2 is plotted versus the inverse absolute temperature for various values of  $\rho$ , which are collected during experiments with different heating rates as shown in Figure 4.1a. The points of equal shrinkage (or density) in those curves can be fitted to straight lines, the so called iso-strain lines (or equivalently iso-density lines). Their slope yields the apparent activation energy. Further information about the activation energy for coarsening relative to the one for diffusion can be gained from the rotation of the iso-strain lines [Rae09c].

## 4.3 Determination of Depolarization Temperature

The depolarization temperature  $T_d$  can be defined as ‘the temperature of the steepest decrease of remanent polarization’ [Ant11]. Several different methods were used in the literature to determine  $T_d$ .

In this study,  $T_d$  was derived from the dielectric measurement of the permittivity  $\varepsilon$  and dielectric loss  $\tan \delta$  as a function of temperature (see Chapter 3.1.10). The two parameters are related by

$$\tan \delta = \varepsilon''/\varepsilon'. \quad (4.3)$$



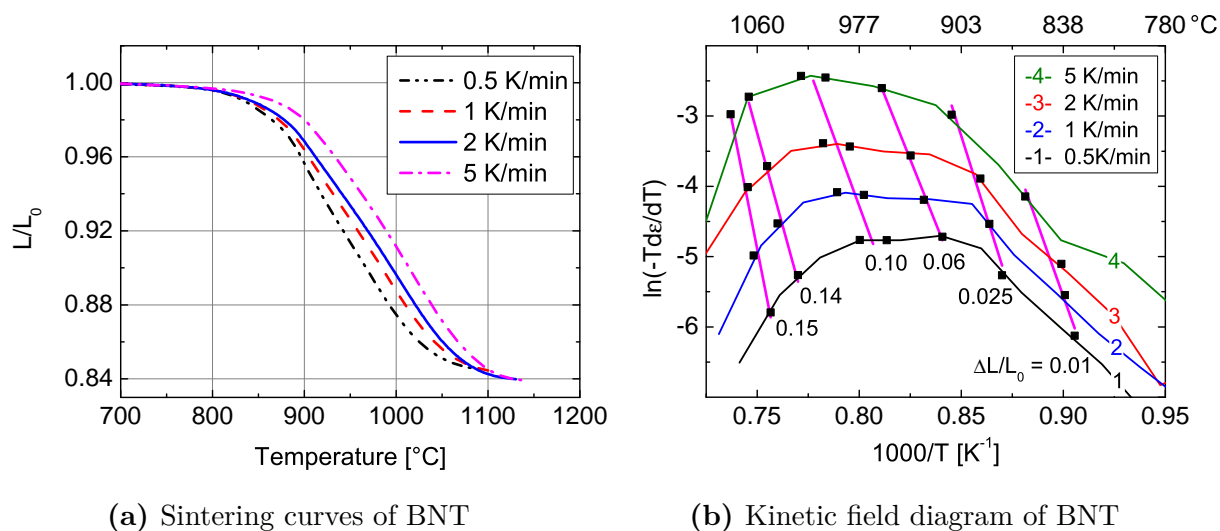


**Figure 4.1:** Construction of (b) the kinetic field diagram from (a) sintering experiments with heating rates from 0.5 K to 5 K. In (b), iso-strain lines were fitted to points of equal strain (black squares).  $\Delta L/L_0$  is the engineering strain derived from the sintering curves.

where  $\epsilon'$  and  $\epsilon''$  are the real and imaginary part of the complex relative dielectric permittivity.

The maximum of the first derivative of  $\epsilon'$ , that is, its inflection point, was taken as depolarization temperature. In samples with high dopant levels, the peak of the first derivative tended to broaden and was completely obscured at low measurement frequencies. In such cases, the first derivative of the imaginary part of the permittivity  $\epsilon''$  was used instead, because it displays the discontinuous change more clearly.



## 5 Local Atomic Environment of Co

The phase formation of cobalt-doped BNT was investigated by means of X-ray diffraction and backscattering SEM. Additional quenching experiments were conducted to gain information about the solubility of Co in BNT. The incorporation of Co in BNT was verified via electron probe micro analysis (EPMA) and scanning transmission electron microscopy combined with energy dispersive X-ray analysis (STEM-EDX). Finally, the lattice site preference of Co was determined by X-ray absorption near-edge structure (XANES) experiments.

### 5.1 Phase Formation in Cobalt-Doped BNT

#### X-ray Diffraction

The formation of BNT from the oxides was presented in Chapter 3.2.4. A pure perovskite phase was obtained after calcination.

The phase compositions of sintered, doped ceramics were determined from crushed and milled powder samples. Si powder was added as internal standard (ca. 25 wt %) to allow for the monitoring of peak shifts and the determination of lattice constants.

Figure 5.1 shows the powder X-ray diffractograms of selected BNT ceramics with various cobalt concentrations. The reflexions of the perovskite phase do not display a detectable shift of peak positions, regardless of the dopant concentration or sintering temperature. The powder XRD pattern of pure BNT sintered at 1150 °C (a) is entirely composed of perovskite reflexions. Similarly, BNT doped with 1.0 mol % Co and sintered at 1075 °C (b) yielded single phase perovskite (within the sensitivity limits of XRD). The diffractograms of BNT containing 2.6 mol % Co (c, d, e), however, show tiny additional reflexions at 35.2° and 42.8°. They occurred at all tested sintering temperatures (1000 °C, 1075 °C and 1150 °C). The corresponding crystal structure was identified as  $\text{Co}_2\text{TiO}_4$ , an inverse spinel, that can form a complete solid solution with  $\text{Co}_3\text{O}_4$  [Yan99].

The  $\text{Co}_2\text{TiO}_4$  reflexions display an extremely low peak/background ratio. When the diffractograms were recorded with shorter measuring times (see inset in Figure 5.1), such as 2 s/0.02°, which is common for routine phase composition analyses, these peaks could not be distinguished from the background noise. This means that they can easily be overlooked, which might have been the case in some of the publications on doped BNT that report single phase perovskite.

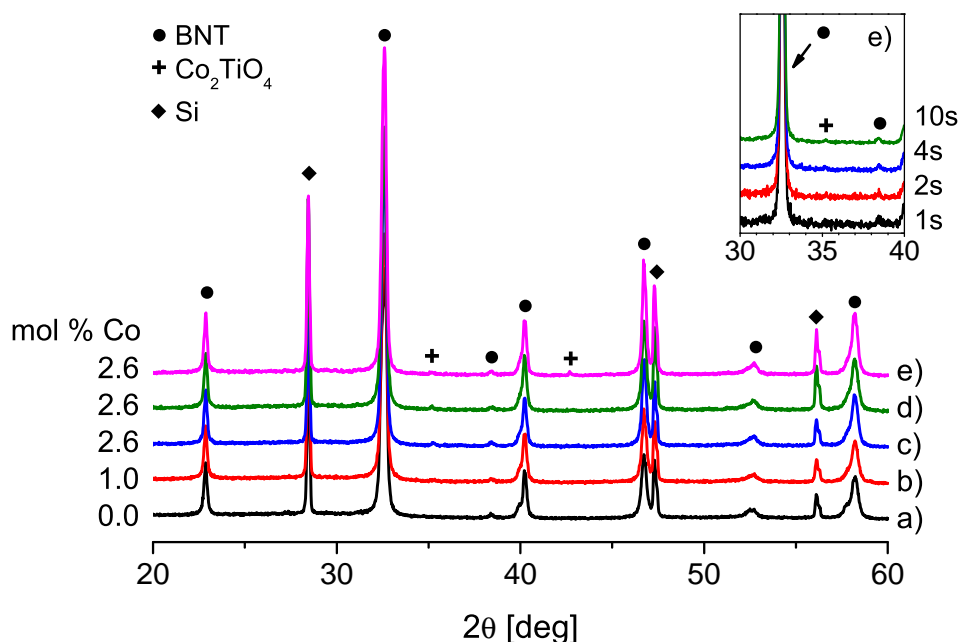


**Figure 5.1:** Powder X-ray diffractograms of sintered BNT ceramics with internal Si powder standard, recorded with 15 s per 0.02°: a) pure BNT, 1150 °C; b) BNT with 1 mol % Co, 1075 °C; c) BNT with 2.6 mol % Co, 1000 °C; d) BNT with 2.6 mol % Co, 1075 °C; e) BNT with 2.6 mol % Co, 1150 °C. The inset shows e) recorded with 1 s, 2 s, 4 s and 10 s per 0.02°.

On this basis, the calcined powders, too, were re-examined using counting times of 15 s/0.02°, but no additional phases were revealed as compared to a counting time of 2 s/0.02°. They can therefore be considered single phase within the limits of XRD sensitivity.

## Scanning Electron Microscopy

Since powder XRD was not sensitive enough to reliably reveal all secondary phases, backscattering SEM (BSD) was chosen to assist in the task. Here, the contrast in the SEM images is due to variations in the effective atomic number  $Z$ , where higher  $Z$  areas appear brighter than those with lower  $Z$  (see also Chapter 3.1.5). Consequently, the contrast between BNT and Bi-free phases is very high. In powder XRD, on the other hand, the heavy-element phase BNT hampers the detection of small quantities of low- $Z$  phases. The BSD images of polished, sintered sample surfaces were examined in combination with EDX, so that the secondary phases could be identified via their atomic fractions.

The results are summarized in Table 5.1. Undoped BNT consisted of the pure perovskite phase, in accordance with XRD. Similarly, BNT doped with the lowest cobalt concentration of 0.1 mol % did not show signs of additional phases.

**Table 5.1:** Secondary phases in sintered BNT ceramics doped with cobalt; phase composition according to EDX analysis:

Cobalt concentration [mol %]	1000 °C	1075 °C	1150 °C
0.1	-	single phase	single phase
0.5	$\text{NaCo}_{0.5}\text{Ti}_{3.5}\text{O}_8^{\text{a}}$	$\text{Co}_2\text{TiO}_4$ $\text{Na}_{0.5}\text{Co}_{0.2}\text{Ti}_{1.7}\text{O}_4$	$\text{Co}_2\text{TiO}_4$ $\text{Na}_{0.8}\text{Co}_{0.4}\text{Ti}_{1.6}\text{O}_4^{\text{b}}$
1.0	$\text{Co}_2\text{TiO}_4$	$\text{Co}_2\text{TiO}_4$ $\text{Na}_{0.6}\text{Co}_{0.2}\text{Ti}_{1.7}\text{O}_4$	$\text{Co}_2\text{TiO}_4$ $\text{Na}_{0.6}\text{Co}_{0.2}\text{Ti}_{1.7}\text{O}_4$
2.6	$\text{Co}_2\text{TiO}_4$	$\text{Co}_2\text{TiO}_4$ $\text{Na}_{0.8}\text{Co}_{0.4}\text{Ti}_{1.6}\text{O}_4^{\text{b}}$	$\text{Co}_2\text{TiO}_4$ $\text{Na}_{0.8}\text{Co}_{0.4}\text{Ti}_{1.6}\text{O}_4^{\text{b}}$
10.6	-	$\text{Co}_2\text{TiO}_4$ $\text{Na}_{1.6}\text{Co}_{0.7}\text{Ti}_{1.2}\text{O}_4$	$\text{Co}_2\text{TiO}_4$ $\text{Na}_{1.5}\text{Co}_{0.8}\text{Ti}_{1.2}\text{O}_4$

<sup>a</sup> Shukaev and Volochaev [Shu95], Freudenbergitte A, x = 0.8

<sup>b</sup> Shukaev and Volochaev [Shu95], Nonstoichiometric ferrititanate structure type, B, x= 0.8

Higher cobalt concentrations triggered the formation of secondary phases. A single secondary phase was detected at a sintering temperature of 1000 °C. At higher sintering temperatures, two secondary phases coexisted. One of them was identified as  $\text{Co}_2\text{TiO}_4$ . It was present down to dopant levels of 0.5 mol %, where it could not be detected using XRD.

The other secondary phase contained Na in addition to Co and Ti. Due to its small grain size, the determined stoichiometry given in Table 5.1 may be inaccurate, especially at low dopant concentrations. The phase compositions resemble two sodium cobalt titanates described by Shukaev and Volochaev in 1995 [Shu95].

Compared with  $\text{Co}_2\text{TiO}_4$ , the sodium-rich phase was only a minor constituent. For example, BNT doped with 2.6 mol % Co and sintered at 1150 °C contained approx. 1.6 vol %  $\text{Co}_2\text{TiO}_4$ , but only 0.3 vol % of  $\text{Na}_{0.8}\text{Co}_{0.4}\text{Ti}_{1.6}\text{O}_4$  (determined via area analysis of SEM BSD images). The overall amount of secondary phase was found to increase with increasing cobalt concentrations.

Figure 5.2 shows the microstructure of BNT doped with 0.5 mol % and 2.6 mol % Co sintered at two different temperatures (1000 °C and 1150 °C). Secondary phase grains are exemplary marked by arrows.  $\text{Co}_2\text{TiO}_4$  mainly formed well-developed grains with straight edges and is located at the intersections of BNT grains (see e.g. Figure 5.2d), but it also occurs as small rounded inclusions in BNT. At 1000 °C, the sodium-bearing secondary phase formed similar crystals, while at a sintering temperature of 1150 °C, it lined the surface of pores like solidified melt (also valid for 1075 °C). Qualitatively, an increase in

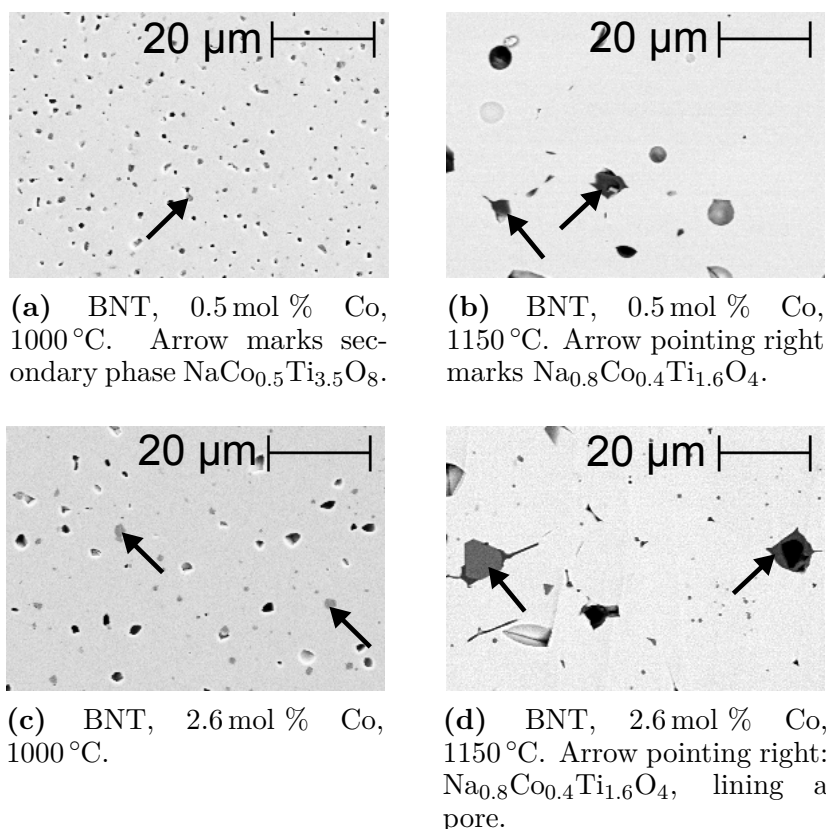


**Figure 5.2:** SEM backscattering images of cobalt-doped, sintered BNT samples (polished surfaces). Bright areas consist of BNT, black spots represent pores. All arrows pointing left mark  $\text{Co}_2\text{TiO}_4$ ; Other arrows: see individual captions.

the mean grain size and a decrease in the number of pores can be observed with increasing sintering temperature. When sintered at 1000 °C, the grains of BNT doped with the higher cobalt concentration grew larger than in the sample with low Co concentration (cf. Figures 5.2a and 5.2c). A systematic study of grain and pore size distribution and mean diameters, though, was beyond the scope of this study.

### Quenching Experiment

As reported above, all BNT ceramics doped with  $\geq 0.5$  mol % Co displayed the formation of at least one secondary phase. It was considered possible that the secondary phase formation stemmed from a cobalt precipitation reaction during the slow cooling process of the sintered samples. This could be the case if the solubility of cobalt in BNT is much lower at room temperature than at the sintering temperature and if the solubility limit was exceeded during cooling. To elucidate this issue, a quenching experiment was conducted.

A green compact of BNT doped with 2.6 mol % Co was heated to 1075 °C under similar conditions as previously sintered samples. After a holding period of 1 h to establish equilibrium conditions, the sample was removed from the furnace. It was immediately dropped

into a large pool of cold water to ensure rapid cooling (within a fraction of seconds) and prevent precipitation. The quenched sample was then prepared for SEM and compared to a conventionally sintered (1075 °C, 2 h) and slowly cooled sample (Figure 5.3). Apart from a slightly smaller average grain size due to the shorter soaking time the samples show a similar microstructure, particularly regarding the abundance and appearance of the secondary phases. These phases were therefore already present at the sintering temperature and did not result from a precipitation effect. The quenched sample was also analyzed for its cobalt content in BNT using electron probe micro analysis (EPMA) (see Chapter 5.2).

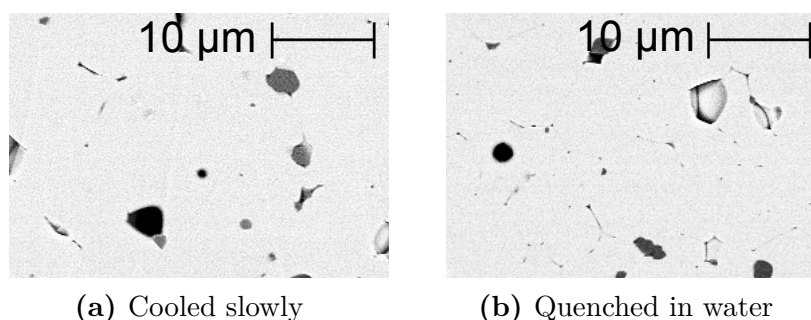


**Figure 5.3:** Quenching effect on BNT doped with 2.6 mol % Co, sintered at 1075 °C. The SEM-BSD images show the polished surfaces.

## 5.2 Incorporation of Co in BNT

Despite the formation of cobalt phases, a fraction of the dopant may have been incorporated into the BNT lattice. This possibility was tested by means of electron probe micro analysis (EPMA), which features wavelength dispersive X-ray spectrometers, and transmission electron microscopy combined with EDX. Both techniques possess a higher sensitivity (factor of ca. 10) for trace elements than conventional SEM-EDX, which turned out insufficient to detect Co in the BNT grains.

### Electron Probe Micro Analysis

Figure 5.4 schematically shows a typical measurement area in an electron microprobe image of BNT doped with 2.6 mol % Co. For the analysis of a single, visually phase pure grain, a set of positions arranged on a grid of at least 6x6 spots was analyzed. Due to the large number of spots, it is very unlikely that invisible  $\text{Co}_2\text{TiO}_4$  grains located beneath the surface of BNT contributed to all of the measured cobalt signals.

The concentration of Co in BNT was analyzed for doping levels of 0 mol %, 0.5 mol %, 1.0 mol %, 2.6 mol % and 10.6 mol % Co. The effect of quenching was also inspected. Figure 5.5 exemplary shows the cobalt concentration measured on seven different grains of BNT doped with 2.6 mol % Co (4 grids, 3 single spot measurements). All recorded values lie well above the mean detection limit of  $(0.07 \pm 0.01)$  mol % Co. The cobalt concentration

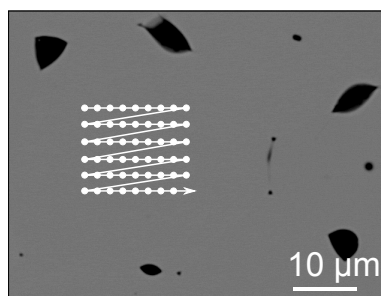


**Figure 5.4:** Electron probe micro analysis measurement procedure. White dots indicate the individual spots of a typical grid measured inside a single grain of BNT. Here: BNT doped with 2.6 mol % Co, sintered at 1150 °C.

varies from grain to grain, but scatters within the expected range (as indicated by the  $\sigma$ -levels) around the mean concentration of  $(0.29 \pm 0.03)$  wt %.

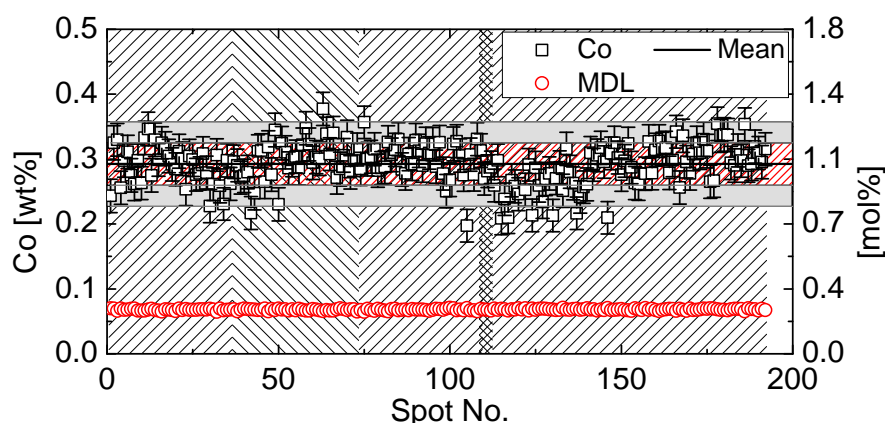


**Figure 5.5:** Quantitative electron probe micro analysis of BNT doped with 2.6 mol % Co (sintering temperature 1150 °C). The figure shows the concentration of cobalt in wt % measured on single phase grains of BNT; the differently hatched areas indicate spots belonging to the same grains (grain 1: spots 1-36, grain 2: spots 37-73, grain 3: spots 74-109, spots 110-112: one grain each, grain 4: spots 113-192). MDL = mean detection limit. Red hatched area = 1<sup>st</sup> sigma level of gauss distribution, grey area = 2<sup>nd</sup> sigma level.

In Figure 5.6, the mean cobalt concentration in BNT is plotted in relation to the initial cobalt concentration. It was above the detection limit for all doped samples and in general increased with increasing dopant levels, except for 1.0 mol % Co. The effect of maximum sintering temperature and cooling conditions was investigated for BNT doped with 0.5 mol % and 2.6 mol % Co. Within the precision of the measurement, the obtained concentrations did not indicate any dependence on the sintering temperature and were not affected by quenching.



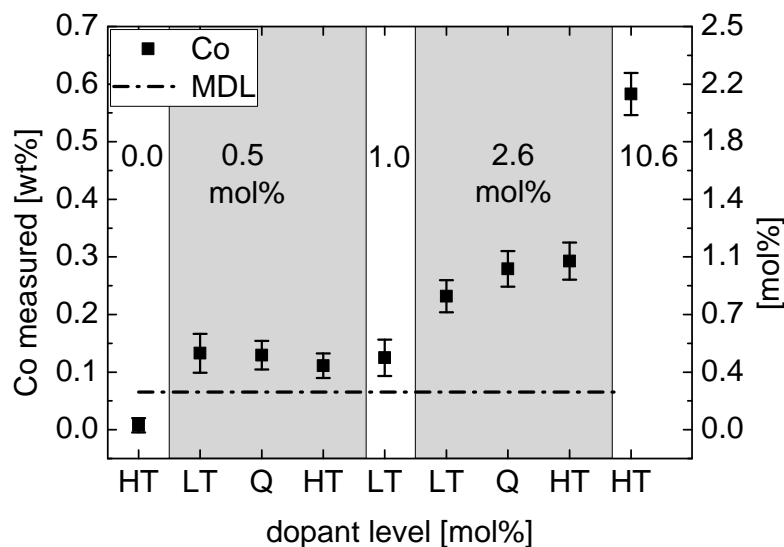


**Figure 5.6:** Quantitative electron microprobe analysis: Effect of sintering temperature and cooling conditions on the cobalt concentration in the BNT grains. MDL = mean detection limit, LT/HT = sintered at 1075 °C/1150 °C and slow cooling, Q = sintered at 1075 °C for 1 h and quenched.

## Transmission Electron Microscopy

The electron beam of the EPMA simultaneously probed a sample volume of approx.  $(2 \times 2 \times 1) \mu\text{m}^3$ . It was considered possible that the BNT grains contained nano-sized exsolutions of a cobaltous secondary phase that were too small to be recognized in the SEM images. They could thus also have generated a misleading cobalt signal. To verify this, high-resolution TEM (HR-TEM) images were recorded and checked for any distortions in the BNT lattice, which could originate from such precipitated cobalt phases due to lattice mismatch. Figure 5.7 shows a HR-TEM image of BNT with 2.6 mol % Co sintered at 1150 °C. No such distortions were observed in any of the tested grains ( $>5$ ) and at varying magnifications.

The same BNT sample was used to determine whether cobalt was distributed uniformly in the BNT grains, or whether it was accumulated at the grain boundaries or the middle of the grains. To this end, scans consisting of 20 or 40 spots arranged in lines (distance between spots 40 nm and 20 nm, respectively) crossing grain boundaries were conducted and analyzed. The results for the grain boundary scans shown in Figure 5.8 are presented in detail in the appendix section (Figures A.1, A.2 and A.3). Cobalt was detected in all of the examined BNT grains. Some elements were enriched at certain grain boundaries, but there was no consistent trend. Other grain boundaries showed no anomalies at all. These results indicate that cobalt is uniformly distributed in the BNT grains with no enrichment or depletion at the grain boundaries.

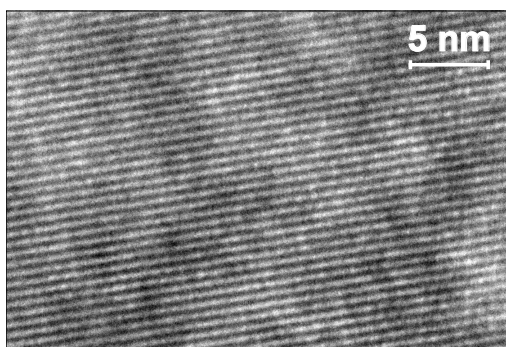


**Figure 5.7:** HR-TEM image of BNT doped with 2.6 mol % Co, sintered at 1150 °C.

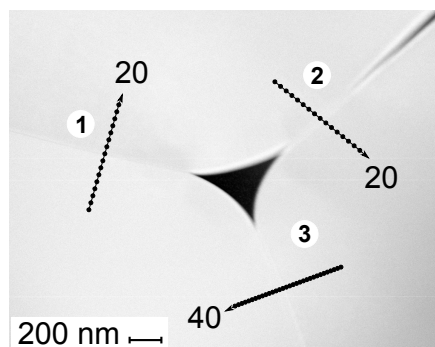


**Figure 5.8:** STEM image of BNT doped with 2.6 mol % Co. Scans across the grain boundary (1-3) consisting of 20 and 40 points are schematically shown by the black lines.

Since XRD did not yield clear results on the incorporation of Co into BNT via peak shifts, TEM was employed to determine whether Co was incorporated into BNT during the calcination, or rather at the elevated temperatures of the sintering process. This cannot be achieved using EPMA due to the comparably large diameter of the electron beam. For the analysis, calcined BNT was prepared in such a manner that the particles were cut to expose their core.

Figure 5.9 shows the STEM image of a BNT powder particle (2.6 mol % Co) after the calcination. The cobalt concentration was measured at the edge as well as in the middle of the grain. This procedure was repeated for several grains. Cobalt was detected in all examined grains, with no preference for neither the grain rims nor the core. Thus, cobalt was incorporated into the BNT lattice during the calcination.

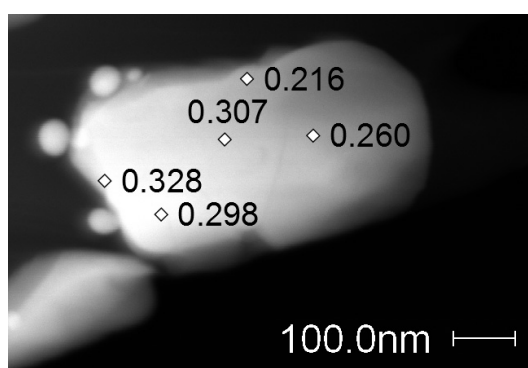


**Figure 5.9:** STEM image of BNT powder doped with 2.6 mol % Co after calcination (800 °C, 4 h). Numbers state mol % Co as determined by semi-quantitative EDX analysis at the indicated positions.

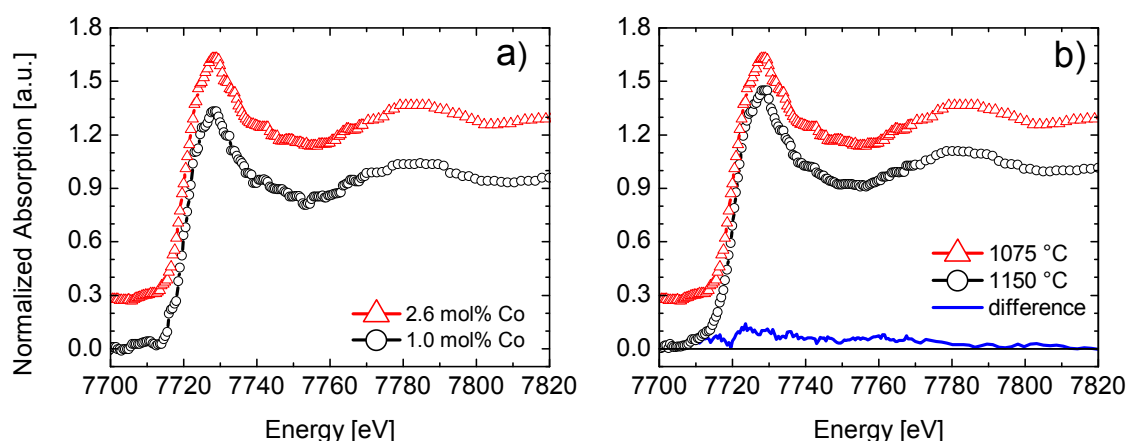
### 5.3 Lattice Site Preference

The lattice site preference of Co was determined by X-ray absorption fine structure (XAFS) experiments. XAFS is an element-selective technique, which can probe the local atomic environment of all Co atoms simultaneously. The measured absorption signal is a superposition of all Co signals in their respective environments. In the vicinity of the absorption edge, the measured XANES (X-ray absorption near-edge structure) spectra were compared to theoretical calculations based on model structures (FEFF9 software [Reh09]). For a detailed description, cf. Chapter 3.1.7.

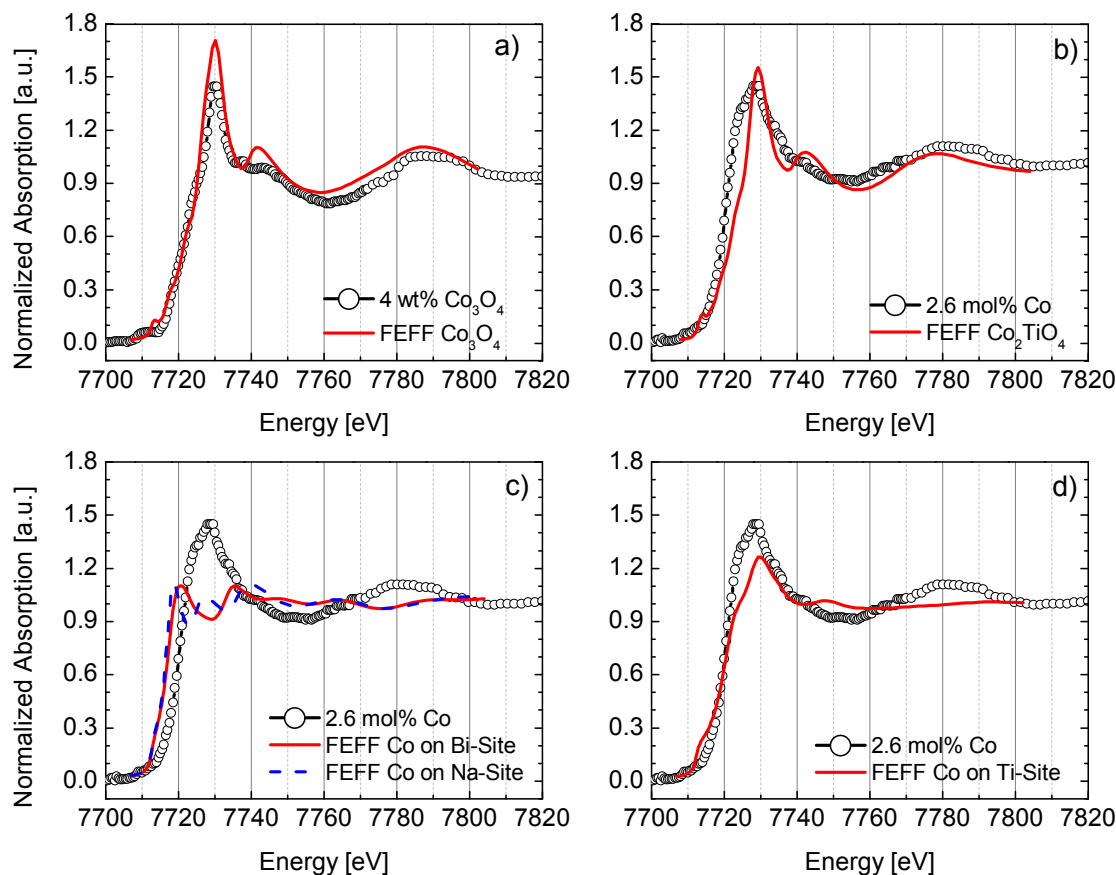
Figure 5.10a shows the Co K-edge of BNT doped with 1.0 mol % and 2.6 mol % Co. The signals from samples with lower Co concentrations were too weak to yield proper data. The absorption edge is shifted from 7709 eV (Co metal) to 7720 eV. This is typical for absorber atoms with a positive valence. The two spectra are identical within the resolution limits of the method, apart from a small pre-edge feature, which is probably an artifact since it did not occur repeatedly in the measurements.

Figure 5.10b provides a comparison of BNT doped with 2.6 mol % Co sintered at two different temperatures: 1075 °C and 1150 °C. No significant difference was observed. Hence, it is sufficient to consider one spectrum exemplary. In this case, BNT with 2.6 mol % sintered at 1075 °C was chosen, since it had the best signal to noise ratio (in the raw data).

To check the agreement of calculated and measured data, a known structure was compared to a theoretical calculation. Figure 5.11a shows the calculated spectrum of  $\text{Co}_3\text{O}_4$  plotted together with the Co signal of  $\text{Co}_3\text{O}_4$  powder in BNT. While the height of the maxima and minima is somewhat overestimated, the positions of all peaks are reproduced very well. A discussion of typical deviations between experimental and calculated spectra, such as the one in height, can be found in the work of Modrow et al. [Mod03].



**Figure 5.10:** XANES spectra of doped BNT at the Co K-edge: a) influence of dopant level (1075 °C); b) influence of sintering temperature (2.6 mol % Co)



**Figure 5.11:** Experimental XANES spectra of the Co K-edge: (a) Pure BNT powder, mixed with 4 wt %  $\text{Co}_3\text{O}_4$  compared to the calculated XANES signal of  $\text{Co}_3\text{O}_4$ ; (b-d) BNT doped with 2.6 mol % Co, 1075 °C, compared to calculated XANES spectra of (b)  $\text{Co}_2\text{TiO}_4$ , (c) Co on the Bi-site (solid line) and Na-site (dashed line) of BNT, (d) Co on the Ti-site of BNT.

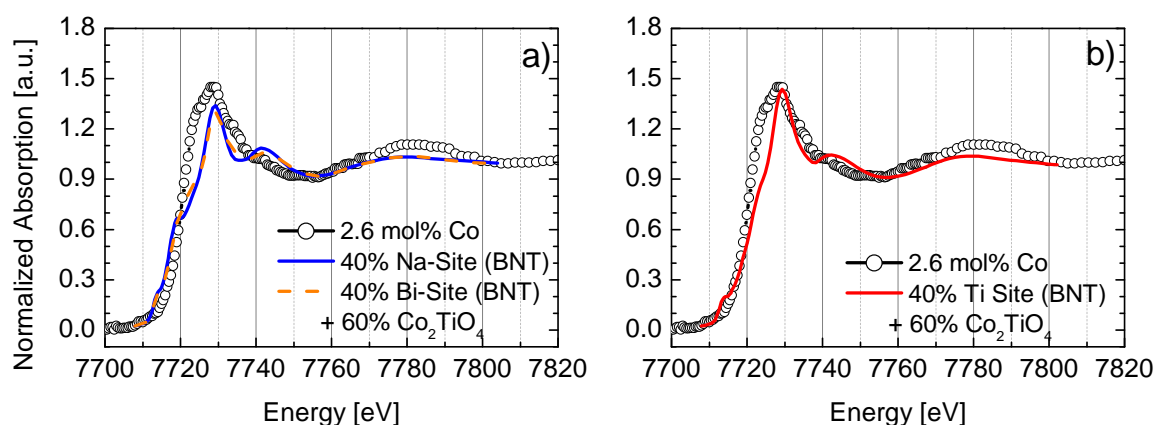
As is known from the EPMA results, approx. 40 % of the total added Co was incorporated into the BNT lattice, while the remaining Co formed the secondary phase  $\text{Co}_2\text{TiO}_4$ . Hence, a XANES spectrum of cobalt-doped BNT is a superposition of Co atoms in BNT and Co atoms in  $\text{Co}_2\text{TiO}_4$ .

Figure 5.11b shows the experimental XANES spectrum of BNT with 2.6 mol % Co (1075 °C) together with the calculated spectrum of the secondary phase  $\text{Co}_2\text{TiO}_4$ . Due to the high amount of secondary phase, there is already a clear resemblance.

Figure 5.11c and 5.11d compare the experimental spectrum to calculated spectra of BNT structures, in which Co replaces the A-cation (either  $\text{Bi}^{3+}$  or  $\text{Na}^{+}$ ) and the B-cation ( $\text{Ti}^{4+}$ ), respectively. The former spectra have their maxima at different energies than the experimental data, and the overall match is poor. In contrast, when Co is incorporated at

the B-site, some features of the experimental spectrum are reproduced fairly well, especially the white line (first, strong peak above the edge energy).

A superposition of the calculated spectra of  $\text{Co}_2\text{TiO}_4$  and Co on the two cation sites of BNT is compared to the measured data in Figure 5.12. For the B-site calculation, a very good agreement with the experimental data is reached, whereas the A-site spectrum poorly reproduces the experimentally observed features, especially near the absorption edge energy. Thus, it is reasonable to assume that Co can replace Ti in BNT to a certain degree.



**Figure 5.12:** Superposition of calculated XANES spectra: 40 % Co a) on the A-site (replacing Na or Bi), b) on the Ti-site in BNT and 60 %  $\text{Co}_2\text{TiO}_4$  versus measured BNT with 2.6 mol % Co. Ratio of cobalt in the secondary phase and BNT is according to EPMA analysis.

## 5.4 Discussion

### 5.4.1 Secondary Phases

When BNT was doped with more than 0.1 mol % Co, one (1000 °C) or two (1075 °C and 1150 °C) secondary phases formed. They could reliably be detected using backscattering SEM, whereas the standard method, powder XRD, was not sensitive enough. In the literature, BNT-BT doped with up to 2.3 mol % Co was reported to be single phase [Chu02, Li04, Xu08a, Zha07], based on XRD measurements. The details on the measurement parameters were not given. Considering the results presented above, BNT and BNT-BT doped with Co or other elements might also have erroneously been believed to be free of secondary phases. The example of Fe-doped BNT further supports this supposition: by chance, a secondary phase was revealed during synchrotron diffraction experiments [Aks12] (2 mol % Fe).

$\text{Co}_2\text{TiO}_4$  was identified in all but one of the secondary phase bearing samples. Quenching experiments showed that it had formed at the sintering temperature rather than being the result of a precipitation process during cooling. This implies that  $\text{Co}_2\text{TiO}_4$  is thermodynamically stable at the sintering temperatures.

The other secondary phase, which was observed in very small quantities, varied slightly in composition. This may be attributed to small grains which make an accurate determination of the composition via SEM-EDX difficult. The composition can be approximated by the formula  $\text{Na}_x\text{Co}_{x/2}\text{Ti}_{2-x/2}\text{O}_4$  (and for 10.6 mol % by  $\text{Na}_x\text{Co}_{x/2}\text{Ti}_{1-x/2}\text{O}_2$ ), corresponding to sodium cobalt titanates reported by Shukaev and Volochaev [Shu95] in their study of the system  $\text{Na}_2\text{O-TiO}_2\text{-CoO}$  at 1000 °C. They observed that some of the compositions melted fully or partially when heated to 1000 °C–1050 °C. This could explain the melt-like morphology, especially since the sodium cobalt titanate grains in BNT with 0.5 mol % Co sintered at 1000 °C, though probably slightly different in composition, still possessed a hypidiomorphic shape.

### 5.4.2 Local Atomic Environment

Thorough investigations using EPMA and HR-TEM demonstrated that a fraction of the added Co had been incorporated into the BNT lattice. BNT doped with 2.6 mol % Co, for instance, can incorporate  $(1.0 \pm 0.1)$  mol % Co. The results of STEM-EDX showed that the incorporation reaction started during the calcination at 800 °C. This detection method was only semi-quantitative. Hence, the concentration in the calcined and sintered samples cannot be compared quantitatively, opening up the possibility that the incorporation reaction may be incomplete at this processing step.

The preferred cation lattice site of Co was identified via XANES. Theoretical calculations of model structures with Co replacing Ti in BNT were in good agreement with the measured data. This also makes sense from a crystal chemical point of view, since the ionic radius of cobalt is much closer to that of  $\text{Ti}^{4+}$  than to either  $\text{Bi}^{3+}$  or  $\text{Na}^+$  (cf. Table 5.2). Recently, Aksel et al. obtained a similar result for iron-doped BNT. Using electron paramagnetic resonance, they demonstrated that  $\text{Fe}^{3+}$  is incorporated into BNT on the Ti site [Aks10a]. With the same technique it was shown that  $\text{Cu}^{2+}$  can be incorporated at the B-site of BNT-BT-KNN [Jo11].

The ionic radii of both  $\text{Co}^{2+}$  and  $\text{Co}^{3+}$  deviate slightly from that of  $\text{Ti}^{4+}$ . When cations of different size replace atoms in a crystal lattice, dimensional changes in the lattice parameters due to radius mismatch can occur. As a consequence, the  $2\theta$  angles change (cf. eq 3.1), leading to a shift of the peaks in XRD patterns. Such ‘peak shifts’ were reported by Xu et al. [Xu08b] for cobalt-doped BNT-BT, whereas—for similar Co concentrations—they were not observed in this study.

However, only up to  $(1.0 \pm 0.1)$  mol % Co was actually incorporated into the perovskite (BNT + 2.6 mol % Co). This is a fairly small amount, which does not necessarily result in detectable X-ray peak shifts. Again, the result is in agreement with Fe-doped BNT, where the iron incorporation at the B-site had almost no effect on the lattice parameters [Aks12]. The shifts observed in the mentioned BNT-BT study by Xu and his team might be ex-

plained by the particle size of their samples, which were in the sub-micrometer region, but increased strongly with increasing dopant concentrations. In PZT the crystal symmetry (tetragonal or rhombohedral at the MPB) was shown to depend on the particle size [Hel07].

### 5.4.3 Valence State

Under most circumstances, XANES also allows for the determination of cation valences. The higher the oxidation number, the further the absorption energy is shifted toward higher energies as compared to the neutral metallic state. Thus, it should be possible to distinguish between  $\text{Co}^{2+}$  and  $\text{Co}^{3+}$ . If Co is incorporated as  $\text{Co}^{2+}$ , all Co atoms in the ceramic have a valence of +2. If Co in BNT has a valence of +3, the overall oxidation number is +2.4. Hence, a comparison of the edge energies of cobalt-doped BNT spectra with standard spectra of pure  $\text{Co}_3\text{O}_4$  (mean valence of +2.66) and pure  $\text{Co}_2\text{TiO}_4$  (mean valence of +2.0) could have revealed the Co valence in BNT. However, the available  $\text{Co}_3\text{O}_4$  powders commonly contain approx. 10 wt % CoO as impurity phase. Moreover, pure  $\text{Co}_2\text{TiO}_4$  is not available on the market, and is difficult to synthesize in a quality sufficient for a XANES standard.

Crystal chemical considerations might yet give a clue to the Co valence state. The stability of a perovskite can be estimated with the help of the Goldschmidt tolerance factor  $t$  [Gol26]:

$$t = \frac{R_A + R_O}{\sqrt{2}(R_B + R_O)} \quad (5.1)$$

Here,  $R_A$ ,  $R_B$  and  $R_O$  are the ionic radii of the A-site and B-site cation and the oxygen anion, respectively. For a perfect cubic perovskite,  $t$  is equal to unity. Perovskites with  $0.9 < t < 1.1$  usually are stable, whereas larger deviations result in the crystallization of other structure types. The tolerance factors for Co in both valences is given in Table 5.2. The tolerance factor for  $\text{Co}^{3+}$  is closer to unity than that for  $\text{Co}^{2+}$ , but both structures probably would be stable. As mentioned before, the structure with  $\text{Fe}^{3+}$  ( $t = 0.91$ ) is stable, even though the ionic radius of  $\text{Fe}^{3+}$  is rather big. Thus, none of the two cobalt valences can be excluded. Results from sintering experiments, however, indicate that Co

**Table 5.2:** Ionic radii in Å according to Shannon [Sha76]. The coordination number (CN) is given in square brackets. The corresponding Goldschmidt tolerance  $t$  factors for different B-site cations are also given.

Cation [CN]	$\text{Ti}^{4+}$ [6]	$\text{Co}^{2+}$ [6]	$\text{Co}^{3+}$ [6]	$\text{Fe}^{3+}$ [6]	$\text{Na}^+$ [12]	$\text{Bi}^{3+}$ [8]
Ionic radius	0.61	0.65	0.55	0.69	1.39	1.17
Tolerance factor $t$	0.94	0.92	0.97	0.91	-	-

is incorporated as trivalent cation during the calcination, but changes to the divalent state above 950 °C (cf. Chapter 6.5.2).

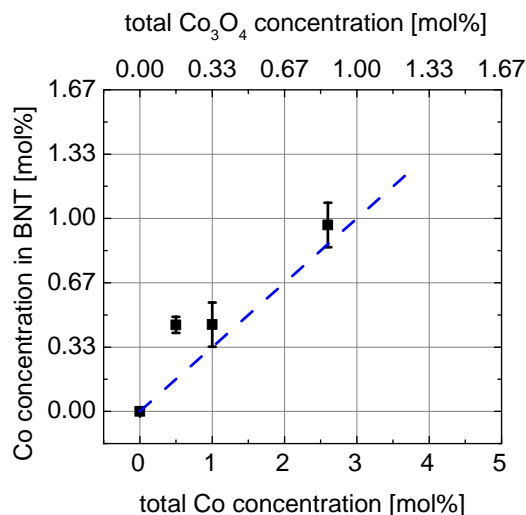
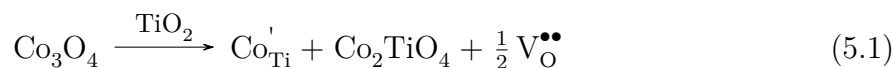


**Figure 5.13:** Measured cobalt concentration in BNT lattice versus total cobalt concentration in the samples as determined by EPMA. The dashed line with a slope of 1/3 represents the cobalt incorporation according to eq 5.1.

#### 5.4.4 Quantitative Considerations

The amount of incorporated Co was determined by EPMA experiments. BNT doped with 10.6 mol % Co displayed a cobalt concentration as high as 2.1 mol % (corresponding to 0.58 wt %), suggesting that the actual solubility limit lies even higher. However, an increased incorporation of Co seems to be coupled with an increased amount of secondary phase, suggesting an equilibrium between Co in the main and secondary phases.

A quantitative relation between added and actually incorporated Co is shown in Figure 5.13. The following incorporation reaction is suggested (dashed blue line):



Here,  $\text{Co}'_{\text{Ti}}$  represents a cobalt atom on the Ti site with a negative effective charge, and  $\text{V}_{\text{O}}^{\bullet\bullet}$  denotes a vacant oxygen site with two positive effective charges.

When BNT is doped with  $\text{Co}_3\text{O}_4$ , one cobalt atom (here assumed to be  $\text{Co}^{3+}$ ) per  $\text{Co}_3\text{O}_4$  molecule substitutes for  $\text{Ti}^{4+}$ . The remaining Co forms  $\text{Co}_2\text{TiO}_4$  together with the freed Ti atom. Thus, 1/3 of the cobalt amount is incorporated into the lattice, which is represented by the blue dashed line in Figure 5.13. The experimental data fits well to this theory. There is only a deviation at a Co concentration of 0.5 mol %, indicating that very



small  $\text{Co}_2\text{TiO}_4$  crystals may not be stable, which promotes higher cobalt concentrations in the BNT lattice.

The aliovalent substitution of Ti is accompanied by an excess negative charge, which is compensated for by the generation of one oxygen vacancy  $V_{\text{O}}^{\bullet\bullet}$  per two substitutional Co atoms. Oxygen vacancies enhance the mass transport during sintering of oxide materials. In perovskites, the cations have lower diffusion coefficients than oxygen. However, since the diffusion of anions and cations is coupled (cf. Chapter 6.5.1), the overall diffusivity also benefits from vacancies which primarily increase the oxygen diffusivity. Oxygen vacancies also affect the domain stability of ferroelectrics and generally result in a hardening effect. These topics will be discussed in the following chapters.



## 6 Sintering of Cobalt-Doped BNT

Knowledge of the processes taking place during heat treatment and sintering is essential for the control of the final ceramic's properties. Apart from the mass transport which leads to densification, solid state reactions, diffusion processes not contributing to densification, valence transitions and vaporization of atomic species need to be taken into account. The following chapter compares the sintering behavior of cobalt-doped and pure BNT following the three basic sintering stages (cf. Chapter 2.3.1) and investigates effects which occur during the heat treatment.

### 6.1 Initial Sintering Stage

The sintering behavior of BNT was investigated by thermo-optical dilatometry in TOM (cf. Chapter 3.1.9). Figure 6.1 shows the sintering curves of BNT with dopant levels from 0.0 mol % to 2.6 mol % Co. Pure BNT began to shrink at 856 °C and required temperatures of 1150 °C to sinter to full density. Adding 0.1 mol % barely affected the sintering behavior. Higher doping levels, however, lead to a drastic decrease in sintering temperatures. This is illustrated in Figure 6.2. Here, the onset temperature of sintering,  $T_{\text{onset}}$ , taken at 1 % shrinkage, and the temperature of half shrinkage  $T_{50}$  are plotted against the dopant level. Both  $T_{\text{onset}}$  and  $T_{50}$  decreased with increasing dopant amount to similar degrees. The most pronounced decrease was obtained for 0.5 mol % Co, while higher dopant levels had a comparably smaller effect. Overall, the sintering temperature could be reduced by more than 100 K by the addition of 2.6 mol % Co.

### 6.2 Intermediate Sintering Stage

#### Sintering with Uniaxial Load

To clarify whether the improved sinterability of Cobalt-doped BNT was due to liquid-phase assisted sintering, sintering experiments with uniaxial load were carried out. The method exploits the fact that a liquid film reduces the friction between particles and facilitates their rearrangement. Hence, when a small load is applied to the green body during sintering, preferential shrinkage in the direction of the external pressure will occur, whereas the shrinkage will be reduced in the perpendicular directions.

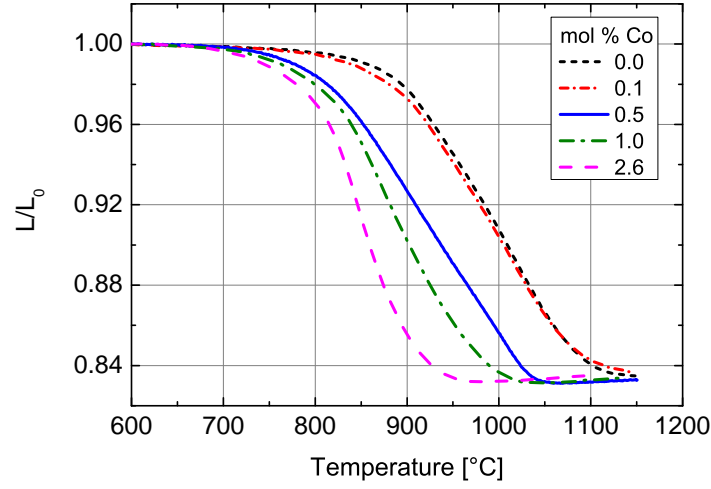


**Figure 6.1:** Sinter shrinkage of BNT doped with various amounts of Co; the heating rate was  $5 \text{ K min}^{-1}$ .

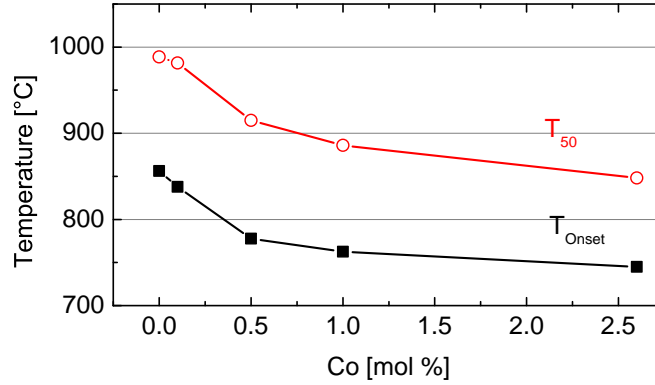


**Figure 6.2:** Onset temperature  $T_{\text{Onset}}$  and temperature of half sinter shrinkage  $T_{50}$  for BNT doped with various amounts of Co; data extracted from the shrinkage curves shown in Figure 6.1.

The load must be chosen small enough not to alter the sintering mechanism, that is, several orders of magnitude below the sintering stress  $\sigma$  for solid state sintering. The sintering stress can be estimated using the Young-Laplace-equation [Ger96] and depends on the surface energy and the reciprocal pore radius of the material.

In the final sintering stage,  $\sigma$  lies around 1 MPa for this study's BNT (for derivation, cf. Chapter 6.5.2). The chosen load of 110 g corresponds to a pressure of ca. 8.5 kPa, which is safely below the sintering stress. Figure 6.3a shows the shrinkage curves of pure BNT. Both the width and the height shrunk almost identically for sintering with and without load. In contrast, the shrinkage curves of BNT doped with 2.6 mol % Co shown in Figure 6.3b

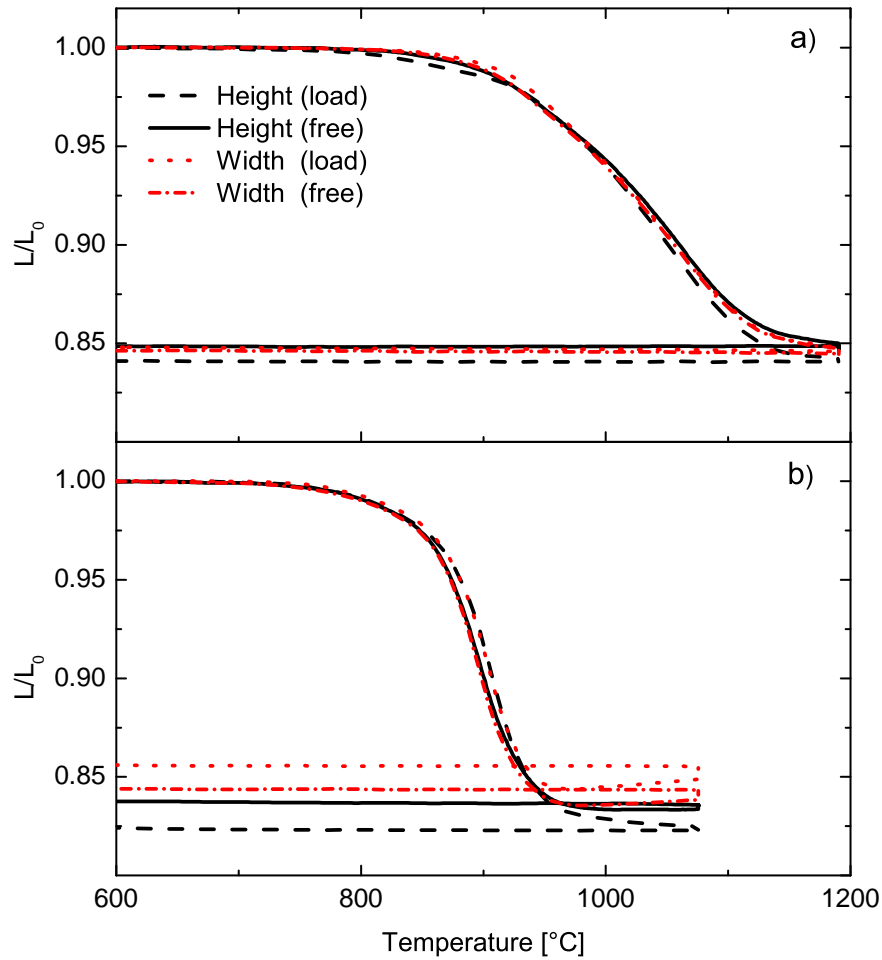


**Figure 6.3:** Sintering with uniaxial load of a) pure BNT and b) BNT doped with 2.6 mol % Co in the TOM furnace. Two samples of the same batch were sintered with and without a small vertical load of 8.5 kPa (ca. 110 g).

display a reduced sample height and increased sample width after sintering with load. Though the effect is comparably small, it can nevertheless be attributed to liquid-phase sintering. The deviation between horizontal and vertical shrinkage set in at 950 °C, that is, in the last sintering stage. BNT with lower cobalt concentrations showed a correspondingly smaller degree of liquid-phase sintering, but with similar onset temperatures.

## Melting Experiments

The magnitude of the observed creep effect was fairly limited compared to other liquid-phase sintering systems (cf. e.g. [Hua08]). Thus the amount of liquid phase was considered to be rather small and consequently hard to detect. Neither SEM nor STEM-EDX showed

the presence of a melt film or an enrichment of specific elements at grain boundaries in the sintered samples (cf. Chapter 5.2). Hence, an indirect approach to determine the nature of the liquid phase was pursued.

Selected powder mixtures were tested in TOM with regard to their melting temperature. To this end, cylindrical samples of compacted powder mixtures were placed on a sintered, polished BNT substrate and heated with  $5\text{ K min}^{-1}$ . Figure 6.4 shows the corresponding setup observed by the TOM furnace camera (cf. Chapter 3.1.9). The powder mixtures were composed of the same oxide powders as those used for the BNT synthesis.

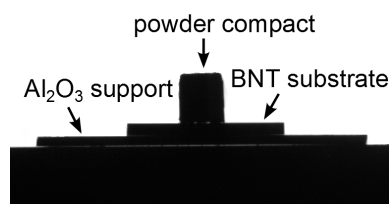


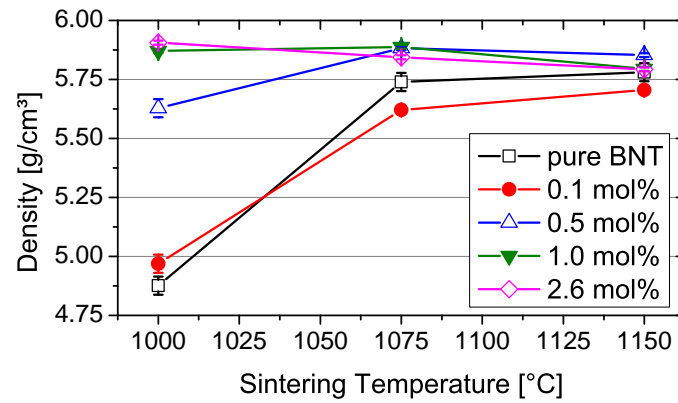
**Figure 6.4:** Setup for melting experiments observed by the TOM camera: a compacted powder cylinder is placed on a polished BNT disc on an alumina support.

The first powder mixture tested corresponded to the average stoichiometry of the sodium cobalt titanate phase,  $\text{Na}_{0.8}\text{Co}_{0.3}\text{Ti}_{1.7}\text{O}_4$ , as determined by SEM-EDX (cf. Chapter 5.1). To account for a possible melting point depression, the composition was tested with and without additional  $\text{Bi}_2\text{O}_3$  (4 vol %). The second composition was  $\text{NaBiO}_2$ , which could develop in the BNT samples if  $\text{Co}_2\text{TiO}_4$  formed with only minor replacement of Ti by Co in BNT. Ti-deficient BNT, however, is unstable and tends to decompose into secondary phases [Spr07].  $\text{TiO}_2$  and  $\text{CoO}$  were added to  $\text{NaBiO}_2$  in small quantities.

$\text{Na}_{0.8}\text{Co}_{0.3}\text{Ti}_{1.7}\text{O}_4$  with and without  $\text{Bi}_2\text{O}_3$  did not show signs of melting up to  $1150^\circ\text{C}$ . The powder compact began to shrink at ca.  $1100^\circ\text{C}$  and slightly stuck to the BNT substrate after the heat treatment. An XRD analysis confirmed the formation of a sodium cobalt titanate reported by Shukaev and Volochaev [Shu95] ( $\text{Na}_{0.8}\text{Co}_{0.4}\text{Ti}_{3.6}\text{O}_8$ ).  $\text{NaBiO}_2$ , on the other hand, melted completely at  $670^\circ\text{C}$ . The liquid wetted the entire BNT surface, with some  $\text{Bi}_2\text{O}_3$  infiltrating the BNT substrate.

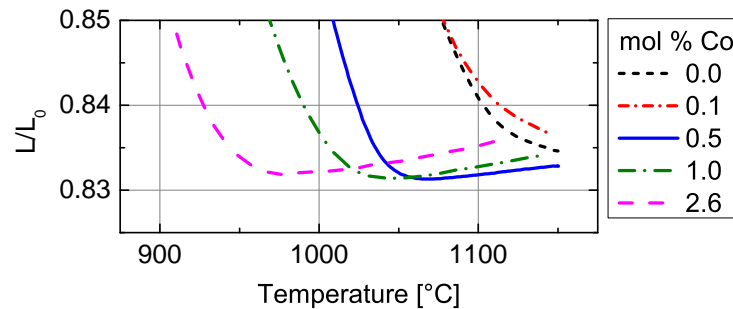
### 6.3 Final Sintering Stage

Figure 6.5 compares the final densities of pure and doped BNT as a function of temperature. As expected from the literature, pure BNT required more than  $1100^\circ\text{C}$  to sinter densely. Doping with 0.1 mol % Co resulted in a similar behavior, that is, the density strongly increased with increasing temperature. Doping with 0.5 mol % Co lead to comparably well densified material at  $1000^\circ\text{C}$ . At  $1075^\circ\text{C}$  and  $1150^\circ\text{C}$  the densities reached values above those of pure and weakly doped BNT. When 1.0 mol % or 2.6 mol % Co was added, the highest densities were obtained at the lowest sintering temperature of  $1000^\circ\text{C}$ . Contrary



**Figure 6.5:** Final densities of pure and doped BNT ceramics after sintering at the indicated temperature for 2 h.

to the other compositions, increased sintering temperatures led to reduced final densities for both compositions. These results are reflected in the sintering curves of doped BNT. Figure 6.6 magnifies the final sintering stage of the curves shown in Figure 6.1. After the minimum of the shrinkage curves is passed, samples doped with 0.5 mol % Co or more begin to swell. The higher the doping level, the stronger the swelling. This effect is real and not due to thermal expansion, which was corrected for as described in Chapter 4.2.1. The swelling is more likely caused by gas trapped in closed pores of the samples, which would explain the observed decrease in final densities mentioned above.



**Figure 6.6:** Sintering curve of doped BNT during the final sintering stage showing sample expansion (magnification of Figure 6.1); the expansion is attributed to the release of oxygen caused by the reduction of  $\text{Co}^{3+}$  to  $\text{Co}^{2+}$ . The gas is trapped in the closed pores and exerts a pressure which counteracts the sintering stress.

## 6.4 Kinetic Field

The kinetic field can be constructed based on the liquid-phase sintering model (cf. [Rae09b]). However, it is sufficient in this case to use the simpler solid state sintering model, since the liquid formation in cobalt-doped BNT concerns only the late final sintering stage at temperatures above 950 °C, where the shrinkage of highly doped BNT is almost complete. Optical dilatometry was used to obtain the shrinkage curves for pure and 2.6 mol %-doped BNT. The heating rates were varied from 0.5 K min<sup>-1</sup> to 10 K min<sup>-1</sup> to obtain several different values for the density  $\rho$  at each temperature. The shrinkage curves are shown in Figure 6.7. For both compositions, the onset temperature and the temperature of maximum shrinkage increased with increasing heating rates. This behavior is common and attributed to the fact that at lower heating rates, the compact is exposed longer to the respective temperatures and thus shrinks more strongly than faster heated samples [Sat96].

From the shrinkage curves in Figure 6.7 kinetic field diagrams were constructed by plotting the logarithm of the strain versus the inverse absolute temperature, as described in Chapter 4.2.2. Iso-strain lines were fitted to the points of equal shrinkage on all curves.

Figure 6.8a and 6.8b show the kinetic field diagrams for pure BNT and BNT doped with 2.6 mol % Co. For selected iso-strain lines the engineering strain  $\Delta L/L_0$  is indicated. The iso-strain lines fitted to the shrinkage curves of pure BNT display an almost constant slope. The horizontal shift is caused by grain growth [Rae09c]. In contrast, the iso-strain lines of BNT doped with 2.6 mol % Co begin to rotate anticlockwise at higher sintering temperatures, so that their slope decreases.

The apparent activation energies  $E_a$  are plotted in Figure 6.9. During the first half of the sintering process,  $E_a$  is comparable for both compositions and varies only in a narrow

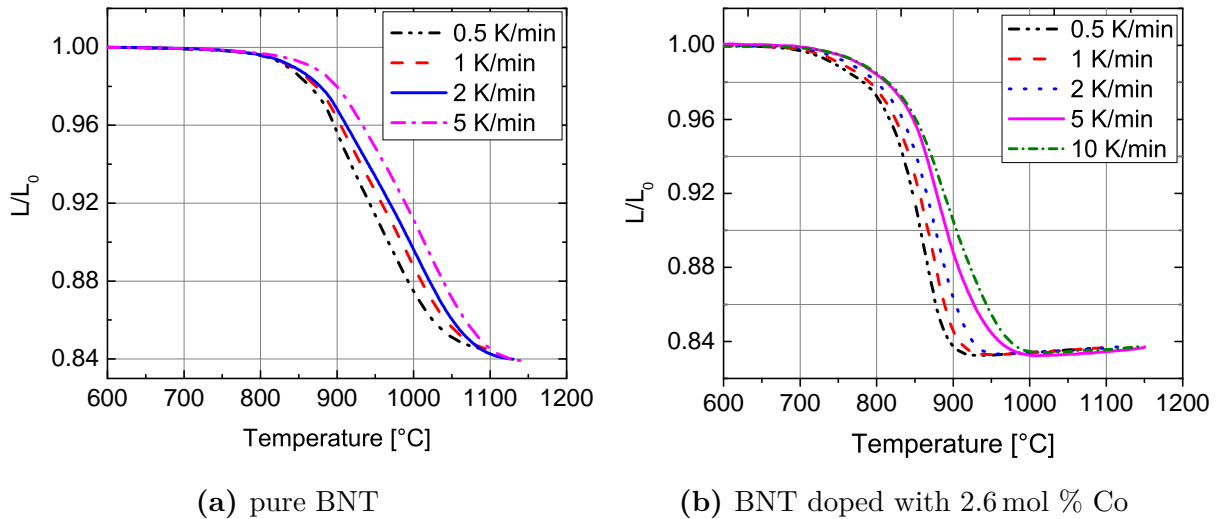


**Figure 6.7:** Shrinkage curves of a) pure BNT and b) BNT doped with 2.6 mol % Co at different constant heating rates.



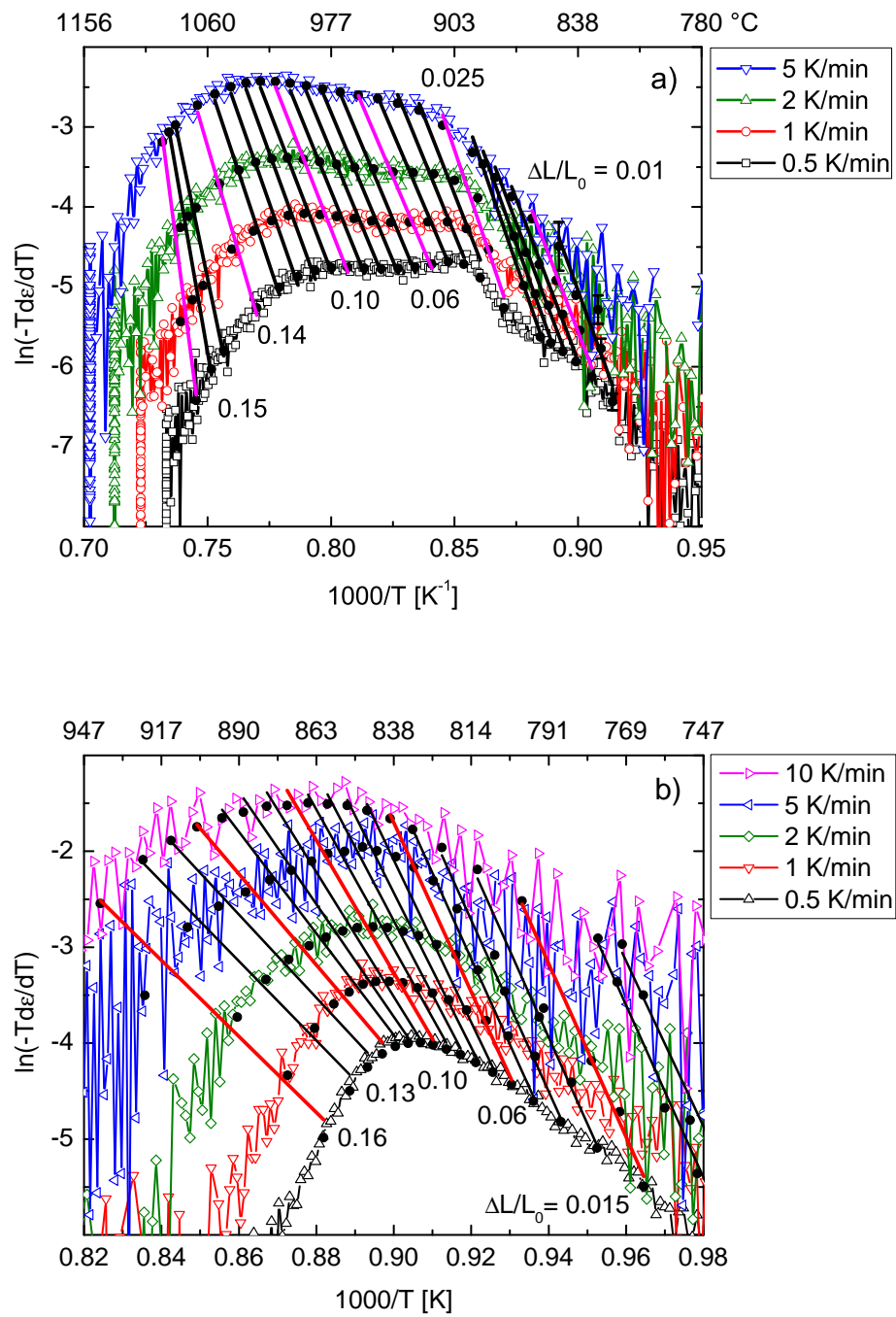


**Figure 6.8:** Kinetic field of a) pure BNT and b) BNT doped with 2.6 mol % cobalt. The diagram was constructed using the shrinkage curves shown in Figure 6.7.  $\Delta L/L_0$  is the engineering strain derived from the sintering curves.

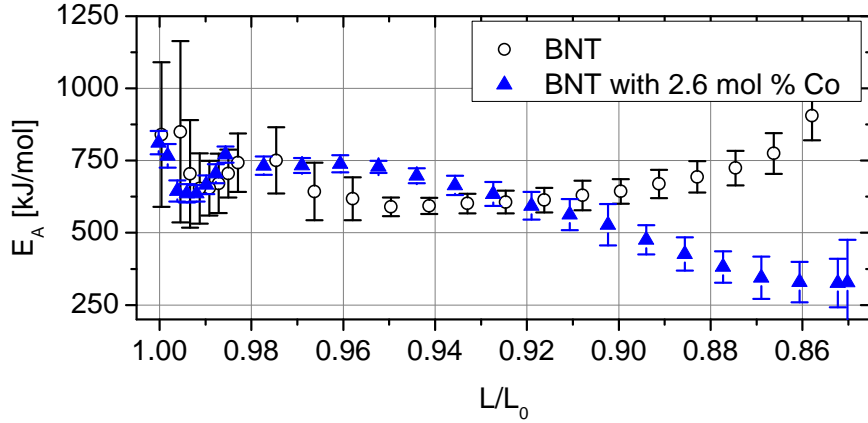


**Figure 6.9:** Comparison of the apparent activation energies  $E_a$  for pure BNT and BNT doped with 2.6 mol % Co. The values were derived from the slopes of the iso-strain lines in the corresponding kinetic field diagrams (Figures 6.8a and 6.8b).

range. In the second half, the apparent activation energy increases in the pure material, whereas an opposite trend manifests for doped BNT.

## 6.5 Discussion

The effect of cobalt doping on the sintering behavior of BNT was investigated in comparison to pure BNT. As shown in Figures 6.1 and 6.2, the addition of cobalt decreased the sintering temperature and led to rapid densification. Doped BNT could be sintered to high final densities at temperatures as low as 1000 °C, which is 150 K below the sintering temperature of pure BNT. The densification was mainly achieved by solid state sintering mechanisms. A small amount of liquid phase was generated above 950 °C. Samples with high dopant concentrations displayed swelling when sintered at high temperatures.

### 6.5.1 Densification Behavior

In solid state sintering, the main mechanisms leading to densification are grain boundary diffusion and lattice diffusion, which transfer material from the grain boundaries to the pores (cf. Chapter 2.3). Lattice diffusion takes place via point defects which move through the lattice. When Schottky type defects, that is, vacant atomic sites in a lattice are present, atoms can move by exchanging their place with the vacancy. The atomic diffusion coefficient  $D$  for this mechanism is directly proportional to the fraction of sites occupied by vacancies. The densification rate during sintering, in turn, directly depends on  $D$  (cf. eq 4.1).

In ceramics, the diffusion of the electrically charged cations and anions is coupled (*‘ambipolar diffusion’*) [Rah03], because the stoichiometry and electroneutrality of the solid must

be maintained. The slowest diffusing species along its fastest diffusion path limits the rate of matter transport. In perovskites the diffusion coefficient of the cations is several orders of magnitude lower than that of oxygen. It is possible that the diffusion, especially that of the B-site cations, is facilitated by cobalt-doping, since  $\text{Co}^{3+}$  has a smaller ionic radius than  $\text{Ti}^{4+}$  (0.55 Å compared with 0.61 Å). Due to the coupled diffusion, however, enhanced diffusivity of the faster species also serves to accelerate the diffusion of the slower species [Rah03]. Hence, the effective diffusion coefficient of BNT benefits from the induced oxygen vacancies (cf. Chapter 5.4) which enhance oxygen diffusivity [Chr10]. Similar effects of aliovalent dopants on the sintering behavior of lead-free piezoceramics were reported and attributed to oxygen vacancies, e.g. for iron-doped BNT [Wat07] or copper-doped KNN [Wan12], which is a perovskite of similar structure as BNT.

While the introduction of 0.1 mol % Co appears to create a too small number of oxygen vacancies to improve sintering, the fivefold amount (0.5 mol % Co) significantly enhanced the densification. The comparably smaller effect of higher cobalt concentrations (1.0 mol % and 2.6 mol %) could be due to clustering of oxygen ion vacancies, thus reducing the efficiency of matter transport.

The enhanced diffusivity allows to sinter doped BNT to higher densities, since it facilitates pore removal by diffusion. This explains the high densities reached for BNT doped with 0.5 mol % Co or higher.

## 6.5.2 Swelling of Doped BNT

The final density of highly doped BNT decreased with increasing sintering temperature. This was reflected in the sintering behavior. After a minimum in the shrinkage curves was passed, the bodies began to swell. This effect is generally observed when gas, which is slightly soluble or insoluble in the solid, becomes trapped in pores. In that case, the shrinkage stops when the gas pressure in the pores equals the driving force for sintering. Now, the sintering process is controlled by the diffusional gas exchange between the pores. A net flow of gas molecules from small pores to neighboring larger pores which have a lower pressure sets in. The volume of the enlarged pores is greater than the sum of the two original pore volumes, leading to an effective swelling of the ceramic body [Rah03].

In this study only the doped samples showed such a swelling effect, despite the high diffusivity. It thus cannot be attributed to enclosed sintering atmosphere (in this study: air), but rather suggests that cobalt-doping causes swelling by increasing the evaporation of some species. In addition, since cobalt reduces the sintering temperature, it reduces the temperature at which the pores close. As a consequence, gas which would otherwise have evaporated and escaped through the open pore system can get trapped inside the ceramic body. Diffusion is considered too slow to counteract the enfolding bloating effect within the timescale of the sintering process.

The required gas pressure for swelling would have to be big enough to counteract the sintering stress  $\sigma$ , which can roughly be estimated using the Young-Laplace-equation [Ger96]:

$$\sigma = \gamma_{sv} \left( \frac{2}{r} \right) \quad (6.1)$$

where  $\gamma_{sv}$  is the solid-vapor interface energy, and  $r$  the radius of a spherical pore.  $\gamma_{sv}$  typically ranges from  $1 \text{ J m}^{-2}$  to  $2 \text{ J m}^{-2}$  for oxides [Ger96, Rah03]. Assuming a pore diameter of  $1 \mu\text{m}$ , the sintering stress  $\sigma$  lies around 2 MPa for the studied material.

Bismuth is known to be the most volatile species in BNT [Nag06, Hir09]. The partial pressure created by bismuth and bismuth oxide ions over solid BNT was calculated under isochoric conditions at  $1000^\circ\text{C}$  using the program FACTSAGE [Bal02]. It turned out to be several orders of magnitude lower than the sintering stress. This is in accordance with the literature, where significant Bi evaporation was reported to commence above  $1100^\circ\text{C}$ . Hence, even if cobalt-doping were to increase the evaporation of Bi, it is unlikely to cause the observed swelling.

Another possible source of a gaseous species is related to a valence transition of  $\text{Ti}^{4+}$  to  $\text{Ti}^{3+}$ . This was observed in  $\text{BNT-Bi}_{0.5}\text{K}_{0.5}\text{TiO}_3$  sintered in air and attributed to a charge balancing effect during Bi vacancy formation [Che10]. The reduction leads to the evaporation of oxygen, but is rather weak and thus would have to be strongly enhanced by Co-doping to induce swelling.

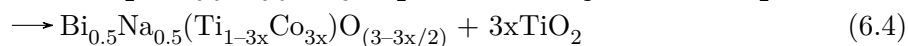
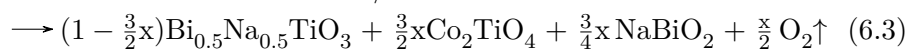
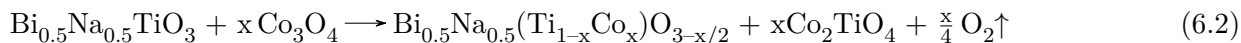
Depending on the sintering atmosphere, valence changes of other transition elements, e.g. Fe, Cr, or Co can occur. These generally result in the vaporization of certain atomic species or molecules. For cobalt, common oxidation numbers include +2 and +3. The reduction from  $\text{Co}^{II}\text{Co}^{III}_2\text{O}_4$  to  $\text{Co}^{II}\text{O}$  occurs at  $900^\circ\text{C}$  [Che03] in air. If residual  $\text{Co}_3\text{O}_4$  was present during the sintering process, it would have reacted to  $\text{Co}_2\text{TiO}_4$  and be partially incorporated into BNT. Hence, a fraction of the initially trivalent cobalt would have to undergo a valence transition (even if Co was incorporated as  $\text{Co}^{3+}$ ). As a consequence  $\text{O}^{2-}$  would be released, which would get trapped in pores that closed early in the sintering process due to inhomogeneous densification.

Furthermore, the incorporated Co in BNT itself could undergo the same transition from  $\text{Co}^{3+}$  to  $\text{Co}^{2+}$ . Such a valence change would be driven by the increase of entropy, which becomes the dominating contribution to the free enthalpy at high temperatures. Additional oxygen vacancies would be created in the BNT lattice by vaporization of oxygen to balance charges. This mechanism directly scales with the dopant concentration. The effect is further enhanced by the fact that the highly doped material sinters earlier and thus possesses closed pores at lower temperatures than weakly doped or pure BNT. Hence, the valence change of cobalt is considered the most likely cause for the observed swelling.

### 6.5.3 Liquid Phase Sintering

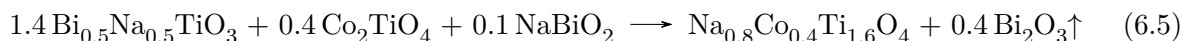
Doped BNT samples showed liquid-phase sintering behavior above  $950^\circ\text{C}$ . The magnitude of this effect was proportional to the dopant concentration, whereas the onset temperature remained constant. In melting experiments, the sodium cobalt titanate powder mixture appeared to remain solid up to  $1150^\circ\text{C}$ . In contrast,  $\text{NaBiO}_2$  melted at  $670^\circ\text{C}$ , that is, almost 300 K below the observed effect. Hence, a more detailed investigation of the phase formation in cobalt-doped BNT is required.

In general, several reactions of BNT with  $\text{Co}_3\text{O}_4$  are conceivable:



The last reaction (eq 6.4) can be discounted, since none of the applied phase analysis techniques detected  $\text{TiO}_2$ , which in addition has a melting temperature above  $1800^\circ\text{C}$ . The first reaction (eq 6.2) shows the incorporation reaction of Co into BNT as discussed in Chapter 5.4. A reaction according to eq 6.3 also generates  $\text{Co}_2\text{TiO}_4$ , but BNT does not incorporate any cobalt, which leads to an effective Ti-deficiency. However, Ti-deficient BNT appears to be unstable. Spreitzer et al. synthesized Ti-deficient BNT and observed two secondary phases,  $\text{Bi}_2\text{O}_3$  and a sodium titanate ( $\text{Na}_8\text{Ti}_5\text{O}_{14}$ ), above  $850^\circ\text{C}$  [Spr07]. In the case of cobalt doping, Ti is preferentially incorporated into  $\text{Co}_2\text{TiO}_4$ , possibly consuming too much Ti for the formation of a sodium titanate phase. Instead, superfluous bismuth oxide and sodium oxide might form a  $\text{NaBiO}_2$  melt. Since  $\text{NaBiO}_2$  has a melting point below the observed liquid-phase sintering effect, the decomposition of BNT either requires higher temperatures (which is unlikely, given the results of Spreitzer's group), or the Ti-deficit only becomes significant at elevated sintering temperatures and triggers the BNT decomposition. The latter could be explained by residual  $\text{Co}_3\text{O}_4$ , which gradually incorporates Ti from BNT via diffusion. Hence, the amount of liquid phase generated is limited by the Ti deficit in BNT, which is linked to the total dopant concentration.

At temperatures above  $1000^\circ\text{C}$ ,  $\text{Bi}_2\text{O}_3$  preferentially evaporates from the melt film of  $\text{NaBiO}_2$ . The excess Na is accommodated in the sodium cobalt titanate phase. A possible formation mechanism is exemplarily shown in eq 6.5:



The melt-like appearance of the sodium cobalt titanate phase (cf. Chapter 5.1) is probably due to partial melting, which was reported by Shukaev and Volochaev for some of the compositions of the system  $\text{Na}_2\text{O-TiO}_2\text{-CoO}$  at  $1000^\circ\text{C}$  to  $1050^\circ\text{C}$  [Shu95].

### 6.5.4 Phase Development During Sintering

Figure 6.10 gives an overview over the possible phase sequence in cobalt-doped BNT. The oxide and carbonate powders are mixed and calcined at  $800^\circ\text{C}$ . The solid state reaction produces  $\text{Bi}_{0.5}\text{Na}_{0.5}\text{TiO}_3$  which has incorporated some  $\text{Co}^{3+}$  instead of  $\text{Ti}^{4+}$ . Although not visible in XRD patterns because of the small amount, some  $\text{Co}_2\text{TiO}_4$  must also have formed. In addition, a solid solution spinel with the end members  $\text{Co}_3\text{O}_4$  and  $\text{Co}_2\text{TiO}_4$  is likely still present. Upon heating during the sintering cycle, the interdiffusion process of Co and Ti between BNT and  $\text{Co}_2\text{TiO}_4$  continues and generates Ti-deficient BNT. This instable phase decomposes to  $\text{NaBiO}_2$ , which forms a melt film on the grain boundaries and causes a small degree of liquid-phase sintering. Gradually,  $\text{Bi}_2\text{O}_3$  starts to evaporate from the melt. Above  $1000^\circ\text{C}$ , the excess Na stabilizes a sodium cobalt titanate phase that

begins to melt partially at around 1075 °C. A valence change of cobalt in BNT from  $\text{Co}^{3+}$  to  $\text{Co}^{2+}$  at approx. 950 °C necessitates the evaporation of oxygen, which is trapped in the closing pores and causes swelling.

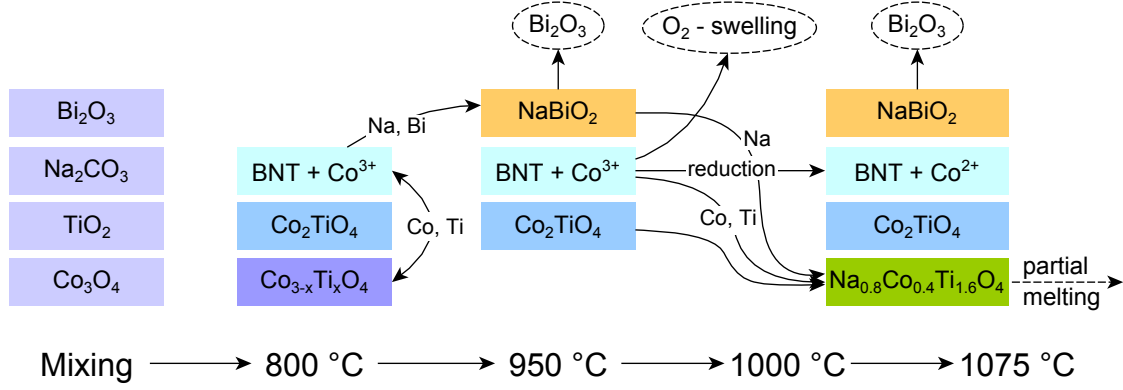


**Figure 6.10:** Proposed reaction sequence in cobalt-doped BNT from starting powders to sintering temperatures above 1075 °C.

### 6.5.5 Sintering Kinetics

As explained in Chapter 4.2.2, the kinetic field provides insight into the kinetics of the sintering process of a ceramic. From the slope of the iso-lines in the kinetic field diagram, the apparent activation energy  $E_a$  can be calculated. In addition, the relation between densification and coarsening can be deduced.

To this end, it is helpful to compare the experimental results to theoretical simulations. The sintering kinetics with various combinations of the activation energy for grain growth  $E_G$  and the activation energy for densification  $E_{\text{act}}$  were calculated in [Rae09b]. The iso-lines were found to have a constant slope and parallel shift when  $E_G$  and  $E_{\text{act}}$  were equal. When the activation energy for grain growth  $E_G$  was bigger than that for densification  $E_{\text{act}}$ , an anticlockwise rotation of the iso-lines was obtained, and the apparent activation energy  $E_a$  decreased. For an inverse relationship of  $E_G$  and  $E_{\text{act}}$ , the rotation was clockwise with increasing  $E_a$ .

The slope of the iso-strain lines of pure BNT was almost constant. Hence, the two activation energies can be considered equal, probably with a tendency toward a higher  $E_{\text{act}}$ , as the apparent activation energy increased slightly during the second half of the shrinkage process (cf. Figure 6.9). In contrast, the iso-strain lines of BNT doped with 2.6 mol % Co began to rotate anticlockwise at about 850 °C and the apparent activation energy decreased. Consequently,  $E_G$  must be higher than  $E_{\text{act}}$ .

Two mechanisms related to doping can decrease the grain boundary mobility, both of which are considered to contribute to the increase in  $E_G$ . (1) The secondary phase particles, mostly  $\text{Co}_2\text{TiO}_4$ , are initially finely dispersed between the BNT grains. They

have a pinning effect on the grain boundaries [Rah03]. (2) A fraction of the dopant atoms is dissolved in BNT. Due to electrostatic interactions, the solute (i.e., the dopant atoms) may be distributed nonuniformly in the grain boundary. The diffusivity of the solute across the grain boundary generally differs from that of the host material. When the boundary starts to move, the generated concentration gradient results in a retarding force. It can be overcome if a sufficiently high activation energy is provided. At fast heating rates the required energy is provided at lower densities as compared to slow heating. The grain boundaries can break free and cause secondary phase particles as well as pores to be overgrown and enclosed inside grains. Figure 5.2d in Chapter 5.1 depicts this situation for BNT doped with 2.6 mol % Co and a heating rate of  $5 \text{ K min}^{-1}$ .

To summarize, the anticlockwise rotation of the iso-strain lines is probably due to enhanced grain growth at higher heating rates, which slows the densification process.

### 6.5.6 Sintering Mechanisms

It was demonstrated above that cobalt-doping greatly reduces the necessary sintering temperature of BNT while maintaining the desired high final density. This is achieved by two co-active sintering mechanisms:

The first one involves the formation of a secondary phase,  $\text{Co}_2\text{TiO}_4$ , thereby generating Ti vacancies in BNT. The second mechanism provides aliovalent  $\text{Co}^{3+}$  ions to replace most of the missing  $\text{Ti}^{4+}$  ions in the BNT lattice. To maintain electroneutrality in the perovskite, oxygen vacancies are generated, which enhance the bulk diffusivity of both anions and cations. The mass transport at lower temperatures is thereby facilitated and the densification promoted. The formation of a small amount of liquid phase due to the Ti-understoichiometry in BNT further assists in the densification process.

An adverse effect to densification was found at high sintering temperatures. The dopant atoms in BNT undergo a valence transition from  $\text{Co}^{3+}$  to  $\text{Co}^{2+}$ , which causes additional oxygen evaporation. The gas gets trapped in closed pores and exerts a pressure high enough to overcome the sintering stress and induce swelling of the ceramic body. This effect could be mitigated by sintering under high oxygen partial pressures and low sintering temperatures. Control of the sintering atmosphere, e.g. by sintering with additional  $\text{Bi}_2\text{O}_3$  powder in the furnace, might help to combat the issue of Bi vaporization. In turn, the formation of the sodium cobalt titanate phase would be suppressed.





## 7 Piezoelectric and Dielectric Characterization

The dielectric and piezoelectric characterization is important to judge the quality of the piezoceramic with respect to possible industrial applications. A great multitude of parameters can be measured under various conditions, depending on the information that is desired. Since the piezoelectric properties of doped BNT were not the focus of this work, the piezo- and dielectric characterization was limited to the following key parameters: Piezoelectric coefficient  $d_{33}$ , temperature-dependent dielectric properties (permittivity  $\varepsilon$  and dielectric loss  $\tan \delta$ ), and, derived thereof, the electrical conductivity and the depolarization temperature  $T_d$ .

### 7.1 Dielectric Permittivity and Loss Tangent

The relative dielectric permittivity at constant stress,  $\varepsilon_r$ , and the dielectric loss  $\tan \delta$  were determined for samples sintered at 1075 °C via capacitance measurements. A frequency range from 0.1 kHz to 1.0 MHz was covered simultaneously. Samples which were depolarized (by preceding measurements above their depolarization temperature) showed very broad peaks at the first phase transition temperature (temperature of depolarization  $T_d$ ), which prevented the determination of  $T_d$ . The transition signal could be enhanced by measuring poled samples [Rob98] that had been aged for at least 24 h after poling.  $T_d$  was then determined from the first derivatives of the real and imaginary part of the permittivity  $\varepsilon'$  and  $\varepsilon''$ , as explained in Chapter 4.3. Due to time constraints, the data for the sample containing 1.0 mol % Co could not be recorded completely.

Figure 7.1 shows the dielectric permittivity and loss tangent of pure BNT and BNT doped with 0.1 mol % Co from room temperature to 550 °C. A strong frequency dispersion of the dielectric properties was found at all dopant levels. This is typical of a relaxor-type behavior [Dan11].

In pure BNT, the first anomaly of  $\varepsilon_r$  at 200 °C is clearly visible for all frequencies tested. In the doped sample, the observed apparent permittivity is higher than for pure BNT and it increases more strongly with temperature. This is probably due to an increased electrical conductivity of the doped material. As a consequence, the inflection point of  $\varepsilon_r$  is no longer discernible at the lowest measurement frequency of 0.1 kHz. At dopant

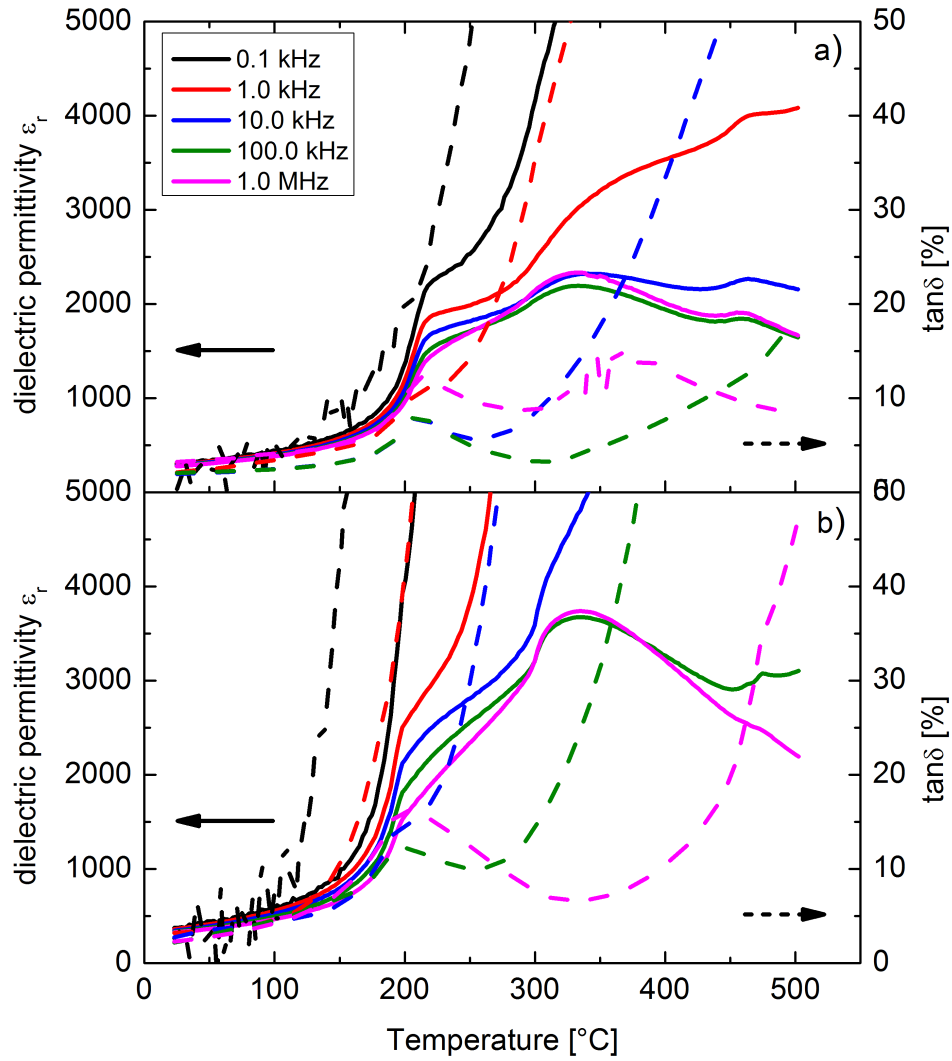


**Figure 7.1:** Relative dielectric permittivities  $\varepsilon_r$  (solid lines) and loss  $\tan \delta$  (dashed lines) of a) pure BNT and b) BNT doped with 0.1 mol % Co as a function of temperature; the samples were aged for at least 24 h before measuring.

concentrations of 0.5 mol % Co and higher, the contribution of the conductivity began to mask the temperature of the phase transition almost completely (see Figure A.4 in the appendix).

## 7.2 Electrical Conductivity

The AC (alternating current) electrical conductivity  $\sigma(\omega)$  was calculated from the dielectric measurements at a frequency of 0.1 kHz using the relationship

$$\sigma(\omega) = \omega \varepsilon_0 \varepsilon''(\omega) = \omega \varepsilon_0 \varepsilon' \tan \delta \quad (7.1)$$

with  $\omega$  = angular frequency,  $\varepsilon_0$  = dielectric permittivity of vacuum ( $8.8514 \times 10^{-12} \text{ F m}^{-1}$ ),  $\varepsilon'$  and  $\varepsilon''$  = real and imaginary parts of the relative dielectric permittivity. The results for the poled samples are shown in Figure 7.2.

In general, the AC conductivity scaled with the measuring frequency. At 40 °C, the doped material showed a slightly lower conductivity than pure BNT (cf. Table 7.1). When the temperature was increased, the conductivity in doped BNT rose by approx. one order of magnitude, which is much stronger than the increase in cobalt-free BNT. This effect was more pronounced at low frequencies, indicating that the conduction mechanism is slow and thermally activated, while at room temperature a faster mechanism is involved.

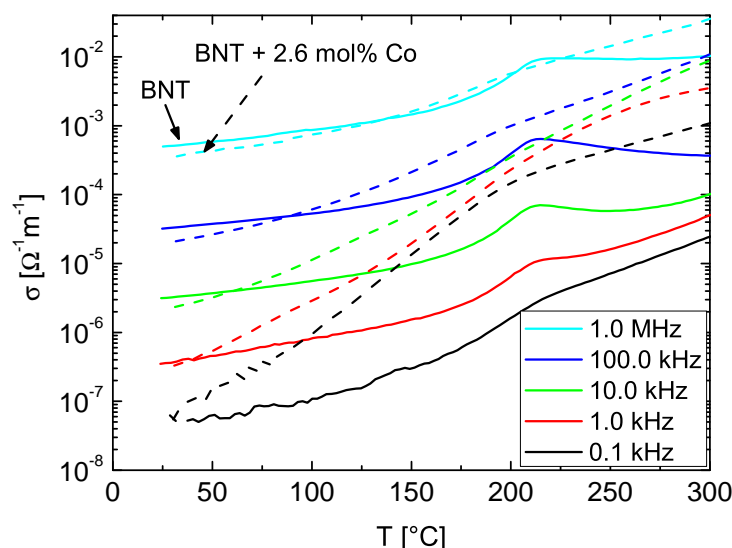


**Figure 7.2:** Calculated AC conductivity of poled BNT samples at various frequencies as a function of temperature. Solid lines - BNT, dashed lines - BNT with 2.6 mol % Co. The graph of BNT at 0.1 kHz was interpolated from the original data which was very noisy between room temperature and 150 °C.

**Table 7.1:** AC conductivities of BNT and BNT doped with 2.6 mol % Co at 0.1 kHz

Conductivity $[(\Omega\text{m})^{-1}]$	40 °C	100 °C
Pure BNT	$2.1 \times 10^{-7}$	$3.0 \times 10^{-7}$
BNT + 2.6 mol % Co	$1.8 \times 10^{-7}$	$1.7 \times 10^{-6}$

### 7.3 Depolarization Temperature

Table 7.2 shows the depolarization temperatures  $T_d$  of pure and doped BNT as a function of the cobalt concentration. The values were derived from the first derivatives of  $\varepsilon'$  and  $\varepsilon''$  as described in Chapter 4.3. For pure BNT,  $T_d$  was found to be 209 °C.

With the addition of small amounts of Co, the depolarization temperature decreased strongly. A further increase in the dopant level had no measurable effect. One should however keep in mind that the phase transition temperature for BNT doped with 0.5 mol % and 2.6 mol % Co was masked by the strong increase of the dielectric permittivity and thus the values may be less accurate than for low dopant concentrations. Methods more suitable to measure the depolarization temperature of samples with high electrical conductivity are the temperature-dependent in situ determination of  $d_{33}$  or the temperature-dependent resonance measurement [Ant11].

**Table 7.2:** Depolarization temperatures for pure and doped BNT (1075 °C) derived from dielectric measurements:

mol % Co	0.0	0.1	0.5	1	2.6	0.0 [Hir09]
$T_d$ [°C]	209	192	188	-	191	187

### 7.4 Piezoelectric Coefficient

Figure 7.3 shows the piezoelectric coefficient  $d_{33}$  as a function of the dopant concentration and the sintering temperature. The highest  $d_{33}$  of  $(69 \pm 1) \text{ pC N}^{-1}$  was achieved for pure BNT sintered at 1075 °C. When cobalt was added, the piezoelectric coefficient dropped, at first rapidly, then much more slowly, down to a minimum of  $(38 \pm 1) \text{ pC N}^{-1}$  at 2.6 mol % Co. The  $d_{33}$  for samples sintered at 1150 °C had a comparable value of  $(68 \pm 1) \text{ pC N}^{-1}$  for pure BNT and showed the same decrease with increasing dopant level as for the samples sintered at 1075 °C. This decrease in piezoelectric coefficient is typical of a ‘hard’ doping effect.

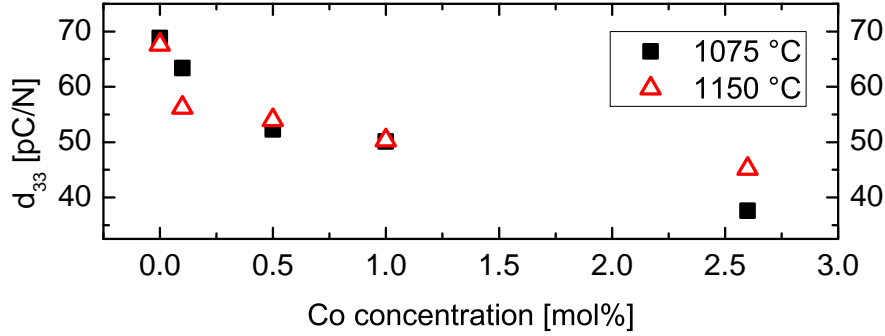


**Figure 7.3:** Piezoelectric coefficient  $d_{33}$  of samples with varying cobalt concentrations, sintered at 1075 °C and 1150 °C.

## 7.5 Discussion

The relative dielectric permittivity  $\varepsilon_r$  and the dielectric loss  $\tan \delta$  were determined as a function of temperature. All samples showed a pronounced frequency dispersion. This behavior is characteristic for relaxor-type materials like BNT [Röd09, Dan11].

In the doped specimens,  $\varepsilon_r$  strongly increased with increasing temperature, to a point where the first anomaly of  $\varepsilon_r$ , which indicates the temperature of ferroelectric-antiferroelectric phase transition, was almost completely masked at the low frequencies. This is a consequence of the high electrical conductivity of the samples, especially at elevated temperatures.

The AC conductivity of pure BNT at 40 °C was comparable to values reported in the literature (cf. [Nag01, Hir09], DC measurements). Doped compositions with a higher cobalt concentration and thus a greater defect concentration showed an increased conductivity.

Hiruma et al. [Hir09] attributed the conductivity of BNT to Bi vacancies and the resulting oxygen vacancies, but they did not specify the conduction mechanism. The activation energy for ionic conductivity (oxygen ions) at room temperature is considered too high to result in significant conduction at moderate temperatures [Che10]. Instead, 3d electrons from  $\text{Ti}^{4+}$  could enter the conduction band. Another contribution probably arises from dipole relaxations, the dipoles being formed between Ti atoms and neighboring oxygen vacancies [Mah07]. In order to determine the mechanisms leading to conduction in the present study, more extensive experiments would be necessary, such as detailed AC and DC measurements and impedance spectroscopy.

A depolarization temperature of 209 °C was found for pure BNT sintered at 1075 °C. This is 22 °C above the depolarization temperature given by Hiruma et al. [Hir09], who used the same method to determine  $T_d$ . The difference might be due to the temperature calibration of the respective heating devices used in the two studies.

With the addition of 0.1 mol % Co,  $T_d$  decreased by 22 °C. A further increase in dopant concentration did not affect  $T_d$ . It remained constant at around 190 °C. This phenomenon

might be related to insufficient poling as a result of the electrical conductivity.

The piezoelectric coefficient  $d_{33}$  for pure BNT was comparable to that found by Hiruma and his group ( $69 \text{ pC N}^{-1}$  as compared to  $73 \text{ pC N}^{-1}$  [Hir09]). Doping with cobalt led to a decrease of  $d_{33}$ . A similar behavior was observed by Xu et al. [Xu08b] for cobalt-doped BNT-BT. Their depolarization temperature, though, increased with cobalt addition. A different result was obtained by Li and his group [Li04], who reported an improved piezoelectric coefficient  $d_{33}$  and explained this by enhanced grain growth in the doped samples.

In PZT, cobalt acts as a ‘hard’ dopant [Xu91], that is, it leads to an increase of the Curie temperature  $T_c$ , but at the same time decreases  $d_{33}$ ,  $\varepsilon_r$  and  $\tan \delta$ . The lower-valent  $\text{Co}^{3+}$  (or  $\text{Co}^{2+}$ ) replaces  $\text{Ti}^{4+}$  and thus causes oxygen vacancies for charge compensation. These vacancies are believed to have a clamping effect on the domain wall motion [Mou03], thereby increasing the coercive field  $E_C$ . As a result, full poling is harder to achieve and  $d_{33}$  will be lower than in non-doped materials poled under the same conditions. Similarly, the poled ceramic is harder to depolarize, resulting in an increase of  $T_d$ .

In this study, however, both  $d_{33}$  and  $T_d$  were lowered by the addition of a supposedly hard dopant. The most likely explanation is that owing to the high electrical conductivity full poling could not be accomplished. As a result, the dielectric and piezoelectric properties of the doped ceramic are inferior to those of pure BNT.

## 8 Conclusion

Bismuth sodium titanate,  $\text{Bi}_{0.5}\text{Na}_{0.5}\text{TiO}_3$  (BNT) is considered a promising lead-free alternative to piezoelectric lead zirconate titanate. Yet, up to now, the dielectric and piezoelectric properties of pure BNT ceramics do not meet the requirements for practical applications. Doping is one way to tailor and enhance the performance of BNT. However, the role of dopants during the sintering process and their effect on the ceramic's final properties has so far received little attention from a microscopic point of view.

In this study the effects of cobalt-doping on BNT were investigated with regard to the phase formation, the lattice site preference of the dopant, the sintering behavior and the dielectric and piezoelectric properties. The results can be summarized as follows:

1. Cobalt-doping of BNT was invariably accompanied by the formation of the spinel phase  $\text{Co}_2\text{TiO}_4$  and small amounts of a sodium cobalt titanate phase when the total dopant level exceeded 0.1 mol % Co. The secondary phases were identified by scanning electron microscopy combined with energy dispersive X-ray spectrometry (EDX). In the literature, BNT- $\text{BaTiO}_3$  doped with Co had so far been reported as single phase. However, these reports were based on X-ray diffraction analyses, which in this study were not sensitive enough to reveal additional phases either.
2. Electron probe micro analysis confirmed that about one third of the added dopant was incorporated into the BNT lattice. An upper solubility limit of Co in BNT could not be determined. The cobalt concentration in BNT continued to increase with increasing dopant levels up to 2.1 mol % when 10.6 mol % Co were added. The incorporation of Co was mainly accomplished during the calcination at 800 °C, as demonstrated by scanning transmission electron microscopy combined with EDX.
3. The preferred lattice site of cobalt in the BNT structure was identified by X-ray absorption near-edge structure (XANES) spectra. The experimental spectra were compared to ab-initio calculations based on model structures of the local atomic environment of Co. Cobalt was found to occupy the octahedral B-site of the perovskite, i.e., it replaced  $\text{Ti}^{4+}$ . It was not possible to reliably determine the valence state of Co by XANES due to the lack of proper standard materials, but results from the sintering experiments suggest it was incorporated in its trivalent state. Above 950 °C,  $\text{Co}^{3+}$  was probably reduced to  $\text{Co}^{2+}$  accompanied by the release of oxygen for charge compensation. The trapped gas is believed to have caused swelling of the material in the late sintering stage.

4. To maintain charge neutrality in cobalt-doped BNT, oxygen vacancies were generated. The vacancies facilitate oxygen diffusion in the perovskite. Since the diffusivity of the cations is coupled with the oxygen diffusion, the overall diffusivity was enhanced as well. As a result, the densification became significant at reduced sintering temperatures as compared to pure BNT. High final densities were reached even at 1000 °C, which was 150 K below the sintering temperature of the non-doped material.
5. Regarding the sintering kinetics, cobalt-doping of BNT appeared to increase the activation energy for grain growth,  $E_G$ . The reasons are assumed to be a pinning effect from secondary phase particles and pores as well as a dragging force from incorporated cobalt atoms.
6. Contrary to expectations, doping with a supposedly ‘hard’ dopant did not increase, but rather decrease the depolarization temperature. The piezoelectric coefficient  $d_{33}$ , too, dropped with increasing dopant concentrations. This was attributed to the high electrical conductivity of the samples, which prevented full poling. The conductivity probably is related to the relaxation of dipoles which are formed between Ti atoms and neighboring oxygen vacancies.

To sum up, cobalt-doping provides a way to greatly reduce the sintering temperature while at the same time allowing to sinter BNT ceramics to high densities. A low sintering temperature has several advantages. First, the evaporation of Bi is less severe, which is expected to be beneficial with regard to the piezoelectric properties. Second, the energy consumption during the heat treatment process is reduced. Third, a lower sintering temperature allows for the use of electrode materials with low melting temperatures.

It was demonstrated that cobalt is located on the Ti-site in the BNT lattice. The role it plays during sintering was examined. In order to fully understand the way in which cobalt modifies the dielectric and piezoelectric properties, however, further careful studies are required. They should take into account possible effects from the secondary phases.

From an application point of view, adding 0.5 mol % Co yielded the best compromise between the degrading effect on the dielectric and piezoelectric properties and the favorable reduction in sintering temperature and obtainable density.

To limit the amount of Bi and O evaporation, sintering in a controlled atmosphere should be attempted. Additional  $\text{Bi}_2\text{O}_3$  powder and a high oxygen partial pressure at a low sintering temperature might decrease the swelling and the Bi loss. It might also affect the electrical conductivity, a decrease of which is expected to enable full poling and enhance the piezoelectric properties.

This study, though certainly not exhaustive, shows that comprehensively examining the effects of a dopant on a piezoelectric ceramic can help to understand in what ways the material is being affected. Such knowledge will make it possible to select specific dopants in order make systematic and targeted modifications of piezoelectric materials.



# References

- [Ack10] J. Acker, H. Kungl, and M. J. Hoffmann. Influence of Alkaline and Niobium Excess on Sintering and Microstructure of Sodium Potassium Niobate ( $\text{K}_{0.5}\text{Na}_{0.5}\text{NbO}_3$ ). *J. Am. Ceram. Soc.*, 93(5):1270–1281, 2010.
- [Aks10a] E. Aksel, E. Erdem, P. Jakes, J. L. Jones, and R. A. Eichel. Defect Structure and Materials ‘Hardening’ in  $\text{Fe}_2\text{O}_3$ -doped  $(\text{Bi}_{0.5}\text{Na}_{0.5})\text{TiO}_3$  Ferroelectrics. *Appl. Phys. Lett.*, 97(1):012903, 2010.
- [Aks10b] E. Aksel and J. L. Jones. Advances in Lead-Free Piezoelectric Materials for Sensors and Actuators. *Sensors*, 10:1935–1954, 2010.
- [Aks10c] E. Aksel and J. L. Jones. Phase Formation of Sodium Bismuth Titanate Perovskite During Solid-State Processing. *J. Am. Ceram. Soc.*, 93(10):3012–3016, 2010.
- [Aks11] E. Aksel, J. S. Forrester, J. L. Jones, P. A. Thomas, K. Page, and M. R. Suchomel. Monoclinic Crystal Structure of Polycrystalline  $\text{Na}_{0.5}\text{Bi}_{0.5}\text{TiO}_3$ . *Appl. Phys. Lett.*, 98:152901, 2011.
- [Aks12] E. Aksel, J. S. Forrester, B. Kowalski, M. Deluca, D. Damjanovic, and J. L. Jones. Structure and Properties of Fe-modified  $\text{Na}_{0.5}\text{Bi}_{0.5}\text{TiO}_3$  at Ambient and Elevated Temperature. *Phys. Rev. B*, 85(2):024121, 2012.
- [Ant11] E. M. Anton, W. Jo, D. Damjanovic, and J. Rödel. Determination of Depolarization Temperature of  $(\text{Bi}_{0.5}\text{Na}_{0.5})\text{TiO}_3$ -Based Lead-Free Piezoceramics. *J. Appl. Phys.*, 110(9):094108, 2011.
- [Arm88] J. T. Armstrong. Quantitative Analysis of Silicate and Oxide Materials: Comparison of Monte Carlo, ZAF, and  $\phi(\rho z)$  Procedures. In D. E. Newbury, editor, *Proceedings of the 23rd annual conference of the Microbeam Analysis Society*, pages 239–246. San Francisco Press, San Francisco, 1988.
- [Bab07] J. Baber, A. Klimera, and F. Raether. In Situ Measurement of Dimensional Changes and Temperature Fields During Sintering with a Novel Thermo-optical Measuring Device. *J. Eur. Ceram. Soc.*, 27(2–3):701–705, 2007.

- [Bal02] C. W. Bale, P. Chartrand, S. A. Degterov, G. Eriksson, K. Hack, R. Ben Mahfoud, J. Melancon, A. D. Pelton, and S. Petersen. FactSage Thermochemical Software and Databases. *Calphad*, 26(2):189–228, 2002.
- [Bar04] A. F. Barzegar, D. Damjanovic, and N. Setter. The Effect of Boundary Conditions and Sample Aspect Ratio on Apparent  $d_{33}$  Piezoelectric Coefficient Determined by Direct Quasistatic Method. *IEEE Trans. Ultra. Ferro. Freq. Control*, 51(3):262–270, 2004.
- [Bok06] A. Bokov and Z. G. Ye. Recent Progress in Relaxor Ferroelectrics with Perovskite Structure. *J. Mater. Sci.*, 41(1):31–52, 2006.
- [Cad46] W. G. Cady. *Piezoelectricity*. McGraw-Hill, New York, 1946.
- [Cao04] D. Cao, I. K. Jeong, R. H. Heffner, T. Darling, J. K. Lee, F. Bridges, J. S. Park, and K. S. Hong. Local Structure Study of the Off-Center Displacement of Ti and Zr across the Morphotropic Phase Boundary of  $\text{PbZr}_{(1-x)}\text{Ti}_x\text{O}_3$ . *Phys. Rev. B*, 70(22):224102, 2004.
- [Car55] R. Carter and F. D. Richardson. 7:336–343, 1955.
- [Che03] M. Chen, B. Hallstedt, and L. J. Gauckler. Thermodynamic Assessment of the Co-O System. *J. Phase Equil.*, 24(3):212–227, 2003.
- [Che07] Q. Chen, L. Chen, Q. Li, X. Yue, D. Xiao, and J. Zhu. Piezoelectric Properties of  $\text{K}_4\text{CuNb}_8\text{O}_{23}$  modified  $(\text{Na}_{0.5}\text{K}_{0.5})\text{NbO}_3$  Lead-Free Piezoceramics. *J. Appl. Phys.*, 102(10):104109, 2007.
- [Che08a] M. Chen, Q. Xu, B.-H. Kim, B. K. Ahn, J. H. Ko, W. J. Kang, and O. J. Nam. Structure and Electrical Properties of  $(\text{Na}_{0.5}\text{Bi}_{0.5})_{1-x}\text{Ba}_x\text{TiO}_3$  Piezoelectric Ceramics. *J. Eur. Ceram. Soc.*, 28(4):843–849, 2008.
- [Che08b] B. Cherdhirunkorn, M. F. Smith, S. Limpijumnong, and D. A. Hall. EXAFS Study on the Site Preference of Mn in Perovskite Structure of PZT Ceramics. *Ceram. Int.*, 34(4):727–729, 2008.
- [Che10] P.-Y. Chen, C.-C. Chou, T.-Y. Tseng, and H. Chen. Second Phase and Defect Formation in  $\text{Bi}_{0.5}\text{Na}_{0.5-x}\text{K}_x\text{TiO}_3$  Ceramics. *Jpn. J. Appl. Phys.*, 49(6):061506, 2010.
- [Chi06] Y.-M. Chiang, S. A. Sheets, G. W. Farrey, N. W. I. V. Hagood, A. Soukhovak, and H. Wang. Electromechanical Actuators, 2006.
- [Cho11] C.-S. Chou, C.-L. Liu, C.-M. Hsiung, and R.-Y. Yang. Preparation and Characterization of the Lead-free Piezoelectric Ceramic of  $\text{Bi}_{0.5}\text{Na}_{0.5}\text{TiO}_3$  Doped with CuO. *Powder Technol.*, 210(3):212–219, 2011.

- [Chr10] A. Chroneos, R. Vovk, I. Goulatis, and L. Goulatis. Oxygen Transport in Perovskite and Related Oxides: A Brief Review. *J. Alloys Compd.*, 494(1-2):190–195, 2010.
- [Chu02] B.-J. Chu, D.-R. Chen, G.-R. Li, and Q.-R. Yin. Electrical Properties of  $\text{Na}_{1/2}\text{Bi}_{1/2}\text{TiO}_3$ - $\text{BaTiO}_3$  Ceramics. *J. Eur. Ceram. Soc.*, 22(13):2115–2121, 2002.
- [Coh92] R. E. Cohen. Origin of Ferroelectricity in Perovskite Oxides. *Nature*, 358:136–138, 1992.
- [Dam98] D. Damjanovic. Ferroelectric, Dielectric and Piezoelectric Properties of Ferroelectric Thin Films and Ceramics. *Rep. Prog. Phys.*, 61(9):1267–24, 1998.
- [Dam01] D. Damjanovic. Piezoelectric Properties of Perovskite Ferroelectrics: Unsolved Problems and Future Research. *Ann. Chim. Sci. Mat.*, 26(1), 2001.
- [Dam10] D. Damjanovic, N. Klein, L. Jin, and V. Porokhonsky. What Can Be Expected From Lead-Free Piezoelectric Materials? *Funct. Mater.Lett.*, 3(1):5–13, 2010.
- [Dan11] J. E. Daniels, W. Jo, J. Rödel, D. Rytz, and W. Donner. Structural Origins of Relaxor Behavior in a  $0.96(\text{Bi}_{1/2}\text{Na}_{1/2})$ - $\text{TiO}_3$ - $0.04\text{BaTiO}_3$  Single Crystal under Electric Field. *Appl. Phys. Lett.*, 98(25):252904, 2011.
- [Dav00] R. A. Davies, M. S. Islam, A. V. Chadwick, and G. E. Rush. Cation Dopant Sites in the  $\text{CaZrO}_3$  Proton Conductor: A Combined EXAFS and Computer Simulation Study. *Solid State Ionics*, 130(1-2):115–122, 2000.
- [Dav11] M. Davies, E. Aksel, and J. L. Jones. Enhanced High-Temperature Piezoelectric Coefficients and Thermal Stability of Fe- and Mn-Substituted  $\text{Na}_{0.5}\text{Bi}_{0.5}\text{TiO}_3$  Ceramics. *J. Am. Ceram. Soc.*, 2011.
- [Du06] H. Du, Z. Li, F. Tang, Q. Shaobo, Z. Pei, and W. Zhou. Preparation and Piezoelectric Properties of  $(\text{K}_{0.5}\text{Na}_{0.5})\text{NbO}_3$  Lead-Free Piezoelectric Ceramics with Pressure-Less Sintering. *Mater. Sci. Eng. B*, 131(1-3):83–87, 2006.
- [Eic11] R. A. Eichel. Structural and Dynamic Properties of Oxygen Vacancies in Perovskite Oxides-Analysis of Defect Chemistry by Modern Multi-Frequency and Pulsed EPR Techniques. *Phys. Chem. Chem. Phys.*, 13(2):368–384, 2011.
- [Eur03a] EU-Directive 2002/95/EC 2003 Restriction of the Use of Certain Hazardous Substances in Electrical and Electronic Equipment (RoHS). *Off. J. Eur. Union*, 46(L37):19–23, 2003.
- [Eur03b] EU-Directive 2002/96/EC: Waste Electrical and Electronic Equipment (WEEE). *Off. J. Eur. Union*, 46(L37):24–38, 2003.

- [Ger85] R. M. German. *Liquid Phase Sintering*. Plenum Press, New York and London, 1985.
- [Ger96] R. M. German. *Sintering Theory and Practice*. John Wiley & Sons, Inc., New York, 1996.
- [Gol26] V. M. Goldschmidt, T. F. Barth, G. O. Lunde, and W. Zachariasen. *Geochemische Verteilungsgesetze der Elemente: 7. Gesetze der Krystallochemie*. Skrifter utgitt av det Norske Videnskaps-Akademi i Oslo, Oslo, 1926.
- [GP04] J.-R. Gomah-Pettry, A. N. Salak, P. Marchet, V. M. Ferreira, and J.-P. Mercurio. Ferroelectric Relaxor Behaviour of  $\text{Na}_{0.5}\text{Bi}_{0.5}\text{TiO}_3$ - $\text{SrTiO}_3$  Ceramics. *Phys. Status Solidi B*, 241(8):1949–1956, 2004.
- [Grö11] M. Gröting, S. Hayn, and K. Albe. Chemical Order and Local Structure of the Lead-Free Relaxor Ferroelectric  $\text{Na}_{1/2}\text{Bi}_{1/2}\text{TiO}_3$ . *J. Solid State Chem.*, 184(8):2041–2046, 2011.
- [Hae99] G. H. Haertling. Ferroelectric Ceramics: History and Technology. *J. Am. Ceram. Soc.*, 82(4):797–818, 1999.
- [Hel07] U. Helbig. Size Effect in Low Grain Size Neodymium Doped PZT Ceramics. *J. Eur. Ceram. Soc.*, 27(7):2567–2576, 2007.
- [Her97] A. Herabut and A. Safari. Processing and Electromechanical Properties of  $(\text{Bi}_{0.5}\text{Na}_{0.5})_{(1-1.5x)}\text{La}_x\text{TiO}_3$  Ceramics. *J. Am. Ceram. Soc.*, 80(11):2954–2958, 1997.
- [Hir90] K. Hirota, T. Inoue, N. Mochida, and A. Ohtsuka. Study of Germanium Spinel (Part 3). *J. Ceram. Soc. Jpn.*, 98(9):976–986, 1990.
- [Hir09] Y. Hiruma, H. Nagata, and T. Takenaka. Thermal Depoling Process and Piezoelectric Properties of Bismuth Sodium Titanate Ceramics. *J. Appl. Phys.*, 105(8):084112, 2009.
- [Hol95] A. F. Holleman, E. Wiberg, and N. Wiberg. *Lehrbuch der anorganischen Chemie*. de Gruyter, Berlin, 101 edition, 1995.
- [Hol05] E. Hollenstein, M. Davies, D. Damjanovic, and N. Setter. Piezoelectric Properties of Li- and Ta-Modified  $(\text{K}_{0.5}\text{Na}_{0.5})\text{NbO}_3$  Ceramics. *Appl. Phys. Lett.*, 87(18):182905, 2005.
- [Hua08] X. Huang and F. Raether. In situ Measurements on Sintering Kinetics of PZT Ceramics. In J. G. Heinrich and C. Aneziris, editors, *Proceedings of the 10th International Conference of the European Ceramic Society*, pages 196–200. Göller, 2008.

- [Hua09] X. Huang and F. Raether. Role of Impurities in the Sintering Behavior and Properties of Lead Zirconate Titanate Ceramics. *J. Am. Ceram. Soc.*, 92(9):2011–2016, 2009.
- [Ike74] S. Ikegami and I. Ueda. Piezoelectricity in Ceramics of Ferroelectric Bismuth Compound with Layer Structure. *Jpn. J. Appl. Phys.*, 13:1572–1577, 1974.
- [Jaf54] B. Jaffe, R. S. Roth, and S. Marzullo. Piezoelectric Properties of Lead Zirconate-Lead Titanate Solid-Solution Ceramics. *J. Appl. Phys.*, 25(6):809–810, 1954.
- [Jaf71] B. Jaffe, W. R. Cook, and H. Jaffe. *Piezoelectric Ceramics*. Acad. Press, London, 1971.
- [Jam68] P. B. Jamieson, S. C. Abrahams, and J. L. Bernstein. Ferroelectric Tungsten Bronze-Type Crystal Structures. I. Barium Strontium Niobate  $\text{Ba}_{0.27}\text{Sr}_{0.75}\text{Nb}_2\text{O}_{5.78}$ . *J. Chem. Phys.*, 48(11):5048–5057, 1968.
- [Jo11] W. Jo, J. B. Ollagnier, J. L. Park, E. M. Anton, O. J. Kwon, C. Park, H. H. Seo, J. S. Lee, E. Erdem, R. A. Eichel, and J. Rödel. CuO as a Sintering Additive for  $(\text{Bi}_{1/2}\text{Na}_{1/2})\text{TiO}_3$ - $\text{BaTiO}_3$ - $(\text{K}_{0.5}\text{Na}_{0.5})\text{NbO}_3$  Lead-Free Piezoceramics. *J. Eur. Ceram. Soc.*, 31(12):2107–2117, 2011.
- [Jon02] G. O. Jones and P. A. Thomas. Investigation of the Structure and Phase Transitions in the Novel A-Site Substituted Distorted Perovskite Compound  $\text{Na}_{0.5}\text{Bi}_{0.5}\text{TiO}_3$ . *Acta Crystallogr. B*, (58):168–178, 2002.
- [Kee12] D. S. Keeble, E. R. Barney, D. A. Keen, M. G. Tucker, J. Kreisel, and P. A. Thomas. Bifurcated Polarization Rotation in Bismuth-Based Piezoelectrics. *Adv. Funct. Mater.*, 22(16):n/a, 2012.
- [Kel08] S. Kelly, D. Hesterberg, and B. Ravel. Analysis of Soils and Minerals Using X-ray Absorption Spectroscopy. In L. R. Drees and A. L. Ulery, editors, *Methods of Soil Analysis. Part 5. Mineralogical Methods*, volume 5, pages 387–463. American Society of Agronomy, Madison, 2008.
- [Kid84] K. Kidoh, k. Tanaka, and F. Marumo. Electron Density DIstribution in an Ilmenite-Type Crystal of Cobalt(II) Titanium(IV) Trioxide. *Acta Crystallogr. B*, 40(2):92–96, 1984.
- [Koe07] J. Koenig, B. Jancar, and D. Suvorov. New  $\text{Na}_{0.5}\text{Bi}_{0.5}\text{TiO}_3$ - $\text{NaTaO}_3$ -Based Perovskite Ceramics. *J. Am. Ceram. Soc.*, 90(11):3621–3627, 2007.
- [Kon88] D. Koningsberger and R. Prins, editors. *X-ray Absorption: Principles, Applications, Techniques of EXAFS, SEXAFS and XANES*, volume 92 of *Chemical Analysis*. John Wiley & Sons, Inc., New York, 1988.

- [Lem07] M. P. Leshenko, E. S. Nazarenko, A. A. Gonchar, L. A. Reznichenko, T. I. Nedoseykina, A. A. Novakovich, O. Mathon, and R. V. Vedrinskii. EXAFS Studies of the Local Atomic Structure of the Lead-Free Piezoelectric Ceramics  $K_xNa_{1-x}NbO_3$  Over the Temperature Range 10-1023 K. *Phys. Rev. B*, 76(13):134106–1–11, 2007.
- [Li04] H.-d. Li, C.-d. Feng, and W.-l. Yao. Some Effects of Different Additives on Dielectric and Piezoelectric Properties of  $(Bi_{1/2}Na_{1/2})TiO_3$ - $BaTiO_3$  Morphotropic-Phase-Boundary Composition. *Mater. Lett.*, 58(7-8):1194–1198, 2004.
- [Li06] J. F. Li, K. Wang, B. P. Zhang, and L. M. Zhang. Ferroelectric and Piezoelectric Properties of Fine-Grained  $Na_{0.5}K_{0.5}NbO_3$  Lead-Free Piezoelectric Ceramics Prepared by Spark Plasma Sintering. *J. Am. Ceram. Soc.*, 89(2):706–709, 2006.
- [Lim07] S. Limpijumnong, S. Rujirawar, and A. Boonchun. Identification of Mn Site in  $Pb(Zr,Ti)O_3$  by Synchrotron X-ray Absorption Near-Edge Structure: Theory and Experiment. *Appl. Phys. Lett.*, 90(10):103113, 2007.
- [Lin08] D. Lin, K. W. Kwok, and H. L. W. Chan. Structure and Electrical Properties of  $Bi_{0.5}Na_{0.5}TiO_3$ - $BaTiO_3$ - $Bi_{0.5}Li_{0.5}TiO_3$  Lead-Free Piezoelectric Ceramics. *Solid State Ionics*, 178(37-38):1930–1937, 2008.
- [Liu90] X. Liu and C. T. Prewitt. High-Temperature X-ray Diffraction Study of  $Co_3O_4$ : Transition from Normal to Disordered Spinel. *Phys. Chem. Miner.*, 17(2):168–172, 1990.
- [Lu06] W. Lu, G. Fan, X. Wang, and F. Liang. Dielectric and Piezoelectric Properties of  $[Bi_{0.5}(Na_{1-x}Li_x)_{0.5}]TiO_3$  Lead-Free Ceramic. *Jpn. J. Appl. Phys.*, 45(11):8763–8765, 2006.
- [Mae04] M. D. Maeder, D. Damjanovic, and N. Setter. Lead Free Piezoelectric Materials. *J. Electroceram.*, 13(1-3):385–392, 2004.
- [Mah07] S. Mahboob, G. Prasad, and G. S. Kumar. Impedance Spectroscopy and Conductivity Studies on B Site Modified  $(Na_{0.5}Bi_{0.5})(Nd_xTi_{1-2x}Nb_x)O_3$  Ceramics. *J. Mater. Sci.*, 42(24):10275–10283, 2007.
- [Mie08] G. Mie. Beiträge zur Optik trüber Medien, speziell kolloidaler Metallösungen. *Ann. Phys.*, 25(3):377–445, 1908.
- [Mod03] H. Modrow, S. Bucher, J. J. Rehr, and A. L. Ankudinov. Calculation and Interpretation of K-shell X-ray Absorption Near-Edge Structure of Transition Metal Oxides. *Phys. Rev. B*, 67(3):035123, 2003.
- [Mom11] K. Momma and F. Izumi. VESTA 3 for Three-Dimensional Visualization of Crystal, Volumetric and Morphology Data. *J. Appl. Crystallogr.*, 44(6):1272–1276, 2011.

- [Mou03] A. J. Moulson and J. M. Herbert. *Electroceramics: Materials, Properties, Applications*. Wiley, Chichester, 2nd ed. edition, 2003.
- [Nag01] H. Nagata and T. Tadashi. Additive Effects on Electrical Properties of  $(\text{Bi}_{1/2}\text{Na}_{1/2})\text{TiO}_3$  Ferroelectric Ceramics. *J. Eur. Ceram. Soc.*, 21(10-11):1299–1302, 2001.
- [Nag03] H. Nagata, M. Yoshida, Y. Makiuchi, and T. Takenaka. Large Piezoelectric Constant and High Curie Temperature of Lead-Free Piezoelectric Ceramic Ternary System Based on Bismuth Sodium Titanate-Bismuth Potassium Titanate-Barium Titanate near the Morphotropic Phase Boundary. *Jpn. J. Appl. Phys.*, 42(12):7401–7403, 2003.
- [Nag06] H. Nagata, T. Shinya, Y. Hiruma, T. Takenaka, I. Sakaguchi, and H. Haneda. Piezoelectric Properties of Bismuth Sodium Titanate Ceramics. In K. M. Nair, R. Guo, A. Bhalla, S.-I. Hirano, and D. Suvorov, editors, *Developments in Dielectric Materials and Electronic Devices*, pages 213–221. John Wiley & Sons, Inc, Hoboken and NJ and USA, 2006.
- [Pal87] H. I. Palmour and T. M. Hare. *Sintering 85*. Plenum Press, New York, 1987.
- [Pan09] P. K. Panda. Review Environmental Friendly Lead-Free Piezoelectric Materials. *J. Mater. Sci.*, 44(19):5049–5062, 2009.
- [Rae01] F. Raether, R. Springer, and S. Beyer. Optical Dilatometry for the Control of Microstructure Development During Sintering. *Mater. Res. Innovations*, 4(4):245–250, 2001.
- [Rae09a] F. Raether. Current State of In Situ Measuring Methods for the Control of Firing Processes. *J. Am. Ceram. Soc.*, 92(S1):146–152, 2009.
- [Rae09b] F. Raether. *Investigations on Sintering of Ceramics Using Novel Heating Methods, In-Situ Measuring and Computer Simulations*. Habilitation Thesis, University of Würzburg, Würzburg, 2009.
- [Rae09c] F. Raether and P. Schulze Horn. Investigation of Sintering Mechanisms of Alumina using Kinetic Field and Master Sintering Diagrams. *J. Eur. Ceram. Soc.*, 29(11):2225–2234, 2009.
- [Rah03] M. N. Rahaman. *Ceramic Processing and Sintering: Second Edition*. Taylor&Francis Inc., New York, 2003.
- [Rav01] B. Ravel. ATOMS: Crystallography for the X-ray Absorption Spectroscopist. *J. Synchrotron Rad.*, 8:314–316, 2001.

- [Rav05] B. Ravel and M. Newville. ATHENA, ARTEMIS, HEPHAESTUS: Data Analysis for X-ray Absorption Spectroscopy using IFEFFIT. *J. Synchrotron Rad.*, 12:537–541, 2005.
- [Reh00] J. J. Rehr and R. C. Albers. Theoretical Approaches to X-ray Absorption Fine Structure. *Rev. Mod. Phys.*, 72(3):621–654, 2000.
- [Reh09] J. J. Rehr, J. J. Kas, M. P. Prange, A. P. Sorini, Y. Takimoto, and F. Vila. Ab Initio Theory and Calculations of X-ray Spectra. *C.R. Phys.*, 10(6):548–559, 2009.
- [Rob98] G. Robert, M. Demartin, and D. Damjanovic. Phase Diagram for the  $0.4\text{Pb}(\text{Ni}_{1/3}, \text{Nb}_{1/3})\text{O}_3$ – $0.6\text{Pb}(\text{Zr}, \text{Ti})\text{O}_3$  Solid Solution in the Vicinity of a Morphotropic Phase Boundary. *J. Am. Ceram. Soc.*, 81(3):749–753, 1998.
- [Röd09] J. Rödel, W. Jo, K. Seifert, E. M. Anton, T. Granzow, and D. Damjanovic. Perspective on the Development of Lead-Free Piezoceramics. *J. Am. Ceram. Soc.*, 92(6):1153–1177, 2009.
- [Sak74] K. Sakata and Y. Masuda. Ferroelectric and Antiferroelectric Properties of  $(\text{Na}_{0.5}\text{Bi}_{0.5})\text{TiO}_3$ – $\text{SrTiO}_3$  Solid Solution Ceramics. *Ferroelectrics*, 7(1):347–349, 1974.
- [Sas99] A. Sasaki, T. Chiba, Y. Mamiya, and E. Otsuki. Dielectric and Piezoelectric Properties of  $(\text{Bi}_{0.5}\text{Na}_{0.5})\text{TiO}_3$ – $(\text{Bi}_{0.5}\text{K}_{0.5})\text{TiO}_3$  Systems. *Jpn. J. Appl. Phys.*, 38(9B):5564–5567, 1999.
- [Sat96] E. Sato and C. Carry. Yttria Doping and Sintering of Submicrometer-Grained alpha-Alumina. *J. Am. Ceram. Soc.*, 79(8):2156–2160, 1996.
- [Sha76] R. D. Shannon. Revised Effective Ionic Radii and Systematic Studies of Interatomic Distances in Halides and Chalcogenides. *Acta Crystallogr. A*, 32(5):751–67, 1976.
- [Shr07] T. R. Shrout and S. J. Zhang. Lead-Free Piezoelectric Ceramics: Alternatives for PZT? *J. Electroceram.*, 19(1):113–126, 2007.
- [Shu95] I. L. Shukaev and V. A. Volochaev. Ternary Sodium and Titanium Oxides with Cobalt(II). *Russ. J. Inorg. Chem.*, 40(12):1974–1980, 1995.
- [Shu05] V. A. Shuvaeva, D. Zekria, A. M. Glazer, Q. Jiang, S. M. Weber, P. Bhattacharya, and P. A. Thomas. Local Structure of the Lead-Free Relaxor Ferroelectric  $(\text{K}_x\text{Na}_{1-x})_{0.5}\text{Bi}_{0.5}\text{TiO}_3$ . *Phys. Rev. B*, 71(17):174114, 2005.
- [Ski07] T. A. Skidmore and S. J. Milne. Phase Development during Mixed-Oxide Processing of a  $(\text{Na}_{0.5}\text{K}_{0.5}\text{NbO}_3)_{(1-x)}(\text{LiTaO}_3)_x$  Powder. *J. Mater. Res.*, 22(8):2265–2272, 2007.



- [Smo61] G. A. Smolensky, V. A. Isupov, A. I. Agranovskaya, and N. N. Ktainik. New Ferroelectrics of Complex Composition. IV. *Sov. Phys. Solid State*, 2:2651–2654, 1961.
- [Spr04] M. Spreitzer, M. Valant, and D. Suvorov. The Synthesis of  $\text{Na}_{0.5}\text{Bi}_{0.5}\text{TiO}_3$  Ceramics. *Mater. Technol.*, 38(6):313–316, 2004.
- [Spr07] M. Spreitzer, M. Valant, and D. Suvorov. Sodium Deficiency in  $\text{Na}_{0.5}\text{Bi}_{0.5}\text{TiO}_3$ . *J. Mater. Chem.*, 17:185–192, 2007.
- [Suc88] J. Suchanicz, K. Roleder, A. Kania, and J. Hańaderek. Electrostrictive Strain and Pyroeffect in the Region of Phase Coexistence in  $\text{Na}_{0.5}\text{Bi}_{0.5}\text{TiO}_3$ . *Ferroelectrics*, 77(1):107–110, 1988.
- [Suc95] J. Suchanicz. Investigations of the Phase Transitions in  $\text{Na}_{0.5}\text{Bi}_{0.5}\text{TiO}_3$ . *Ferroelectrics*, 172(1):455–458, 1995.
- [Swa90] S. L. Swartz. Topics in Electronic Ceramics. *IEEE Trans. Electr. Insul.*, 25(5):935–987, 1990.
- [Tak91] T. Takenaka, K. Maruyama, and K. Sakata.  $(\text{Bi}_{1/2}\text{Na}_{1/2})\text{TiO}_3\text{-BaTiO}_3$  System for Lead-Free Piezoelectric Ceramics. *Jpn. J. Appl. Phys.*, 30:2236–2239, 1991.
- [Tan01] T. Tani, T. Takeuchi, and T. Kimura. Piezoelectric Ceramics and Production Process of the Same, 2001.
- [Thu77] H. Thurnauer. Reflections. *Am. Ceram. Soc. Bull.*, 56(10):861–866, 1977.
- [Ved98] R. V. Vedrinskii, V. L. Kraizman, A. A. Novakovich, P. V. Demekhin, and S. V. Urazhdin. Pre-Edge Fine Structure of the 3d Atom K X-ray Absorption Spectra and Quantitative Atomic Structure Determinations for Ferroelectric Perovskite Structure Crystals. *J. Phys.: Condens. Matter*, 10(42):9561–9580, 1998.
- [Wan05] X. X. Wang, X. G. Tang, K. W. Kwok, H. L. W. Chan, and C. L. Choy. Effect of Excess  $\text{Bi}_2\text{O}_3$  on the Electrical Properties and Microstructure of  $(\text{Bi}_{1/2}\text{Na}_{1/2})\text{TiO}_3$  Ceramics. *Appl. Phys. A*, 80(5):1071–1075, 2005.
- [Wan08] Y. Wang, D. Damjanovic, N. Klein, and N. Setter. High-Temperature Instability of Li- and Ta-Modified  $(\text{K},\text{Na})\text{NbO}_3$  Piezoceramics. *J. Am. Ceram. Soc.*, 91(11):1962–1970, 2008.
- [Wan12] H.-Q. Wang, Y.-J. Dai, and X.-W. Zhang. Microstructure and Hardening Mechanism of  $\text{K}_{0.5}\text{Na}_{0.5}\text{NbO}_3$  Lead-Free Ceramics with CuO Doping Sintered in Different Atmospheres. *J. Am. Ceram. Soc.*, 95(4):1182–1184, 2012.
- [Wat07] A. Watcharapasorn, S. Jiansirisomboon, and T. Tunkasiri. Sintering of Fe-Doped  $\text{Bi}_{0.5}\text{Na}_{0.5}\text{TiO}_3$  at  $<1000^\circ\text{C}$ . *Mater. Lett.*, 61(14-15):2986–2989, 2007.

- [Wil09] D. B. Williams and C. Barry Carter. *Transmission Electron Microscopy: A Textbook for Materials Science*. Springer, New York, 2nd edition edition, 2009.
- [Wyc63] R. W. G. Wyckoff. *Crystal Structures*. Interscience, New York and London, 2 edition, 1963.
- [Xia08] D. Xiao, D. Lin, J. Zhu, and P. Yu. Studies on New Systems of BNT-Based Lead-Free Piezoelectric Ceramics. *J. Electroceram.*, 21:34–38, 2008.
- [Xu91] Y. Xu. *Ferroelectric Materials and Their Applications*. North-Holland, Amsterdam, 1991.
- [Xu05] Q. Xu, X. Chen, W. Chen, S. Chen, B. Kim, and J. Lee. Synthesis, Ferroelectric and Piezoelectric Properties of Some  $(\text{Na}_{0.5}\text{Bi}_{0.5})\text{TiO}_3$  System Compositions. *Mater. Lett.*, 59(19-20):2437–2441, 2005.
- [Xu06] Q. Xu, X.-L. Chen, W. Chen, M. Chen, S.-L. Xu, B.-H. Kim, and J.-H. Lee. Effect of MnO Addition on Structure and Electrical Properties of  $(\text{Na}_{0.5}\text{Bi}_{0.5})_{0.94}\text{Ba}_{0.06}\text{TiO}_3$  Ceramics Prepared by Citrate Method. *Mater. Sci. Eng. B*, 130(1-3):94–100, 2006.
- [Xu08a] C. Xu, D. Lin, and K. W. Kwok. Structure, Electrical Properties and Depolarization Temperature of  $(\text{Bi}_{0.5}\text{Na}_{0.5})\text{TiO}_3\text{-BaTiO}_3$  Lead-Free Piezoelectric Ceramics. *Solid State Sci.*, 10(7):934–940, 2008.
- [Xu08b] Q. Xu, M. Chen, W. Chen, H.-X. Liu, B.-H. Kim, and B.-K. Ahn. Effect of CoO Additive on Structure and Electrical Properties of  $(\text{Na}_{0.5}\text{Bi}_{0.5})_{0.93}\text{Ba}_{0.07}\text{TiO}_3$  Ceramics Prepared by the Citrate Method. *Acta Mater.*, 56(3):642–650, 2008.
- [Yan99] A. Yankin, O. Vikhreva, and V. Balakirev. P–T–x Diagram of the Co–Ti–O System. *J. Phys. Chem. Solids*, 60(1):139–143, 1999.
- [Zha07] W. Zhao, H. Zhou, Y. Yan, D. Liu, and S. Liu. Influence of Different Dopants on the Piezoelectric Properties of the  $\text{Na}_{0.5}\text{Bi}_{0.5}\text{TiO}_3\text{-BaTiO}_3$  Lead-Free Ceramics. *Key Eng. Mater.*, 336-338:105–108, 2007.
- [Zha08a] S.-T. Zhang, A. B. N. Kouna, E. Aulbach, T. Granzow, W. Jo, H. J. Kleebe, and J. Rödel. Lead-Free Piezoceramics with Giant Strain in the System  $\text{Bi}_{0.5}\text{Na}_{0.5}\text{TiO}_3\text{-BaTiO}_3\text{-K}_{0.5}\text{Na}_{0.5}\text{NbO}_3$ . I. Structure and Room Temperature Properties. *J. Appl. Phys.*, 103(3):034107–034107–8, 2008.
- [Zha08b] S.-T. Zhang, A. B. N. Kouna, E. Aulbach, W. Jo, T. Granzow, H. Ehrenberg, and J. Rödel. Lead-Free Piezoceramics with Giant Strain in the System  $\text{Bi}_{0.5}\text{Na}_{0.5}\text{TiO}_3\text{-BaTiO}_3\text{-K}_{0.5}\text{Na}_{0.5}\text{NbO}_3$ . II. Temperature Dependent Properties. *J. Appl. Phys.*, 103(3):034108, 2008.

# A Appendix

A.1	Table of Raw Materials . . . . .	86
A.2	Crystallographic Data for XANES Calculations . . . . .	87
A.3	STEM-EDX Line Scans . . . . .	88
A.4	Dielectric Characterization of BNT . . . . .	91

Table A.1: Detailed list of starting powders for BNT synthesis including impurities:

Powder	Bismuth oxide	Rutile	Sodium carbonate	Cobalt oxide
Chemical formula	Bi <sub>2</sub> O <sub>3</sub>	TiO <sub>2</sub>	Na <sub>2</sub> CO <sub>3</sub>	Co <sub>3</sub> O <sub>4</sub>
Purity	99.975 %	99.8 %	99.95 %	99.7 %
Particle size <sup>a</sup>	<4 μm	0.9 μm to 1.6 μm	agglomerates, ca. 1 mm	<37 μm
Supplier	Alfa Aesar <sup>b</sup>	Alfa Aesar <sup>b</sup>	Acros Organics <sup>c</sup>	Alfa Aesar <sup>b</sup>
Impurities	SO <sub>4</sub> , Cl < 10 ppm, Na 1 ppm	Al 16 ppm, Ca 279 ppm, Fe 42 ppm, K 133 ppm, Mg 36 ppm, P 183 ppm, Si 42 ppm, S 45 ppm, Zr 348 ppm	Heavy metals <5 ppm, nitrogen compounds <0.001 ppm, total sulfur (SO <sub>4</sub> ) <0.05 %, insoluble matter in H <sub>2</sub> O <0.01 %; Trace analysis: Al < 10 ppm, Ca < 50 ppm, Cl < 20 ppm, Fe < 5 ppm, K < 100 ppm, PO <sub>4</sub> < 10 ppm, SiO <sub>2</sub> < 50 ppm	Fe 39 ppm, Mn 4 ppm, Ni < 10 ppm, S 600 ppm, Ca 61 ppm, Cu < 1 ppm

<sup>a</sup> as stated by the manufacturer  
<sup>b</sup> Alfa Aesar GmbH, Karlsruhe, Germany  
<sup>c</sup> Acros Organics, Geel, Belgium

**Table A.2:** Crystallographic data used for XANES calculations.  $a$ ,  $b$ ,  $c$  = unit cell dimensions,  $\theta_D$  = Debye temperature.

Crystal phase	Space group	$a$ [Å]	$b$ [Å]	$c$ [Å]	from	$\theta_D$ [K]	Cluster size [atoms]
$\text{Bi}_{0.5}\text{Na}_{0.5}\text{TiO}_3^a$	Cc	9.5261	5.4831	5.5079	[Aks11]	185	124
$\text{Co}_2\text{TiO}_4$	$Fd\bar{3}m$	8.420	8.420	8.420	[Hir90]	560	89
$\text{Co}_3\text{O}_4$	$Fd\bar{3}m$	8.1099	8.1099	8.1099	[Liu90]	525	89
$\text{CoO}$	$Fm\bar{3}m$	4.2603	4.2603	4.2603	[Car55]	518	81
$\text{CoTiO}_3$	$R\bar{3}$	5.0394	5.0394	13.811	[Kid84]	500	143
Co	$P6_3/mmc$	2.5071	2.5071	4.0695	[Wyc63]	385	81

<sup>a</sup>  $\beta = 125.3442^\circ$

### A.3 STEM-EDX Line Scans

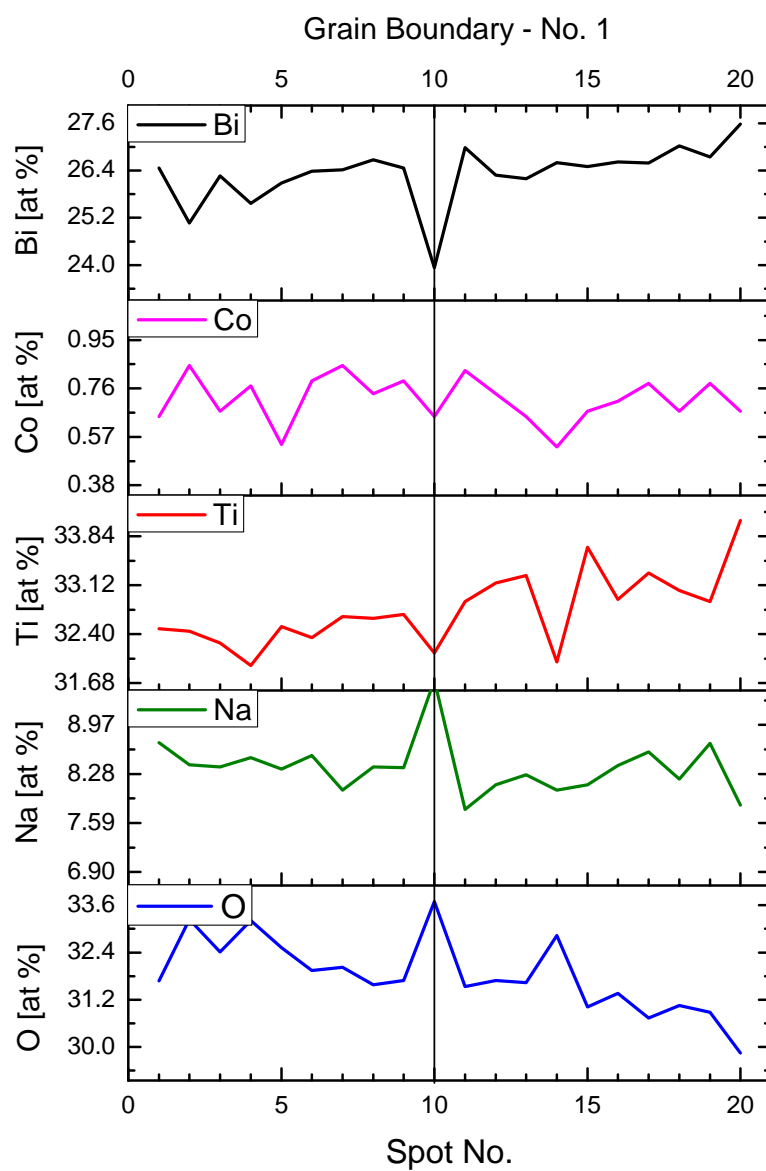


**Figure A.1:** STEM-EDX line scan across grain boundary 1 in Figure 5.8.

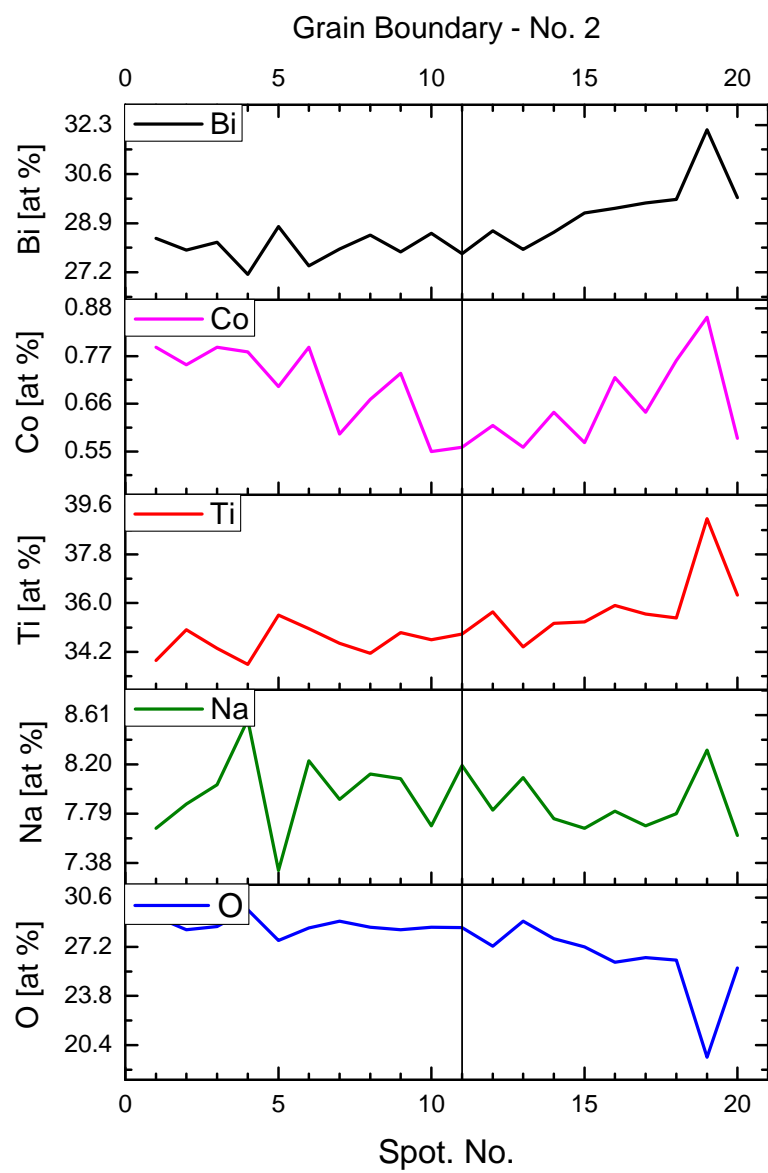


**Figure A.2:** STEM-EDX line scan across grain boundary 2 in Figure 5.8.

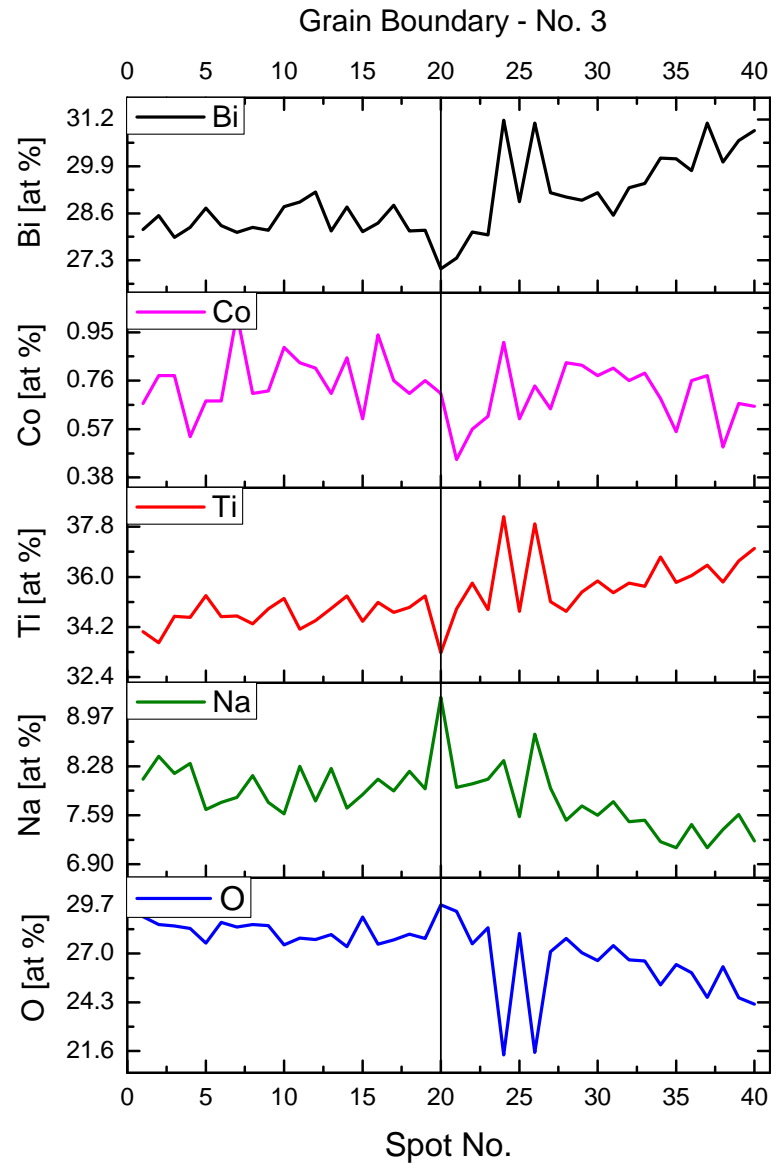


**Figure A.3:** STEM-EDX line scan across grain boundary 3 in Figure 5.8.



## A.4 Dielectric Characterization of BNT

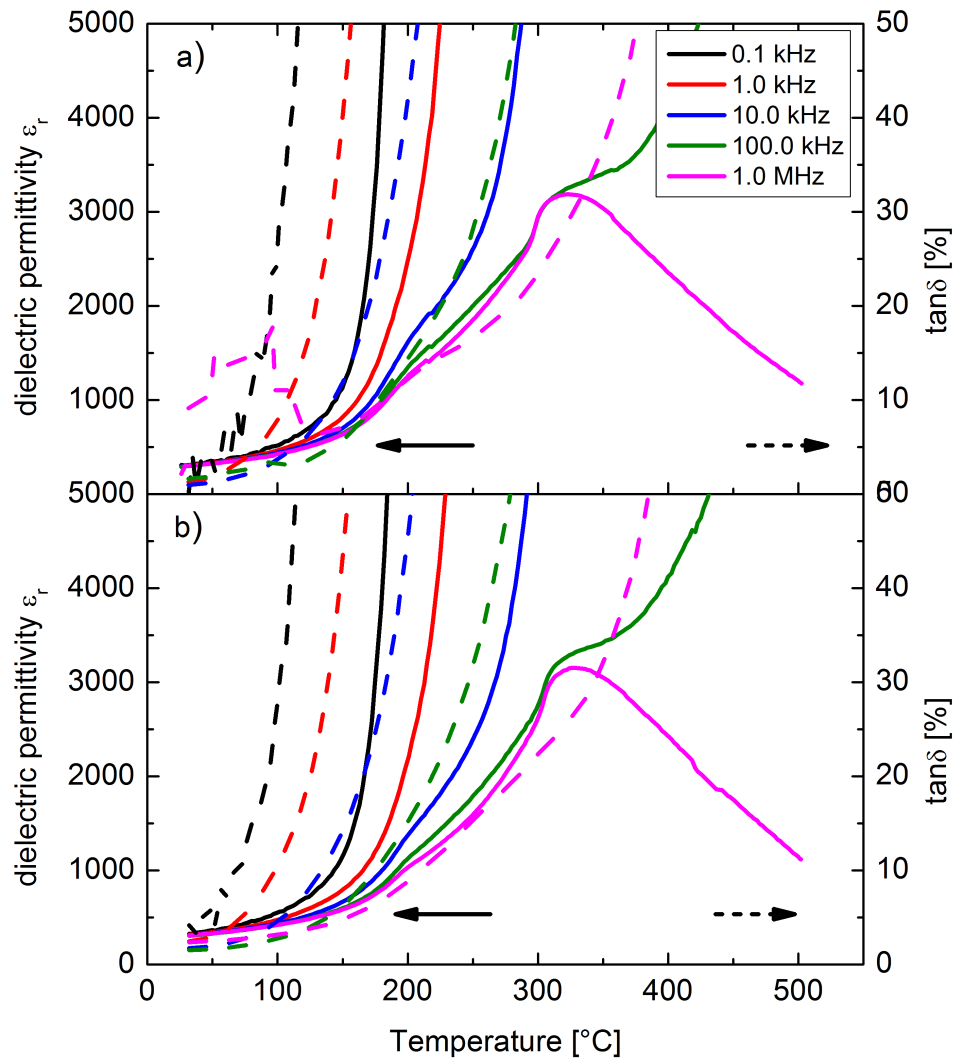


**Figure A.4:** Relative dielectric permittivities  $\varepsilon_r$  (solid lines) and loss  $\tan \delta$  (dashed lines) of BNT doped with a) 0.5 mol % Co and b) 2.6 mol % Co as a function of temperature; the samples were aged for at least 24 h before measuring.



# Curriculum Vitae

## Personal Information

Name:	Veronika Schmitt, née Gössl
Date of Birth:	25 Aug 1984
Place of Birth:	Regensburg, Germany
Nationality:	German

## Education

Feb 2009 - Dec 2012	PhD Student at the University of Bayreuth and Fraunhofer Institute für Silicatforschung ISC (Würzburg)
Nov 2008	Diploma in Mineralogy, final grade 1.1
Mar 2008 - Nov 2008	Diploma Thesis at the Fraunhofer ISC, Topic: Lead-Free Piezoceramics
Oct 2003 - Mar 2008	Diploma Studies (Mineralogy) at the University of Würzburg
Jul 2003	German Abitur at the Goethe-Gymnasium Regensburg, overall grade 1.6

## Professional Occupation

Feb 2009 - Dec 2012	Scientific researcher at the University of Bayreuth and Fraunhofer ISC
Dec 2008 - Feb 2009	Student assistant at the Fraunhofer ISC, phase analysis of silicon nitride ceramics
Aug 2007 - Feb 2008	Student assistant at the Fraunhofer ISC, project 'Infiltration of silicon carbide preforms with Si'

## Stipends and Awards

Feb 2009 - Dec 2012	Member of the international doctorate program ‘Structure, Reactivity and Properties of Oxide Materials’ of the Elite Network of Bavaria
Dec 2010	Poster Award at the ‘Chemie-Symposium der Studierenden Mainfrankens 2010’

## Publications and Conferences

- [1] V. Schmitt and F. Raether. Effect of Cobalt Doping on the Sintering Mechanisms of the Lead-Free Piezoceramic  $(\text{Bi}_{0.5}\text{Na}_{0.5})\text{TiO}_3$ . *J. Eur. Ceram. Soc*, 34(1): 15-21, 2014.
- [2] V. Schmitt and T. E. M. Staab. Co-Doping of  $(\text{Bi}_{0.5}\text{Na}_{0.5})\text{TiO}_3$ : Secondary Phase Formation and Lattice Site Preference of Co. *J. Phys.: Condens. Matter*, 24(45): 455901, 2012.
- [3] Conference Abstract: V. Schmitt, P. Scheiner, F. Raether and T. E. M. Staab. Influence of Co and Cu Doping on the Lead-Free Piezoceramic Bismuth Sodium Titanate. *International Conference on Electroceramics 2011* (Sydney, Australia), 2011.

# Acknowledgments

The members of my thesis committee contributed greatly to the success of this thesis:

I would like to thank Professor Sextl for giving me the opportunity to carry out this work at the Fraunhofer ISC. I am grateful for the professional discussions and for his numerous, helpful suggestions.

I am thankful to Professor Breu for the critical feedback, discussions and valuable advice which served to improve the quality of my work significantly.

I would like to express my sincere gratitude to Dr. Raether for sharing his profound knowledge on sintering and for his tireless readiness for long discussions.

In addition, I thank the above-named members of my thesis committee for their great patience and support in the face of numerous obstacles.

I would like to express my deep gratitude to my advisor Dr. Staab for his guidance, inspiring discussions and fruitful suggestions. I greatly appreciated his unwavering support and encouragement throughout this work, especially as things went badly for a while. He also helped me to become aware of my personal strengths.

The financial support by the Elitenetzwerk Bayern is gratefully acknowledged. I thank everyone from Bayerisches Geoinstitut involved in the organization of the graduate program.

I would like to thank my co-workers at Fraunhofer ISC for introducing me to lab equipment and measurement devices, for sample preparation and analysis—particularly last minute favors—and the help with administrative issues. A special thanks goes to my former diploma student P. Scheiner for his contribution to our research topic.

For the great deal of assistance from outside the Fraunhofer ISC in analytical tasks, I would like to thank Dr. Dudzik and Dr. Feyerherm (BESSY), D. Krauß (BGI), Professor Damjanovic (EPFL) and Dr. Schreiner (CeramTec).

Thank you fellow office mates and friends for the delightful ambiance and the everyday conversations, you greatly helped me to keep going! The same holds true for the moral support and advice by Dr. Helbig.

Finally I thank my family: My brother Wolfram and my parents, for your compassion, constant moral support and assistance with all sorts of computer issues. You were always there when I doubted my strength. My family-in-law, for your encouragement and for making me laugh so many times with you.

My husband Dominik, for your love, backing and great patience! This endeavor would not have been possible without you!

Last but not least, my cat deserves an acknowledgment for guarding and consoling me in her very own way!

# Declaration of Authorship

I hereby declare that this submission is my own work and that, to the best of my knowledge and belief, it contains no materials previously published or written by another person nor material which to a substantial extent has been accepted for the award of any other degree or diploma of the university or other institute of higher learning, except where due acknowledgement has been made in the text.

I have not previously attempted to or succeeded in acquiring any academic degree except those presented with the submission of this thesis.

Würzburg, 31 January 2013

---

Veronika Schmitt